DISSERTATION

submitted to the

Combined Faculty of Mathematics, Engineering and Natural Sciences

of Heidelberg University, Germany

for the degree of

Doctor of Natural Sciences

Put forward by

Valerie Susanne Klein

born in Ludwigsburg (Germany)

Oral examination: May 4th 2022

MODELING AND MEASURING CARDIAC MAGNETOSTIMULATION

Referees: Prof. Dr. Lothar R. Schad
Prof. Dr. Peter Bachert

Für meine Eltern.

MODELLIERUNG UND MESSUNG DER MAGNETSTIMULATION DES HERZENS

Die Magnetresonanztomographie (MRT) verwendet magnetische Gradientenwechselfelder, welche im Patienten elektrische Felder (E-Felder) induzieren, die das Herz stimulieren könnten. Die theoretische Leistungsfähigkeit der neuesten Generation von Gradientensystemen wird in der Praxis zunehmend durch regulatorische Sicherheitsgrenzwerte zur Vermeidung der Herzstimulation (HS) eingeschränkt. Vor diesem Hintergrund untersucht die vorliegende Arbeit HS-Schwellenwerte sowie die der HS zugrunde liegenden physikalischen und physiologischen Mechanismen mit einem integrativen Ansatz aus Modellierung und Messungen. Zunächst wurde ein Modell zur Vorhersage von Stimulationsschwellen und dem entsprechenden Ort der Stimulation im Herzen entwickelt. Dieses Modell basiert auf einer Kombination von E-Feld-Simulationen in numerischen Körpermodellen und elektrophysiologischen Herzfasermodellen. Die HS-Schwellenwerte wurden für zwei kommerzielle Gradientensysteme modelliert und lagen >10-fach über den regulatorischen Sicherheitsgrenzwerten. Im nächsten Schritt wurden Schwellenwerte für die Magnetstimulation des Herzens in vivo in zehn gesunden Schweinen gemessen. Hierfür wurden Magnetfeldpulse durch Entladungen einer Kondensatorbank in eine Spule erzeugt. Die durchschnittliche E-Feld-Stimulationsschwelle im Schweineherzen lag bei 92.9 ± 13.5 V/m. Die Abweichung zwischen experimentellen und in tierspezifischen MR-basierten Schweinemodellen vorhergesagten Stimulationsschwellenwerten lag bei $\leqslant$18%. Dies validiert die Gültigkeit des Modells für die in den Experimenten verwendete Magnetpulsform. Die experimentellen und modellbasierten Ergebnisse dieser Arbeit tragen dazu bei, die Sicherheit des Patienten in der MRT zu gewährleisten, ohne das räumliche und zeitliche Auflösungsvermögen der Bildgebung unnötig einzuschränken.

MODELING AND MEASURING CARDIAC MAGNETOSTIMULATION

Magnetic resonance imaging (MRI) employs time-varying magnetic gradient fields, which induce electric fields (E-fields) in the patient that can potentially stimulate the heart. The performance of novel gradient systems is increasingly restricted by regulatory safety limits, thus motivating a deeper understanding of cardiac stimulation (CS) in MRI. This thesis investigates the thresholds and mechanisms underlying CS using an integrative approach of modeling and measurements. First, a numerical modeling framework was developed that combines E-field simulations in computational body models with electrophysiological cardiac fiber models to predict stimulation thresholds and sites in the heart. The CS thresholds predicted for two commercial gradient systems were >10-fold higher than the regulatory limits. Second, cardiac magnetostimulation thresholds were measured in ten healthy pigs using magnetic field pulses created by capacitor discharges into a coil. The average threshold E-field in the porcine heart was 92.9 ± 13.5 V/m. CS thresholds predicted in individualized porcine models derived from MR images reproduced the measurements with deviations of $\leqslant$18%, thus demonstrating the validity of the model for the experimental magnetic field waveform. The numerical and experimental results presented in this thesis inform the derivation of safe operational limits for MRI without unnecessarily restricting gradient performance and thus imaging speed and resolution.

ACKNOWLEDGEMENTS

First and foremost, I would like to thank Prof. Dr. Lothar R. Schad for providing me with the opportunity to work as a part of his research group. You have given me the freedom to pursue my research interests and supported me in achieving my academic goals throughout my master and PhD projects.

Second, I would like to thank Prof. Dr. Peter Bachert for acting as referee of this thesis. Your lectures and seminars on Medical Physics encouraged me to pursue research in this field, starting with my bachelor thesis and throughout my PhD.

My special thanks goes to Prof. Dr. Lawrence L. Wald, Prof. Dr. Bastien Guérin, and Dr. Mathias Davids. Your scientific guidance and mentoring during our biweekly meetings and during my research visit in Boston, your excellent ideas, and your continued support and encouragement have contributed greatly to the results of this work. Thank you also to Livia Vendramini, Natalie Ferris, and Michael Reichert for the many helpful and productive discussions. I really enjoy working as part of our little team.

Many thanks to Prof. Dr. Christopher Nguyen, Livia Vendramini, Prof. Dr. David Sosnovik, Donald Straney, and Dr. Jaume Coll-Font for your help with the experimental study performed as part of this thesis. Without your support and valuable contributions, this work would not have been possible.

To my dear colleagues at CKM: Thank you for the many coffee and Tischkicker breaks, the climbing sessions, and the occasional Feierabendbier that made work and everything around it so much more enjoyable. I have always appreciated the friendly atmosphere in the office, the never-ending supply of chocolate when it was most needed, and the funny and sometimes weird discussions that have resulted in some very close friendships.

Thank you to Anne, Chris, Efe, Irène, Mathias, Michael (x2), Natalie, and Safa for your helpful thoughts and comments on this thesis.

Thank you to my parents and my brother for always having my back, for your unconditional support and for believing in all my ideas and ambitions.

To Georg, for being there for me through the highs and lows of my PhD journey and beyond, sharing the joy at successes and encouraging to overcome problems. Thank you for everything.

CONTENTS

LIST OF FIGURES

LIST OF TABLES

LIST OF ABBREVIATIONS

AP Action potential

AV Atrioventricular

CNS Central nervous system

COP Coplanar spiral coil pair

CS Cardiac stimulation

CT Computed tomography

ECG Electrocardiography

EM Electromagnetic

EMP Electromagnetic pulse

EP Electrophysiological

EPI Echo-planar imaging

FEM Finite element method

FID Free induction decay

FOV Field-of-view

GPA Gradient power amplifier

HML Human Monitoring Laboratory

IEC International Electrotechnical Commission

MIP Maximum intensity projection

MPI Magnetic particle imaging

MRG McIntyre-Richardson-Grill

MRI Magnetic resonance imaging

NMR Nuclear magnetic resonance

PNS Peripheral nerve stimulation

PVC Premature ventricular contraction

RF Radiofrequency

SA Sinoatrial

SD Standard deviation

SE Spin echo

SOL Solenoid coil

SR Slew rate

TE Echo time

TMS Transcranial magnetic stimulation

TMV Transmembrane voltage

VF Ventricular fibrillation

1 INTRODUCTION

The ability of magnetic resonance imaging (MRI) to acquire both functional and morphological images with high soft tissue contrast has made it an important imaging tool for diagnosing pathological conditions as well as planning and following their treatment. MRI has also enabled ground-breaking advancements in research, for example in mapping and understanding structural connections of the human brain (McNab et al., 2013; Wang et al., 2021). The MR imaging process employs a high-amplitude static magnetic field to align the hydrogen atom's nuclear spins in the patient. Perturbation from this equilibrium alignment ("excitation") causes the spins to precess around the magnetic field axis with a nucleus-specific precession frequency that is proportional to the magnitude of the local magnetic field. Excitation of the spin system is achieved by applying a radiofrequency (RF) magnetic field at resonance frequency, which is followed by the reception of the signal induced by the spins in a receive coil during their decaying precession. The spatial origin of this signal is encoded using magnetic "gradient fields": superimposing these to a uniform static magnetic field creates a spatial dependence of the spins' resonance frequency. This establishes a link between a signal's frequency and its origin in space, thus enabling the formation of images from the measured signals.

Both the imaging speed and the spatial image resolution depend on the performance of the gradient system. Some imaging techniques, such as diffusion MRI (Huang et al., 2021; Tian et al., 2022), require particularly high gradient field amplitudes. At the same time, the gradient fields need to be switched rapidly, i. e., in the kilohertz frequency range, to efficiently acquire the quickly decaying signal. The gradient switching speed is usually quantified in terms of slew rate, which is defined as the ratio of the peak gradient field amplitude and the rise time. High slew rates are especially relevant for fast readout techniques such as fast spin echo (Listerud et al., 1992), echo-planar imaging (Mansfield and Maudsley, 1977), and balanced steady-state free precession (Bieri and Scheffler, 2013). These techniques are, e. g., used to capture dynamic processes in the human body, such as breathing (Baumann et al., 2009), functional brain activation (Logothetis, 2008), or the beating heart (Nguyen et al., 2014).

As per Faraday's law, time-varying magnetic fields such as MRI gradient fields induce electric fields (E-fields) in conductive media like biological tissue. Gradient-induced E-fields in the patient can become strong enough to stimulate excitable tissues, a phenomenon referred to as "magnetostimulation". In MRI, magnetostimulation is most commonly observed in the form of peripheral nerve stimulation (PNS) (Cohen et al., 1990; Mansfield and Harvey, 1993; Molendowska et al., 2021; Nyenhuis and Gross, 2019; Schenck, 2013). At onset, PNS can be experienced as light tingling or touch perceptions (Budinger et al., 1991; Schaefer et al., 2000). When the gradient field switching rate (dB/dt) is increased to 50% or more above the threshold,

PNS can become more severe, resulting in involuntary muscle contractions and pain (Bourland et al., 1999; Budinger et al., 1991).

Another, much more dangerous form of gradient-induced magnetostimulation is that of the heart muscle (Irnich, 1994; Irnich and Schmitt, 1995; Nyenhuis et al., 1994; Reilly, 1991, 1992b; Schaefer et al., 2000). Like peripheral nerves, the myocardium can be electrically excited by externally applied or magnetically induced E-fields. Cardiac stimulation (CS) can cause the induction of single ectopic heartbeats and can even result in arrhythmias like ventricular fibrillation (VF) (Antoni, 1998; Reilly, 1992b). As such, CS can lead to life-threatening situations, as opposed to PNS that can become uncomfortable or painful at most. While the risk of CS by MRI gradients has been estimated to be low (Reilly, 1998; Schaefer et al., 2000), there was a single account of a premature ventricular contraction (PVC) observed in a patient with heart disease during a routine MRI scan (Lohr et al., 1999). It was postulated that metallic clips implanted in the patient's heart muscle may have locally amplified the E-field, which may have led to stimulation at lower gradient field switching rates than expected under normal circumstances (Lohr et al., 1999).

The most recent progress in MRI gradient technology makes CS an increasingly important safety issue. Modern MRI systems can reach gradient field amplitudes of 300-500 mT/m with slew rates of up to 600 T/m/s (Huang et al., 2021; McNab et al., 2013; Setsompop et al., 2013; Tan et al., 2020). A recently developed special-purpose gradient coil designed for diffusion imaging of the female breast can even reach gradient strengths of up to 1 T/m (Jia et al., 2021; Littin et al., 2021). Albeit impressive, these advances in gradient performance cannot be fully utilized due to PNS or CS restrictions.

The occurrence of PNS is minimized by restricting dB/dt below the average PNS threshold measured in studies on healthy human volunteers (Feldman et al., 2009; Lee et al., 2016; Setsompop et al., 2013). Unlike PNS, magnetically induced CS thresholds cannot be measured in humans because of the potentially dangerous outcome for the subject. As a consequence, the CS limit described in regulatory guidelines on MRI safety issued by the International Electrotechnical Commission (IEC 60601-2-33 (IEC, 2010)) are based on a combination of electrode stimulation ("electrostimulation") experiments and simple electromagnetic (EM) field simulations. The IEC guidelines limit the maximum gradient dB/dt and the induced E-field based on the exponential strength-duration curve (Blair, 1932), which is often used to quantify tissue stimulation thresholds as a function of pulse duration. In this frame, the pulse duration is defined as the duration of the applied dB/dt or E-field stimulus, i.e., the slew period of the applied magnetic field. The strength-duration curve is defined by two parameters: a minimum asymptotic threshold for infinite pulse duration, the "rheobase", and a time constant describing how fast the stimulation threshold decreases with increasing pulse duration.

The IEC standard, as it is still used today, was based on the important work by Reilly, who derived strength-duration parameter values from a large body of electrode CS experiments conducted mainly in animals (Reilly, 1991, 1992b). The lowest CS threshold reported by one of these experiments (Roy, 1980) is similar to the theoretical stimulation threshold of a large 20-µm diameter myelinated nerve predicted using a neurodynamic model (Reilly, 1992b). From this single experimental value,

Reilly estimated that for the most sensitive percentile of the population, the E-field rheobase for cardiac tissue would be similar to the theoretical rheobase for a 20-µm nerve, namely 6.2 V/m (Reilly, 1991, 1992b). The cardiac E-field rheobase for the population average was estimated to be twice that value (12 V/m (Reilly, 1992a,b)), which is in contrast to another review of electrostimulation studies that estimated an average rheobase of 60 V/m (Irnich, 1994).

The IEC chose Reilly's more conservative estimate of 6.2 V/m and included an additional safety factor in their guidelines, resulting in a rheobase of 2 V/m (IEC, 2010). The time constant of cardiac tissue used in the IEC standard was set at 3 ms (IEC, 2010). This value is an estimated average of experimental values reported in the literature, which showed a wide variability of 0.2 to 7.7 ms (Reilly, 1991, 1992b). Finally, attempts were made to translate the resulting E-field limit to a dB/dt limit, yielding a quantity that is more accessible to monitoring in MRI (unlike the E-field, a coil's magnetic field can be measured directly). For this conversion, Reilly calculated the E-field induced in a homogeneous ellipsoidal model of the torso of "a large man" exposed to a uniform time-varying B-field (Reilly, 1992b). This calculation relied on several simplifications, such as neglecting the formation of E-field hotspots by the body's inhomogeneous distribution of conductive tissues. Using this simplified E-field-to-dB/dt conversion, the IEC estimated the dB/dt rheobase for the human heart to be 20 T/s (IEC, 2010). For some high-performance gradient systems, such as in the Connectome MRI scanner (McNab et al., 2013; Setsompop et al., 2013), the IEC cardiac safety limit is lower than the PNS limit at long rise times. In this case, CS becomes the limiting factor to the application of the gradient technology, replacing the commonly more limiting PNS concern. The lack of CS events compared to the almost daily observation of PNS in MRI, however, suggests that this limitation is an artifact of the conservative nature imposed by lack of cardiac magnetostimulation data in the regulatory process. Additionally, despite the potential adverse impact of cardiac magnetostimulation in MRI, there is a fundamental lack of insights into its underlying mechanisms.

In light of the increasing relevance of CS as a limiting factor of MR imaging performance, this thesis aims to establish a deeper understanding of the physical and physiological fundamentals of cardiac magnetostimulation. To achieve this goal, magnetically induced CS is investigated both through numerical modeling and animal stimulation experiments. The thesis consists of three main parts that entail the following:

i. The development of a modeling framework for the prediction of cardiac magnetostimulation in computational anatomical models (Klein et al., 2021)

ii. An experimental study that measures the cardiac magnetostimulation threshold of the porcine heart (Klein et al., 2022)

iii. Predictions of cardiac magnetostimulation thresholds in individualized porcine body models using the framework developed in (i) to provide an in-depth model validation

The first part of this thesis develops a computational framework to model CS by time-varying magnetic fields created by arbitrary coil wire geometries and current waveforms. The modeling framework combines EM field simulations in detailed, high-

resolution human and animal anatomical models with electrophysiological models of electrically excitable cardiac fibers. The need for a computational CS model is especially acute regarding the ethical difficulties to obtain experimental data in humans. In recent years, the number of in silico studies of cardiac electrophysiology has risen drastically (Plank et al., 2021), and modeling is playing an increasingly important role in clinical cardiology (Niederer et al., 2018). However, most of these studies model average electrophysiological properties on a macroscopic organ level and do not include individual cardiac cells due to the high computational costs (Jaeger et al., 2021). This inhibits the investigation of small-scale interactions on a cellular level, such as electrical stimulation of single cardiomyocytes by extracellular E-fields. Some previous work has modeled isolated cardiac fibers consisting of several cells connected end-to-end by gap junctions (Rudy and Quan, 1987, 1991). However, to the best of the author's knowledge, this thesis is the first to integrate such fiber models into a detailed macroscopic model of the human anatomy and to apply this modeling approach to the investigation of cardiac magnetostimulation.

A few previous studies have simulated the E-field distribution induced by MRI gradient coils in the heart of heterogeneous human body models (Liu et al., 2003; Pastore et al., 2011; Wang et al., 1995; Xia et al., 2002). Two of these studies (Liu et al., 2003; Xia et al., 2002) combined the simulated E-field with a mesh representation of the heart equipped with phenomenological parameters such as action potential (AP) waveform and conduction velocity (Lu and Xia, 1996; Xia et al., 1996). The authors used this heart model to simulate the conduction of depolarization waves, i. e., electrical activation in the form of APs, through the myocardium. The electrical potential changes simulated in the heart were in turn used to predict electrocardiography (ECG) signals on the skin surface of the body model. The heart model was stimulated by the initiation of APs at the mesh nodes corresponding to the locations with the highest induced E-field (Liu et al., 2003). Under these artificial conditions, the simulated ECG signals showed severe arrhythmias when the heart model was stimulated continuously over one cardiac cycle (Liu et al., 2003). However, the authors did not determine the threshold E-field required for cardiac excitation, i. e., the generation of APs.

In contrast to these previous simulations, the model developed in this thesis includes realistic descriptions of the geometry and electrophysiology of excitable fibers in the heart, which were embedded within anatomical models equipped with EM tissue properties for the E-field simulations. Explicitly modeling the paths of excitable fibers in the heart is important as it has been shown that it is not the magnitude of the induced E-field but rather the relative orientation of the E-field and the cardiac tissue that is critical for stimulation (Knisley et al., 1999). For the CS predictions in this thesis, the E-field in the heart is projected onto the fiber paths, integrated along their length to obtain electrical potential changes, and modulated in time with the coil current waveform. The resulting spatiotemporal potential changes are fed into electrical-circuit representations of the electrical activity of cardiac fibers. These fiber models predict the response of the cardiac fibers to an imposed E-field, including the initiation of APs, and thus CS. Previous work has applied a similar approach of coupling simulated E-fields with neurodynamic models of peripheral nerve fibers to successfully predict PNS by MRI gradient fields (Davids et al., 2019a, 2020, 2017,

2019b; Klein et al., 2019). This thesis investigates stimulation thresholds of two types of cardiac fibers, i. e., Purkinje and ventricular myocardial fibers, both of which play essential roles in cardiac excitation and signal conduction. Purkinje fibers form a dense network on the sub-endocardium and are responsible for spreading the depolarization wave uniformly and rapidly throughout the ventricles. The ventricular myocardium itself is organized in fiber-like structures that enable the ventricles to contract upon electrical stimulation. The ion channel dynamics of individual cardiac cells are modeled using dedicated membrane models of the human cardiac Purkinje cell (Stewart et al., 2009) and the ventricular myocyte (O'Hara et al., 2011). The cells are electrically connected end-to-end with resistive gap junctions to form fiber-like structures (Rudy and Quan, 1987, 1991).

For a preliminary model validation, CS thresholds were predicted in canine body models and compared with two experimental studies from the early 1990s that measured cardiac magnetostimulation thresholds in dogs (Mouchawar et al., 1992; Nyenhuis et al., 1992). Simulations were then performed in an adult male and female human body model to predict CS thresholds for two commercial whole-body MRI gradient systems and for different gradient waveforms. The predicted human CS thresholds were compared with the IEC cardiac safety limit (IEC, 2010) of these gradient systems as well as the gradients' PNS thresholds.

The second part of this thesis describes the measurement of cardiac magnetostimulation thresholds in ten healthy, anesthetized pigs to further validate the model's predictions. Due to their similarity to humans in terms of heart size and AP shape and duration (Gaur et al., 2021), this large animal model is integral to most current cardiovascular research (Azarov et al., 2018; Clauss et al., 2019; Dixon and Spinale, 2009; Valdeomillos et al., 2019). Despite the potential value of using pigs to shed light on cardiac magnetostimulation, a thorough search of the relevant literature did not yield any previous experiments. The bulk of previously measured CS thresholds comes from electrode experiments, and only a few studies measured cardiac magnetostimulation thresholds in vivo. In the early 1990s, magnetically induced CS was measured in anesthetized canines (Andoh et al., 1994; Mouchawar et al., 1992; Nyenhuis et al., 1991, 1992; Yamaguchi et al., 1991, 1992, 1994). These studies induced CS by discharging large capacitors into inductive solenoid or flat spiral coils positioned close to the canines' chest or in direct contact with the myocardium, respectively, which created a time-varying magnetic field. Successful CS was identified on ECG and arterial blood pressure signals, and thresholds were reported in terms of minimum coil current or dB/dt resulting in an altered cardiac rhythm. Simulations in simple computational models of the canine torso indicated that a peak induced E-field of approximately 100 V/m was required to stimulate the canine heart (Mouchawar et al., 1993; Ragan et al., 1995). Unfortunately, essential details in this series of pioneering experiments, such as the exact anatomy and posture of the canines, were either not reported or are unknown, making it challenging to extrapolate these experimental results to humans retrospectively.

For the porcine experiments performed in this thesis, a magnetic cardiac stimulator was constructed consisting of a large capacitor that was discharged into a flat spiral coil placed near the porcine torso and centered below the heart. The discharge

created a damped sinusoidal magnetic field pulse whose amplitude depended on the capacitor voltage. The voltage was increased in small increments until cardiac capture, i. e., depolarization of the myocardium resulting in contraction, was observed on continuously acquired ECG, non-invasive blood pressure, and peripheral oximetry traces. Immediately after the stimulation experiment, fat-water-separated Dixon MR images of the pigs were acquired along with CINE images of the beating heart to create individualized whole-body computational models of each animal's anatomy. These models allowed to account for body size, posture, and heart position variations across the animals when calculating dB/dt and E-field values induced in the porcine heart at the threshold capacitor voltage. This approach thus presents an improvement over previous estimates of the E-field required to stimulate the heart, which were done in comparatively coarse generic torso models (Mouchawar et al., 1993; Ragan et al., 1995). Finally, the stimulation thresholds measured in the porcine heart were compared to maximum dB/dt and E-field values created by three commercial MRI gradient systems in the heart of a male human body model.

The third part of this thesis applies the coupled electromagnetic-electrodynamic cardiac fiber models of Part 1 to the individual porcine models to validate the overall modeling pipeline using the porcine experimental data obtained in Part 2. To this end, Purkinje and ventricular muscle fibers were added to the porcine body models derived from the MR images to simulate CS thresholds for the exact magnetic field distribution, waveform, and animal's anatomy used in the stimulation experiments. The predicted CS threshold was then compared to the measured threshold for each animal. Moreover, a sensitivity analysis of the predicted thresholds was conducted to assess their dependence on important simulation parameters such as electrical tissue conductivity and geometry of the cardiac fiber paths. These simulations present an important step towards understanding the origins of cardiac magnetostimulation and the extrapolation of thresholds measured in an animal model to the CS threshold of the human heart. Such an integrative approach of measurements and modeling is crucial in any future revision of safety limits for state-of-the-art MR imaging in humans.

2 THEORETICAL BACKGROUND

This chapter describes the theoretical principles relevant for the understanding of this work. The first two sections cover the basics of nuclear magnetic resonance (NMR) and magnetic resonance imaging (MRI), with a special focus on MRI gradient technology. A more detailed description of the concepts described in these sections can, e. g., be found in (Haacke et al., 1999). The third section introduces the theory behind magnetostimulation of peripheral nerves and the heart. Finally, the last section briefly describes the basic concepts of numerical modeling of tissue magnetostimulation.

2.1 NUCLEAR MAGNETIC RESONANCE

In 1922, Otto Stern and Walther Gerlach conducted an experiment in which they observed a quantization of the angular momentum of neutral silver atoms passing through a magnetic field gradient owing to the intrinsic spin of the unpaired 5s electron (Gerlach and Stern, 1922). Stern was awarded the Nobel Prize in Physics in 1943 "for his contribution to the development of the molecular ray method and his discovery of the magnetic moment of the proton". In the 1930s, Isidor Isaac Rabi and collaborators built upon this work and investigated the nuclear spin and its interaction with external magnetic fields (Rabi et al., 1938). Rabi conducted the first resonance experiment, and was awarded the Nobel Prize in Physics in 1944 "for his resonance method for recording the magnetic properties of atomic nuclei". In 1946, the research groups of Felix Bloch (Bloch, 1946) and Edward Mills Purcell (Purcell et al., 1946) measured precession signals from paraffin and water samples. With their work, they laid the foundation for NMR, and were jointly awarded the Nobel Prize in Physics in 1952 "for their development of new methods for nuclear magnetic precision measurements and discoveries in connection therewith".

2.1.1 *Nuclear spin and Zeeman effect*

Atomic nuclei consist of protons and neutrons, so-called *nucleons*. Both particles are fermions with spin quantum number $s = \frac{1}{2}$ and an orbital angular momentum with quantum numbers $l \geqslant 0$. The total angular momentum of a nucleon is thus given by the quantum number $j = |l \pm s| = |l \pm \frac{1}{2}|$. The total angular momentum $\hat{\vec{I}}$ of a nucleus is obtained by the sum over its nucleons and is commonly referred to as *nuclear spin*.

The hat symbol identifies a variable as a quantum-mechanical operator.

As an angular momentum operator, $\hat{\vec{I}} = \left(\hat{I}_x, \hat{I}_y, \hat{I}_z\right)$ fulfils the following commutator relations:

$$\begin{aligned} \left[\hat{I}_i, \hat{I}_j\right] &= i\hbar\epsilon_{ijk}\hat{I}_k \\ \left[\hat{I}_i, \hat{\vec{I}}^2\right] &= 0, \end{aligned} \tag{2.1}$$

where $\hbar = \frac{h}{2\pi} \approx 1.055 \cdot 10^{-34}$ Js denotes the reduced Planck constant. Choosing the z-axis as the axis of quantification, the eigenvalues of the nuclear spin magnitude $\hat{\vec{I}}^2$ and its projection onto the z-axis $\hat{I}_z$ are given by

$$\begin{aligned} \hat{\vec{I}}^2 |I, m\rangle &= I\,(I+1)\,\hbar^2 |I, m\rangle \\ \hat{I}_z |I, m\rangle &= m\hbar |I, m\rangle \end{aligned} \tag{2.2}$$

with the nuclear spin quantum number $I = 0, \frac{1}{2}, 1, \frac{3}{2}, \ldots$ and the magnetic quantum number $m \in \{-I, -I+1, \ldots, I-1, I\}$. The eigenvalues of $\hat{\vec{I}}^2$ and $\hat{I}_z$ can therefore only assume discrete values. Without an external magnetic field, the energy of a certain quantum state is independent of m and therefore $2\,(I+1)$-fold degenerate. In the case of protons $I = j = s = \frac{1}{2}$ holds, and $\hat{I}_z$ has two eigenvalues with

It is common nomenclature in NMR to refer to the magnetic flux density $\vec{B}$ as the "magnetic field", which has been adopted in this thesis.

$$m = \pm\frac{1}{2}. \tag{2.3}$$

Nuclei with nonzero nuclear spin $\hat{\vec{I}}$ also possess a nonzero magnetic moment, which can be expressed in terms of multiples of the nuclear magneton

$$\mu_N = \frac{e\hbar}{2m_p} \tag{2.4}$$

with the proton charge $e = 1.602 \cdot 10^{-19}$ C and the mass $m_p = 1.673 \cdot 10^{-27}$ kg. The magnetic moment is then given as

$$\hat{\vec{\mu}} = \frac{g\mu_N}{\hbar}\hat{\vec{I}} = \gamma\hat{\vec{I}}, \tag{2.5}$$

where g is the experimentally determined g-factor, and γ is the nucleus-specific gyromagnetic ratio. In the case of protons, $g \approx 5.586$ and $\gamma \approx 2.675 \cdot 10^8 \frac{\text{rad}}{\text{s}\cdot\text{T}}$, or, equivalently,

$$\frac{\gamma}{2\pi} = 42.58\ \frac{\text{MHz}}{\text{T}}. \tag{2.6}$$

The magnetic moment interacts with surrounding magnetic fields. In the presence of a magnetic field, the $(2I+1)$ degeneracy of spin states is lifted, a phenomenon referred to as the *Zeeman effect*. Figure 2.1 shows the Zeeman effect for a system with $I = \frac{1}{2}$ and positive γ, such as a proton. Let us assume, without loss of generality, that a static external magnetic field with $|\vec{B}| = B_0$ points along the z-axis:

Here, $\hat{z}$ denotes the unit vector pointing along the z-direction.

$$\vec{B} = B_0\hat{z}. \tag{2.7}$$

The interaction between this magnetic field and the magnetic moment of a resting proton can be described by the Hamiltonian operator

$$\hat{\mathcal{H}} = -\hat{\vec{\mu}} \cdot \vec{B} = -\gamma B_0 \hat{I}_z. \tag{2.8}$$

The Hamiltonian is time-independent, and therefore solving the the stationary Schrödinger equation

$$\hat{\mathcal{H}} |I, m\rangle = E_m |I, m\rangle \tag{2.9}$$

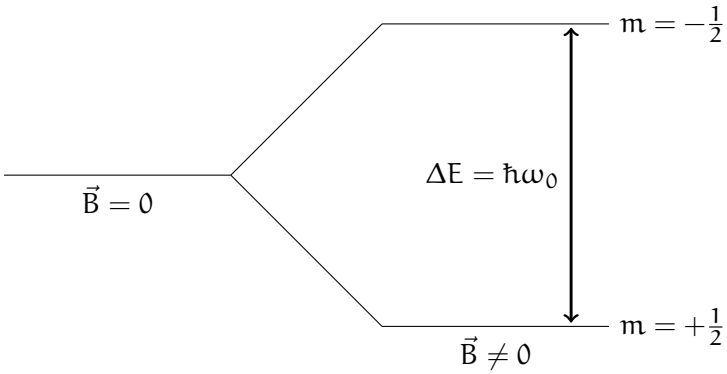

Figure 2.1: Zeeman splitting of energy levels for a system with nuclear spin $I = \frac{1}{2}$ and $\gamma > 0$, such as a proton. There are two energy eigenstates $E_m = \pm\frac{1}{2}\hbar\omega_0$. In the lower energy level, the spin is aligned "parallel" to $\vec{B}$ ("spin-up" state). In the higher energy level, it is aligned "anti-parallel" to $\vec{B}$ ("spin-down" state). Quantum mechanics dictates that in general, the spin is a superposition of both states.

yields the following equidistant energy eigenvalues E_m:

$$E_m = -\hbar m \gamma B_0 \tag{2.10}$$

with an energy difference of

$$\Delta E = E_{m+1} - E_m = \hbar\gamma B_0 = \hbar\omega_0 \tag{2.11}$$

between neighboring eigenstates. Transition between these states is possible by absorption or emission of a photon with a nucleus-specific frequency, the so-called *Larmor frequency*:

$$\omega_0 = \gamma B_0. \tag{2.12}$$

In NMR, transitions between the two spin eigenstates of the proton (Figure 2.1) are induced by the application of a magnetic field $\vec{B}_1(t)$ that oscillates at the Larmor frequency ω_0 (see Section 2.1.3).

2.1.2 *Macroscopic magnetization*

In NMR, the sample size is usually on the order of 1 mm^3. In the case of water, such a sample contains approximately $6.68 \cdot 10^{19}$ hydrogen atoms (assuming a molar hydrogen density of 111 M, and Avogadro's number $N_A \approx 6.022 \cdot 10^{23}$ mol^{-1}). For such macroscopic samples, it is feasible to consider the average behavior of a large number of spins rather than the spin dynamics of single protons. The macroscopic magnetization $\vec{M}$ of a sample of volume V is given by the sum of the expectation values of the magnetic moments $\hat{\vec{\mu}}_i$ of N individual spins:

$$\vec{M} = \sum_{i=1}^{N} \frac{\langle \hat{\vec{\mu}}_i \rangle}{V}. \tag{2.13}$$

At thermal equilibrium with temperature T, the occupation probability of the energy eigenstates E_m is described by the *Boltzmann distribution*

$$p_m = \frac{1}{Z} e^{-\frac{E_m}{k_B T}}, \tag{2.14}$$

where $k_B \approx 1.381 \cdot 10^{-23} \frac{J}{K}$ is the Boltzmann constant, and Z denotes the state sum:

$$Z = \sum_{m=-I}^{I} e^{-\frac{E_m}{k_B T}}. \tag{2.15}$$

Assuming $\vec{B} = B_0 \hat{z}$, Equation 2.13 can be expressed by

$$\vec{M} = \frac{N}{V} \gamma \hbar \sum_{m=-I}^{I} p_m m \hat{z}. \tag{2.16}$$

In the case of protons ($I = \frac{1}{2}$), the ratio of the number of spins $N_{\pm\frac{1}{2}}$ populating the two energy eigenstates with $m = \pm\frac{1}{2}$ is given by

$$\frac{N_{+\frac{1}{2}}}{N_{-\frac{1}{2}}} = \frac{p_{+\frac{1}{2}}}{p_{-\frac{1}{2}}} = e^{\frac{\Delta E}{k_B T}} = e^{\frac{\hbar \gamma B_0}{k_B T}}. \tag{2.17}$$

Assuming a magnetic field strength of $B_0 = 3$ T and a human body temperature of $T \approx 310$ K, the number of spins in the lower-energy $m = +\frac{1}{2}$ state (spin-up state) exceed the number of spins in the higher-energy $m = -\frac{1}{2}$ state (spin-down state) by approximately 20 parts per million (ppm). Thus, the number of spins contributing to the macroscopic magnetization $\vec{M}_0$ is very small. For protons, Equation 2.16 becomes

$$\vec{M} = \frac{N}{2V} \gamma \hbar \tanh\left(\frac{\hbar \gamma B_0}{2 k_B T}\right) \hat{z}. \tag{2.18}$$

For the temperature T of the human body $\hbar \gamma B_0 \ll k_B T$ holds. Consequently, the macroscopic magnetization can be approximated as

$$\vec{M} \approx \frac{N}{V} \frac{\hbar^2 \gamma^2}{4 k_B} \frac{B_0}{T} \hat{z}, \tag{2.19}$$

The Taylor series of tanh *is* $x + \mathcal{O}(x^3)$.

using the Taylor expansion of $\tanh(x)$ to the first order. This shows that the net magnetization is approximately proportional to the magnetic field strength B_0, the spin density $\frac{N}{V}$, and the square of the gyromagnetic ratio γ.

2.1.3 *Signal excitation*

While the spin dynamics of single nuclei are governed by quantum-mechanical laws, the dynamics of a macroscopic spin sample can be described using classical physics. According to classical mechanics, a magnetic moment $\vec{\mu}$ inside an external magnetic field $\vec{B} = B_0 \hat{z}$ experiences a torque. The resulting motion of the magnetic moment can be described by

$$\frac{d\vec{\mu}}{dt} = \vec{\mu} \times \gamma \vec{B}. \tag{2.20}$$

If $\vec{\mu}$ is not perfectly aligned with $\vec{B}$, i. e., if there is a component of $\vec{\mu}$ transverse to $\vec{B}$, $\vec{\mu}$ will start to precess around the magnetic field axis (here: the z-axis). This precession occurs at the Larmor frequency $\omega_0 = \gamma B_0$. For the magnetization vector

of a macroscopic sample (see Equation 2.13) in which the spins do not interact, Equation 2.20 becomes

$$\frac{d\vec{M}}{dt} = \vec{M} \times \gamma \vec{B}. \tag{2.21}$$

In thermal equilibrium, all individual spins that contribute to the macroscopic magnetization $\vec{M} = M_0 \hat{z}$ precess at the same frequency ω_0 around the z-axis. However, they have no phase coherence, and thus their transverse components sum up to zero. This means that the net magnetization vector $\vec{M}$ is aligned with the z-axis (*longitudinal magnetization* $M_z = M_0$), and has no component perpendicular to $\vec{B}$ in the x-y-plane (*transverse magnetization* $M_x = M_y = 0$). The magnetization $\vec{M}$ thus has to be tipped out of its alignment with $\vec{B}$ to make it precess around the z-axis, and to allow measurement of a non-zero transverse magnetization M_{xy} via Faraday induction (Equation 2.39).

This can be achieved by the application of a second, time-dependent magnetic field $\vec{B}_1(t)$ in the plane perpendicular to $\vec{B}$ (here: the x-y-plane). This magnetic field is commonly referred to as the *radiofrequency (RF) field*. To investigate the motion of the magnetization in presence of $\vec{B}_1(t)$, it is advantageous to switch from the laboratory frame to a reference frame rotating at the angular velocity $\vec{\Omega}$:

$$\frac{d\vec{F}}{dt} = \left(\frac{d\vec{F}}{dt}\right)' + \vec{\Omega} \times \vec{F}. \tag{2.22}$$

Here, the prime denotes the rotating reference frame and $\vec{F}$ is a generic vector function. Applying Equation 2.22 to Equation 2.21 yields

$$\left(\frac{d\vec{M}}{dt}\right)' = \vec{M} \times \gamma \left(\vec{B} + \frac{\vec{\Omega}}{\gamma}\right) = \vec{M} \times \gamma \vec{B}_{\text{eff}}. \tag{2.23}$$

In the rotating frame, $\vec{M}$ thus precesses around an effective magnetic field $\vec{B}_{\text{eff}} = \vec{B} + \frac{\vec{\Omega}}{\gamma}$.

Consider a left-circularly polarized RF field that takes the form

$$\vec{B}_1(t) = B_1 \begin{pmatrix} \cos(\omega_1 t) \\ -\sin(\omega_1 t) \\ 0 \end{pmatrix} \tag{2.24}$$

with the frequency ω_1. The motion of the magnetization in the laboratory frame is given by

$$\frac{d\vec{M}}{dt} = \vec{M} \times \gamma \left(\vec{B} + \vec{B}_1\right). \tag{2.25}$$

In a reference frame that rotates around the z-axis with frequency $\vec{\Omega} = -\omega_1 \hat{z}$,

$$\left(\frac{d\vec{M}}{dt}\right)' = \vec{M} \times \gamma \left(B_1 \hat{x}' + \left(B_0 - \frac{\omega_1}{\gamma}\right) \hat{z}'\right) \tag{2.26}$$

with

$$\hat{x}' = \hat{x} \cos(\omega_1 t) - \hat{y} \sin(\omega_1 t) \tag{2.27}$$

and $\hat{z}' = \hat{z}$. According to Equation 2.26, the precession of $\vec{M}$ around the z-axis vanishes if $\omega_1 = \omega_0$, in which case $\vec{M}$ only rotates around $\hat{x}'$. This means that the energy transfer between the RF field and the magnetization is most efficient if $\vec{B}_1$ oscillates at the Larmor frequency ω_0 *(resonance condition)*. The rotation angle α of the magnetization around $\hat{x}'$ depends on the duration τ and the time-dependent amplitude $B_1(t)$ of the RF field:

$$\alpha = \int_0^\tau \gamma B_1(t')dt'. \tag{2.28}$$

An RF field applied for a short duration to tip the magnetization out of its alignment with the z-axis is commonly referred to as an *RF pulse*.

2.1.4 *Bloch equations and relaxation*

The RF field transfers energy into the spin system. After the RF pulse, the longitudinal magnetization M_z regrows to its initial value with a constant rate $1/T_1$, while the transverse magnetization M_{xy} decays with a constant rate $1/T_2$. These decay processes are referred to as longitudinal and transverse relaxation.

BLOCH EQUATIONS In 1946, Felix Bloch (Bloch, 1946) derived the equation of motion for the macroscopic magnetization $\vec{M}$ in the presence of an external magnetic field $\vec{B}$ taking into account relaxation effects:

Here, it is again assumed that $\vec{B} = B_0\hat{z}$.

$$\frac{d\vec{M}}{dt} = \vec{M} \times \gamma\vec{B} + \frac{1}{T_1}(M_0 - M_z)\,\hat{z} - \frac{1}{T_2}\vec{M}_\perp \tag{2.29}$$

with $\vec{M}_\perp = M_x\hat{x} + M_y\hat{y}$. This equation can be split up into the three magnetization components:

$$\frac{dM_x}{dt} = \gamma\left(\vec{M} \times \vec{B}\right)_x - \frac{M_x}{T_2} \tag{2.30}$$

$$\frac{dM_y}{dt} = \gamma\left(\vec{M} \times \vec{B}\right)_y - \frac{M_y}{T_2} \tag{2.31}$$

$$\frac{dM_z}{dt} = \gamma\left(\vec{M} \times \vec{B}\right)_z + \frac{M_0 - M_z}{T_1} \tag{2.32}$$

The solutions to the Bloch equations in the rotating frame of reference are given by Equation 2.34 and Equation 2.36.

LONGITUDINAL RELAXATION T_1 relaxation or *longitudinal relaxation* results from the interaction of each spin with surrounding nuclei, atoms, and molecules, the so-called "lattice" (this term is derived from early NMR experiments in solids, i. e., crystalline lattices). The process is also referred to as *spin-lattice relaxation*. The spins transfer energy to their environment via collisions, rotations, and electromagnetic (EM) interactions in the form of heat. The relaxation process of the longitudinal magnetization component M_z is characterized by a decay constant T_1:

$$\frac{dM_z}{dt} = \frac{M_0 - M_z}{T_1}. \tag{2.33}$$

The solution to this equation is given by an exponential regrowth of M_z to the equilibrium value M_0:

$$M_z(t) = M_z(0)e^{-\frac{t}{T_1}} + M_0\left(1 - e^{-\frac{t}{T_1}}\right) \tag{2.34}$$

with $M_z(0)$ the longitudinal magnetization component immediately after application of the RF pulse. Typical T_1 relaxation times for protons in biological tissues range between tens and thousands of milliseconds for magnetic field strengths of interest in MRI (Haacke et al., 1999).

TRANSVERSE RELAXATION T_2 relaxation or *transverse relaxation* results from interactions of neighboring spins with each other, and is therefore also referred to as *spin-spin relaxation time*. The magnetic field experienced by a spin is a superposition of the static external field $\vec{B}$ and the local field $\vec{B}_{loc}(t)$ generated by neighboring spins. Brownian motion causes fluctuations in the local magnetic field, which lead to local variations in the precession frequency. The frequency variations in turn cause the spins to lose their relative phase coherence, or to "dephase" over time. As a result, the transverse magnetization $M_\perp$ decays with a decay constant T_2 in the rotating frame of reference:

$$\frac{dM'_\perp}{dt} = -\frac{1}{T_2}M'_\perp \tag{2.35}$$

The solution to this equation is given by an exponential decay:

$$M'_\perp(t) = M'_\perp(0)e^{-\frac{t}{T_2}} \tag{2.36}$$

with $M'_\perp(0)$ being the transverse magnetization component immediately after application of the RF pulse. The decay constant T_2 assumes values on the order of tens of milliseconds in most biological tissues (e. g., 60 ms in fat at $B_0 = 1.5$ T (Haacke et al., 1999)) and significantly higher values in liquids (e. g., 2200 ms in cerebrospinal fluid at $B_0 = 1.5$ T (Haacke et al., 1999)). Naturally, any process that causes T_1 relaxation also results in a loss of phase coherence in the transverse plane, thus causing T_2 relaxation. In addition, T_2 relaxation processes can also occur independently of T_1 relaxation. It thus generally holds that

$$T_2 \leqslant T_1. \tag{2.37}$$

The decay constant T_2 describes dephasing due to spin and molecular interactions. In reality, $M_\perp$ decays much faster due to local inhomogeneities in the magnetic field caused by magnet imperfections and object-specific, susceptibility-induced field distortions. The decay due to these inhomogeneities is characterized by a decay constant T'_2. The total observed decay is described with a decay constant T^*_2 defined as

$$\frac{1}{T^*_2} = \frac{1}{T_2} + \frac{1}{T'_2}. \tag{2.38}$$

Here, the prime is common notation for the reversible transverse decay constant and does not refer to the rotating frame of reference.

The impact of T'_2 is reversible and can be removed by the application of a 180° RF pulse (see Section 2.1.6).

2.1.5 *Signal reception*

Transverse components of the magnetization precessing in the x-y-plane can be measured via Faraday induction in a receive or RF coil placed perpendicularly to the static magnetic field axis, i. e., the z-axis. After application of an RF pulse, the perpendicular magnetization $\vec{M}_\perp = \vec{M}_{xy}$ rotates around the z-axis, creating a time-varying magnetic flux density $\frac{d\Phi(t)}{dt}$, which induces an oscillating voltage U_{ind} in the receive coil according to Faraday's law of induction:

$$U_{ind}(t) = -\frac{d\Phi(t)}{dt} = -\frac{d}{dt}\int_V \vec{M}_\perp\left(\vec{r}', t\right)\vec{B}_1^-\left(\vec{r}'\right)d\vec{r}'. \tag{2.39}$$

Here, V is the volume of the sample and $\vec{B}_1^-$ is the receive field of the RF coil. In contrast, the RF transmit field used for spin excitation is often denoted as the "$\vec{B}_1^+$ field". The oscillating voltage or signal decays exponentially over time due to spin dephasing (see Section 2.1.4):

$$U_{ind}(t) \propto S(t) = S_0 e^{-i\gamma B_0 t} e^{-\frac{t}{T_2}} \int_V \rho\left(\vec{r}'\right)d\vec{r}'. \tag{2.40}$$

This is the fundamental signal measured in an NMR experiment. It is commonly referred to as *free induction decay (FID)*.

2.1.6 *Spin echo pulse sequence and Dixon method*

As explained in the previous sections, the NMR signal decays quickly with a decay constant T_2^* owing to magnetic field inhomogeneities. This effect can be removed by the application of an $\alpha = 180°$ RF pulse between signal excitation and reception, e. g., along the x'-axis. This pulse rotates the dephasing spins around x' such that the spins with higher precession frequency are behind the spins with lower precession frequency. This causes the spins to rephase, which leads to an increase in signal amplitude, the so-called "echo". If the 180° pulse is applied at $t = TE/2$, the echo occurs at TE, the *echo time*. The amplitude of the echo decays with the "true" transverse decay constant T_2 and is independent of T_2' effects. The combination of a 90° pulse for spin excitation with a 180° pulse for spin rephasing is referred to as *spin echo (SE)* pulse sequence.

The spin echo was discovered in 1949 by the physicist Erwin Hahn (Hahn, 1950).

The *Dixon method* is a technique that allows to separate fat and water signals (Dixon, 1984), and is mainly used for abdominal imaging. The method is based on the fact that fat and water protons have a slightly different resonance frequency $\Delta\omega$ owing to the differences in their molecular environments. This means that fat and water spins go in- and out-of-phase with each other as a function of time with a *phase cycling* period of $1/\Delta\omega$. The Dixon method exploits this phase cycling through the acquisition of two spin echo images with slightly different TE values. In one image, the fat and water signals are in-phase at the center of the echo, in the other image they are out-of-phase. The in-phase image I_{IP} and the out-of-phase image I_{OP} are thus a combination of the fat and water signals I_{fat} and I_{water}:

The Dixon method can be combined with a variety of pulse sequences, e. g., a spin echo sequence.

$$I_{IP} = I_{water} + I_{fat} \tag{2.41}$$

$$I_{OP} = I_{water} - I_{fat}, \tag{2.42}$$

and the fat- and water-weighted images can be calculated as

$$I_{water} = 0.5 \cdot (I_{IP} + I_{OP}) \tag{2.43}$$

$$I_{fat} = 0.5 \cdot (I_{IP} - I_{OP}) . \tag{2.44}$$

The last paragraph already alluded to the concept of NMR *images*. The following section will explain how these images can be obtained from measured NMR signals.

2.2 MAGNETIC RESONANCE IMAGING

Raymond V. Damadian was the first to discover that human cancer cells have different T_1 and T_2 relaxation times than healthy tissue (Damadian, 1971). He was also the first to acquire whole-body MR images in 1977 using a saddle-shaped magnetic field that was resonant at only a single point (Damadian et al., 1977), although this imaging method was inherently very slow. Paul C. Lauterbur and Sir Peter Mansfield showed that the addition of a spatially varying magnetic field causes a position-dependence of the spin resonance frequency, and thus allows localization of the spin signal in clinically acceptable times (Lauterbur, 1973; Mansfield and Grannell, 1973). They were jointly awarded the Nobel Prize in Physiology or Medicine in 2003 "for their discoveries concerning magnetic resonance imaging". Lauterbur, Mansfield, and Damadian laid the groundwork for modern MRI, which uses the principles of NMR discussed in the previous section to acquire tomographic images of an object or patient. MRI achieves excellent soft tissue contrasts based on the vastly different relaxation times (see Section 2.1.4) as well as spin densities ρ of different biological tissues and has thus gained great importance as a diagnostic medical imaging modality. The following discussions of spatial signal encoding will neglect the influence of relaxation processes for simplicity.

2.2.1 *Spatial encoding and k-space*

The NMR signal needs to be localized in space to form images. This is achieved by the use of so-called *gradient fields*, whose z-component varies linearly inside the imaging volume. Superposition of a linear magnetic gradient field

$$\vec{G} = \left(\frac{dB_z}{dx}, \frac{dB_z}{dy}, \frac{dB_z}{dz} \right) = (G_x, G_y, G_z) \tag{2.45}$$

to the static magnetic field $\vec{B} = B_0 \hat{z}$ causes a spatial variation of the spins' precession frequency according to

$$\omega(\vec{r}) = \gamma B_{tot}(\vec{r}) = \omega_0 + \omega_G(\vec{r}) = \gamma \left(B_0 + \vec{G}\vec{r} \right) . \tag{2.46}$$

In general, the gradient field amplitude is time-dependent: $G = G(t)$. The precession frequency of the spin system can be determined after the measurement via Fourier analysis, which allows to reconstruct the spatial location of the acquired signal. In two-dimensional MRI, three spatial encoding steps are required to reconstruct tomographic images from the measured signals. These steps are referred to as slice selection, frequency encoding, and phase encoding, each of which is applied along one spatial direction.

SLICE SELECTION The application of a gradient field along one spatial direction (here, without loss of generality, the z-direction) creates a z-dependent precession frequency:

$$\omega(z) = \gamma(B_0 + G_z z). \tag{2.47}$$

If an RF pulse with frequency ω_{RF} is applied simultaneously with the gradient field G_z, only spins in an xy-plane at $z = \omega_{RF}/(\gamma G_z)$ precess at the resonance frequency and can thus be excited. For practical reasons, the RF pulse has a finite length and thus contains not a single frequency but a certain *bandwidth* $\Delta\omega$ of frequencies. Therefore, spins are excited in a slice with thickness

$$\Delta z = \frac{\Delta\omega}{\gamma G_z}. \tag{2.48}$$

The greater the gradient field amplitude G_z, the smaller the thickness of the excited slice becomes for a given RF bandwidth $\Delta\omega$. The slice profile depends on the frequency content of the RF pulse. Usually, a truncated sinc pulse is used to achieve a rectangular slice profile.

The Fourier transform of a sinc function in the frequency domain is a rectangular function in the spatial domain.

Since the gradient field G_z is applied for a finite time, it is often referred to as a *gradient pulse*, similarly to the RF pulse. Assuming that the RF pulse is applied after the first half of the gradient pulse duration τ and flips the magnetization instantaneously into the transverse plane, the spins dephase due to the second half of G_z, which can lead to signal loss. The dephasing can be reversed by the application of a second gradient pulse that has the opposite *polarity*, i. e., opposite sign of the gradient field amplitude, and is applied for half of the duration $\frac{\tau}{2}$ of the first gradient pulse.

FREQUENCY ENCODING After slice selection, only the two in-plane directions (here: x and y) have to be spatially encoded. Application of a *frequency-encoding gradient* G_x along the x-direction during the signal acquisition leads to a spatial dependence of the precession frequency along x:

$$\omega(x) = \gamma(B_0 + G_x x). \tag{2.49}$$

The measured signal is now a superposition of signals with different frequencies, which can be analyzed and assigned to a certain location along x using a one-dimensional Fourier transform. The received NMR signal is given by

$$S(t, G_x) = S(t) \int e^{-i\gamma \int_0^t G_x(t')x\,dt'} dx \tag{2.50}$$

with $S(t)$ given by Equation 2.40 neglecting relaxation effects.

PHASE ENCODING Spatial encoding along the second in-plane direction can be achieved by the application of a *phase-encoding gradient* between signal excitation and reception. The application of a gradient G_y with duration τ_y results in an accumulated phase

$$\Phi_{G_y}(y) = -\int_0^{\tau_y} \omega_{G_y}(y, t')\,dt' = -\gamma y \int_0^{\tau_y} G_y(t')\,dt'. \tag{2.51}$$

After application of the phase-encoding gradient, all spins precess at the same frequency again, but have a different phase that linearly depends on y. The phase encoding step is repeated N_y times with gradient amplitudes G_y varying between $-G_{y,max}$ and $+G_{y,max}$. This results in a set of N_y linear equations that can be solved for the phase and thus the location of the signal along y. The received NMR signal is given by

$$S\left(t, \tau_y, G_y\right) = S(t) \int e^{-i\gamma \int_0^{\tau_y} G_y(t')y dt'} dy. \tag{2.52}$$

In three-dimensional (3D) MRI the slice selection step is omitted and phase encoding is applied along the two spatial directions perpendicular to the frequency encoding direction.

K-SPACE The total received signal in two-dimensional MRI is given by

$$S\left(t, \vec{G}\right) = S_0 \int\int \rho\left(x, y\right) e^{-i\gamma\left(\int_0^t G_x(t')x dt' + \int_0^t G_y(t')y dt'\right)} dx dy. \tag{2.53}$$

Defining the wave vector $\vec{k}$ according to

$$\vec{k} = \frac{\gamma}{2\pi} \int_0^t \vec{G}\left(t'\right) dt' = \left(k_x, k_y, k_z\right) \tag{2.54}$$

simplifies Equation 2.53 to

$$\begin{aligned} S\left(\vec{k}\right) &= S_0 \int\int \rho\left(x, y\right) e^{-2\pi i\left(k_x x + k_y y\right)} dx dy && (2.55)\\ &= S_0 \int \rho\left(\vec{r}\right) e^{-2\pi i \vec{k}\vec{r}} d\vec{r} && (2.56)\\ &= S_0 \cdot \left(\mathcal{F}\rho\right)\left(\vec{r}\right). && (2.57) \end{aligned}$$

Here, $\mathcal{F}$ is the two-dimensional Fourier transform. $S\left(\vec{k}\right)$ is the received signal sampled in the spatial frequency domain, which in MRI is commonly referred to as *k-space*. The spin density ρ can be obtained from the measured signal in *k-space* via an inverse Fourier transform:

$$\rho\left(\vec{r}\right) = S_0^{-1} \int S\left(\vec{k}\right) e^{2\pi i \vec{k}\vec{r}} d\vec{k}. \tag{2.58}$$

In practice, $S\left(\vec{k}\right)$ is not measured continuously but at discrete points in k-space. To this effect, the wave vector $\vec{k}$ assumes discrete values through variations of the gradient moment, i. e., the integrated gradient pulse, and the RF pulse. The most common trajectory chosen to traverse or sample k-space is Cartesian with k-space increments Δk_x in frequency encoding direction and Δk_y in phase encoding direction:

$$\begin{aligned} \Delta k_x &= \frac{\gamma}{2\pi} G_x \Delta t_x && (2.59)\\ \Delta k_y &= \frac{\gamma}{2\pi} \Delta G_y \tau_y. && (2.60) \end{aligned}$$

In the case of frequency encoding, a constant gradient G_x is applied for a duration τ_x and the signal is sampled at N_x discrete time points with increments $\Delta t_x = \frac{\tau_x}{N_x}$.

For phase encoding, a gradient G_y is applied for a duration τ_y before signal reception. This step is repeated N_y times with phase encoding gradient strengths varying between $-G_{y,max}$ and $+G_{y,max}$ with increments of $\Delta G_y = \frac{2G_{y,max}}{N_y}$. The extent of the imaging volume, the so-called *field-of-view (FOV)*, in the frequency and phase encoding directions is determined by the k-space increments:

$$FOV_x = \frac{1}{\Delta k_x} \tag{2.61}$$

$$FOV_y = \frac{1}{\Delta k_y}. \tag{2.62}$$

Consequently, the image pixel size is given by

$$\Delta x = \frac{FOV_x}{N_x} = \frac{2\pi}{\gamma G_x \Delta t_x N_x} \tag{2.63}$$

$$\Delta y = \frac{FOV_y}{N_y} = \frac{2\pi}{\gamma \Delta G_y \tau_y N_y}. \tag{2.64}$$

These equations demonstrate how the pixel size, and thus the spatial image resolution, depend on the gradient field strength G.

2.2.2 *Gradient coils*

Each spatial component of the total magnetic gradient field $\vec{G}$ is created by a separate coil. Gradient systems therefore consist of three coils, which are referred to as X-axis, Y-axis, and Z-axis coils. As described above, the *z*-component of a gradient field varies linearly along one spatial dimension within the FOV. However, to satisfy Gauss's law for magnetism (Equation 2.74), gradient fields must have non-zero components in the xy-plane, so-called *concomitant field* terms. They are in general negligible for most imaging techniques, but do contribute to physiological effects discussed in the following section (Section 2.3). Figure 2.2 shows the total magnetic field magnitude $|\vec{B}|$ and the *z*-component B_z of the commercially available, actively shielded Siemens Sonata gradient coil (Y-axis). The B_z component varies linearly along y within the FOV. The largest magnetic field values are reached outside of the FOV, as can be seen on the $|\vec{B}|$-field map.

Shielding minimizes the magnetic field outside of the gradient coil, and thus reduces unwanted eddy currents on, e. g., the cryostat.

The performance of MRI gradient systems is usually characterized by the gradient field amplitude or gradient strength G, measured in mT/m, and the slew rate SR, measured in T/m/s. The maximum slew rate is defined as

$$SR_{max} = \frac{G_{max}}{t_{rise}}, \tag{2.65}$$

where G_{max} is the maximum gradient field amplitude and t_{rise} is the minimum rise time it takes to achieve G_{max}, starting from 0 mT/m (Figure 2.3). It is determined by the inductance L of the gradient coil and the voltage U of the gradient power amplifier (GPA), which is typically on the order of 2000 V:

$$SR = \frac{\epsilon_G}{L} \cdot U, \tag{2.66}$$

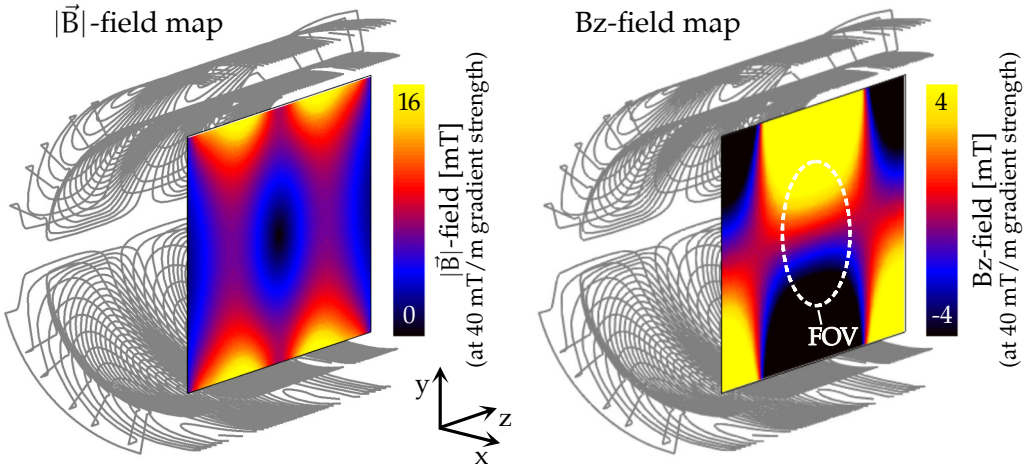

Figure 2.2: Total magnetic field magnitude $|\vec{B}|$ and z-component B_z of the Siemens Sonata gradient (Y-axis coil, Siemens Healthineers, Erlangen, Germany) in the central coronal slice (y-z-plane). The dashed line indicates the imaging FOV, within which the B_z component varies linearly among the gradient direction (here: y).

with ϵ_G being the gradient efficiency, i. e., the gradient strength per unit current. The slew rate indicates how fast the gradient field can be switched, and thus how fast k-space can be sampled. High slew rate values are especially important for fast imaging sequences like *echo-planar imaging (EPI)*, which cover the whole k-space in one or only few RF excitations (Mansfield and Maudsley, 1977). High gradient field amplitudes, on the other hand, are required for high-resolution imaging (Equation 2.63) and, e. g., for diffusion encoding (Le Bihan and Breton, 1985). Typical slew rates for whole-body gradient systems range around 200 T/m/s with gradient strengths between 40 mT/m and 80 mT/m. Special-purpose gradient systems such as head gradients can reach slew rates of up to 500 T/m/s and gradient strengths of up to 200 mT/m (Tan et al., 2020). Another important parameter is the *gradient non-linearity*, which describes the deviation of the gradient field from the ideal linear B_z variation in the imaging FOV. Gradient non-linearities can result in image distortions caused by a loss of the linear relationship between precession frequency and spatial location (Equation 2.46). Such distortions need to be corrected for in the reconstructed images.

2.3 MAGNETOSTIMULATION OF PERIPHERAL NERVES AND THE HEART

According to Faraday's law of induction (Equation 2.75), time-varying magnetic fields $d\vec{B}/dt$ induce electric fields $\vec{E}$ (E-fields). These E-fields cause a current flow in conductive tissues in the body that can stimulate excitable tissues such as peripheral nerves (Cohen et al., 1990; Mansfield and Harvey, 1993; Nyenhuis and Gross, 2019; Schenck, 2013), the brain (Hallett, 2000), the retina (Lövsund et al., 1980; Magnusson and Stevens, 1911), or the heart (Bourland et al., 1991; Mouchawar et al., 1992; Nyenhuis et al., 1992; Yamaguchi et al., 1991, 1992, 1994).

In the following, the magnitudes of $d\vec{B}/dt$ and $\vec{E}$ will simply be referred to as dB/dt and E.

Tissue stimulation through magnetically induced E-fields is referred to as *magnetostimulation*. In contrast, *electrostimulation* denotes tissue stimulation by electric

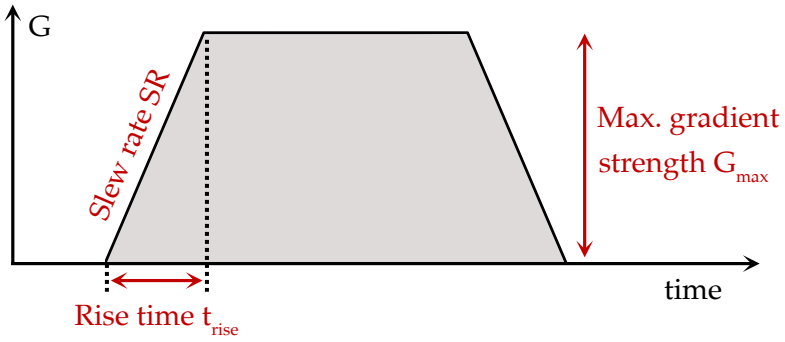

Figure 2.3: Definition of gradient field amplitude G and rise time t_{rise}, during which the gradient field is slewed from zero to maximum gradient strength G_{max}. The slew rate (SR) is defined as the ratio of G_{max} and t_{rise}, and thus indicates how fast the gradient field can be switched.

currents generated by electrodes attached to the skin or placed in direct contact with the respective tissue. Electrostimulation is routinely used for diagnostic and therapeutic purposes, e. g., in nerve conduction studies (Daube, 2012), chronic pain treatment (Parker et al., 2018), and in cardiac pacemaker systems (Coates and Thwaites, 2000). Magnetostimulation, on the other hand, is, e. g., employed in transcranial magnetic stimulation (TMS), which uses switching magnetic fields to stimulate the brain. TMS is utilized to monitor and treat depression or obsessive-compulsive disorder (Fitzsimmons et al., 2022), Parkinson's (Elahi et al., 2009) and Alzheimer's disease (Freitas et al., 2011), to name but a few examples. Magnetostimulation is less invasive than electrostimulation, as it does not require passing high currents through the patient's skin, which can be painful (Hallett, 2000). However, significantly higher energies are required for magnetostimulation (Mouchawar et al., 1992), and it is thus less widely used in clinical applications.

In MRI, E-fields are induced in the patient by the time-varying magnetic gradient fields employed for spatial encoding described in the previous section, leading to unwanted stimulation of peripheral nerves and potentially the heart. This section explains the basic anatomy and physiology of electrically excitable structures in peripheral nerve fibers and the heart. Particular emphasis is placed on nerve and cardiac magnetostimulation, i. e., stimulation by time-varying magnetic fields. The following part describes the strength-duration curve, which is often used to quantify tissue stimulation thresholds. Finally, a brief overview is provided on how MRI is affected by unwanted tissue stimulation and which safety regulations are applied to prevent or minimize its occurrence.

2.3.1 *The peripheral nervous system*

The mammalian peripheral nervous system encompasses all nerves in the body outside the brain or the spinal cord, which form the central nervous system (CNS). Peripheral nerves pass on electrical signals from the CNS to organs and extremities and back. Peripheral nerves consist of several bundles of peripheral nerve fibers.

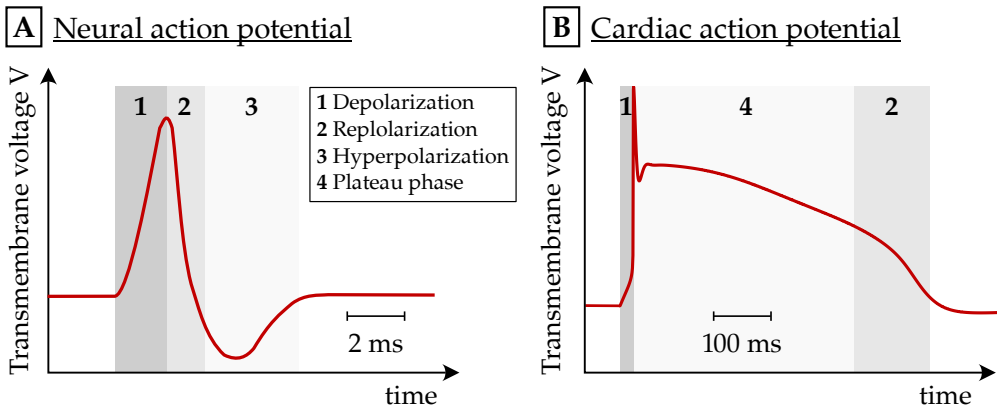

Figure 2.4: Typical action potentials of a nerve cell (A) and a cardiomyocyte (B). Note the different time scales.

The core of each nerve fiber is the axon, an elongated cell that can conduct electrical signals from the cell body to the peripheral end of the fiber. Large mammalian nerve fibers are usually myelinated, meaning that parts of the axon are wrapped in a fatty myelin sheath, which consists of several layers of Schwann cells. The myelin sheath provides electrical insulation from the extracellular space and thus makes signal conduction along the fiber faster. Between Schwann cells are regularly spaced unmyelinated regions, these parts of the nerve fiber are termed "nodes of Ranvier". At the nodes of Ranvier the axon is populated by voltage-dependent sodium and potassium ion channels and pumps. Ion channels are large transmembrane proteins with aqueous pores through which ions can flow (Izhikevich, 2007). The channels have gating particles that can activate ("open") or inactivate ("close") the channel. The gating mechanisms are described mathematically in Section 2.4.2.

In the resting state, the nerve membrane maintains a constant ionic concentration gradient between the intra- and extracellular space. The intracellular space is mainly occupied by potassium ions, while the extracellular space is mainly occupied by sodium ions. This results in a transmembrane voltage (TMV). In the equilibrium state, the TMV is at $V_{rest} = -70$ mV. During excitation, some sodium channels open, leading to a sodium influx into the cell and an increase in TMV (depolarization). Once the voltage passes a value of ca. -50 mV, all sodium channels open and the TMV increases rapidly to ca. $+30$ mV. The potassium channels are also activated by the increasing TMV but open more slowly than the sodium channels. After the depolarization phase, the outward potassium current is strong enough to cause a decrease in TMV (repolarization) until the nerve's resting potential is re-established. Potassium ions continue to flow out of the cell even after repolarization, which can result in a transitory period in which the TMV falls below its resting value (hyperpolarization). The characteristic rise and fall of TMV is the *action potential (AP)* (Figure 2.4). Following the AP, sodium-potassium pumps re-establish the intra- and extracellular ion concentrations at equilibrium. Neighboring parts of the nerve fiber membrane are still at rest during the AP, which causes a current to flow along the axon. This current in turn depolarizes the next patch of membrane, thus conducting the AP along the nerve fiber.

2.3.2 *Excitable cardiac tissue*

Just like peripheral nerves, the heart muscle (myocardium) is an electrically excitable organ that propagates stimuli in the form of APs. The duration of a typical cardiac AP is between 200 ms and 400 ms (Antoni, 1998), which is significantly longer than the AP of peripheral nerves or skeletal muscle (Figure 2.4). As in nerve fibers, cardiac APs are created by an interplay of TMV changes and ionic currents (most importantly Na^+, K^+, and Ca^{2+}). After the initial depolarization spike, during which the TMV quickly rises from the resting state (between −90 mV and −75 mV (O'Hara et al., 2011; Stewart et al., 2009)) to its initial peak (around +30 mV), the cardiac AP has a long plateau phase (around 0 mV) before the membrane repolarizes and returns to its resting state. During the plateau phase, the heart is refractory, i. e., it is difficult to initiate a new AP. This refractory state allows enough time for the heart chambers to contract and relax before the next stimulus can be propagated through the myocardium (Antoni, 1998).

Electrical excitation of the heart is normally initiated spontaneously by the sinoatrial (SA) node located in the inner wall of the right atrium, from where it spreads out over the atrial myocardium, initiating atrial contraction. The impulse then propagates through the atrioventricular (AV) node to the ventricles with a short delay which allows atrial contraction to be completed before the ventricles are excited. From the AV node, the signal is conducted through the bundle of His fibers into the Purkinje fibers.

In humans and canines, cardiac Purkinje fibers form a dense network in the ventricular muscle wall underneath the endocardium, and their task is to distribute the electrical signal rapidly throughout the ventricles to allow for uniform excitation and contraction (Boyden et al., 2010). In addition to this subendocardial network, some species such as pigs or sheep have free-running Purkinje fibers running radially through the heart muscle wall (De Almeida et al., 2015; Garcia-Bustos et al., 2017; Sedmera and Gourdie, 2014). Purkinje fibers consist of electrically excitable cylindrical cells, which are specialized in fast signal conduction. The diameter of human Purkinje cells is up to 70-80 µm (Legato, 1973). Individual cells are connected end-to-end by intercalated discs, forming fiber-like structures. The intercalated discs contain gap junctions that allow efficient conduction of APs by passage of ions between the cells. Purkinje fibers are part of the heart's natural pacemaking system. They can generate and conduct APs even in the absence of external electrical stimuli (Antoni, 1998). This autorhythmicity of the Purkinje fibers can keep the heart beating even if any of the upstream components of the pacemaking system (e. g., the SA or AV nodes) fail to function. The electrical signal generated in the Purkinje fibers is normally overridden by the signal generated in the SA and AV nodes since the Purkinje fibers have a lower AP firing frequency than the nodes.

The Purkinje fibers pass the excitation signal on to cells in the ventricular myocardium (cardiomyocytes), which are capable of both electrical excitation and contraction. Human ventricular cardiomyocytes reach lengths of up to 100 µm, and diameters of 10-15 µm (Legato, 1973). Similarly to Purkinje cells, they form fiber-like structures. Ventricular muscle fibers are organized in sheets and wrap around the ventricles along helical trajectories. While electrical signals are mainly propagated

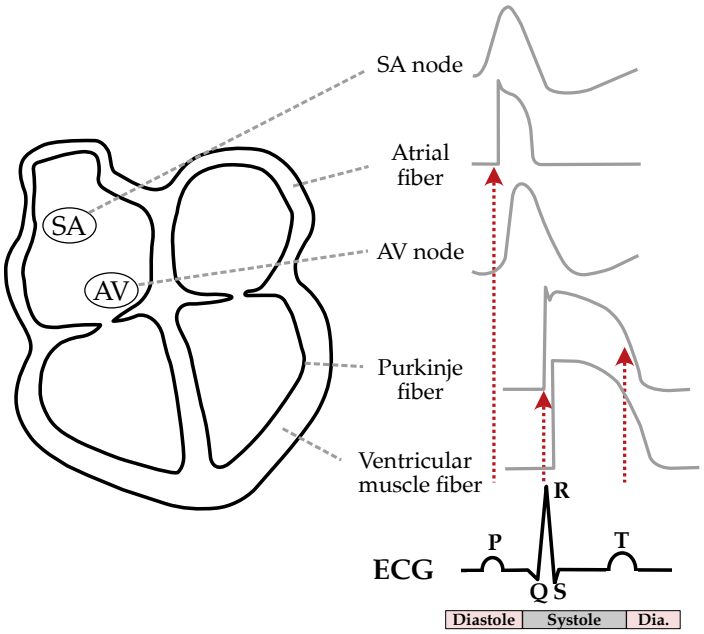

Figure 2.5: Action potentials of different cardiomyocytes contributing to the overall electrocardiography (ECG) signal. The figure is adapted from (Harvey and Grant, 2018).

along the cardiac fibers (Legato, 1973), neighboring fibers can also communicate and pass on electrical signals, e. g., by exchanging ions through the cell membranes and extracellular space (ephaptic coupling (Lin and Keener, 2010)). This coupling mechanism can result in complex depolarization waveforms that are propagated through the myocardium.

The electrical activity of the heart can be recorded with an electrocardiogram (ECG). The ECG plots the temporal evolution of the electrical voltage that is created by the de- and repolarization of the myocardium and measured with electrodes attached to the skin. Figure 2.5 shows how APs initiated in different parts of the cardiac conduction system and myocardium contribute to the ECG signal. Most importantly, the P-wave on the ECG signal indicates depolarization of the atria, while the QRS complex is caused by depolarization of the ventricles. Finally, the T-wave corresponds to repolarization of the ventricles. The phase between the end of the P-wave and the end of the T-wave is the ventricular *systole*, during which an electrical impulse is propagated through the myocardium, causing it to contract. The phase between the T-wave and the P-wave is the ventricular *diastole*, during which the myocardium is relaxed.

2.3.3 *The strength-duration curve*

The threshold for tissue stimulation is often quantified in terms of the *strength-duration* curve (Geddes and Bourland, 1985a,b; Mouchawar et al., 1989; Tacker and Geddes, 1996). This curve describes the dependence of the strength or amplitude of the investigated threshold quantity, e. g., the electrode current or the magnetically induced E-field amplitude, on the duration during which it is applied. Weiss found

The pulse duration denotes the duration during which a stimulus, such as an electrode current or E-field, is applied to the tissue.

that the lowest (threshold) charge Q of an electrode had a positive linear correlation with the pulse duration τ (Weiss, 1901):

$$Q(\tau) = b(\tau + c), \tag{2.67}$$

with tissue- and experiment-specific parameters b and c. For a rectangular pulse, the threshold electrode current amplitude I is given by the ratio of the charge and the pulse duration. For such pulses, the threshold current can thus be expressed as:

$$I(\tau) = I_{rheo}\left(1 + \frac{t_{chron}}{\tau}\right). \tag{2.68}$$

This equation is the empirically derived hyperbolic, so-called *Lapicque* expression of the strength-duration curve (Lapicque, 1909). This formulation is equivalent to Equation 2.67, with $b = I_{rheo}$ being the so-called *rheobase*, i. e., the threshold asymptote for long pulse durations. The parameter $c = t_{chron}$ is termed the *chronaxie*, which corresponds to the time at which the threshold current is twice the rheobase. The chronaxie of the mammalian myocardium was estimated to be around 2 ms (Geddes and Bourland, 1985a; Irnich, 1994).

Irnich expressed the hyperbolic strength-duration curve (Equation 2.67) in terms of the E-field magnitude E induced in the tissue:

$$\frac{1}{\tau}\int^{\tau} E\,dt \geqslant E_{rheo}\left(1 + \frac{t_{chron}}{\tau}\right). \tag{2.69}$$

Here, E_{rheo} is the rheobase of the electric field, and τ is the E-field pulse duration. Irnich referred to this formulation as the "Fundamental Law for Electrostimulation" (Irnich, 1994). The integral in Equation 2.69 implies that stimulation is determined by the time-average of the E-field amplitude, and that the pulse shape, i. e., the temporal evolution of the E-field, does not play a role.

Another approach to quantify tissue stimulation models the cell membrane as an RC-equivalent circuit and describes stimulation as the charging process of this circuit. This approach gives rise to the exponential *Blair* strength-duration curve (Blair, 1932):

$$I(\tau) = I_{rheo} \cdot \left(1 - \exp\left(-\frac{\tau}{t_c}\right)\right)^{-1} \tag{2.70}$$

In this equation, I_{rheo} is again the rheobase of the threshold electrode current, and $t_c = RC$ is the time constant of a cell membrane represented by a resistance R and capacitance C connected in parallel. For the canine myocardium, the average time constant was measured to be 2.4 ms (Pearce et al., 1982).

2.3.4 *Safety regulations for MRI gradient fields*

In MRI, E-fields induced by time-varying gradient fields can lead to unwanted magnetostimulation effects. MRI gradient fields need to be switched rapidly, i. e., between 100 Hz and 10 kHz (Bowtell and Bowley, 2000), to allow for fast image acquisition. The induced E-fields in the patient can become strong enough to interact with the peripheral nervous system and cause *peripheral nerve stimulation (PNS)*. At onset,

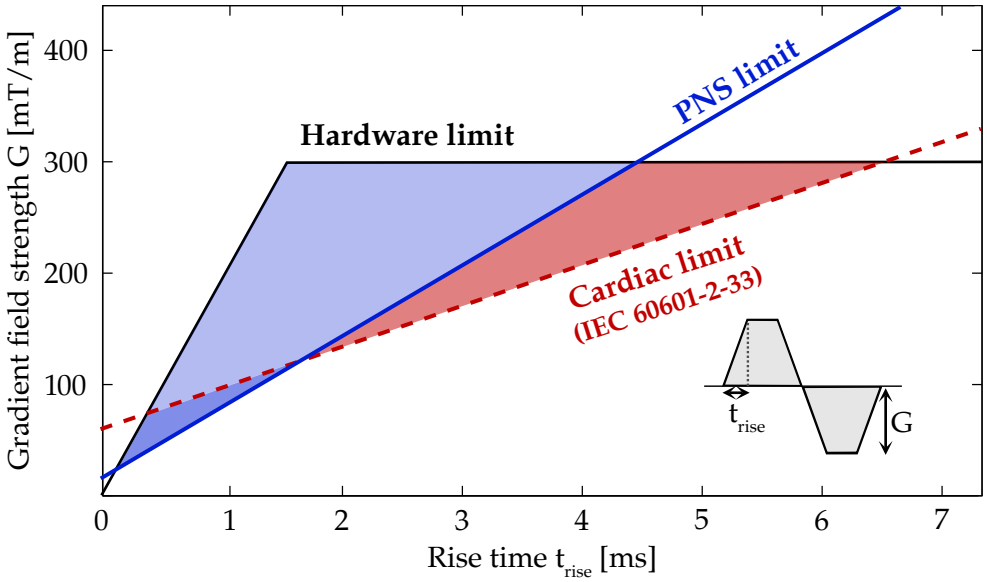

Figure 2.6: Hardware and stimulation limits of the Siemens Connectome scanner (Siemens Healthineers, Erlangen, Germany). The blue curve shows the gradient coil's PNS thresholds, which were measured in healthy volunteers for rise times between 0.1 ms and 0.8 ms for simultaneous slewing of the X-, Y-, and Z-axis coils, and extrapolated linearly for longer rise times (Setsompop et al., 2013). The red curve shows the cardiac safety limit for the Connectome gradient as defined by the IEC 60601-2-33 regulatory standard (IEC, 2010). The black curve shows the hardware limits, which are dictated by the maximum gradient field strength and the slew rate. The figure is adapted from (Setsompop et al., 2013).

PNS is usually experienced as a benign tingling or tapping sensation (Budinger et al., 1991; Schaefer et al., 2000), but can get intolerable and even painful if the PNS threshold is exceeded by more than 50% (Bourland et al., 1999; Budinger et al., 1991).

Safety regulations issued by the International Electrotechnical Commission (IEC) 60601-2-33 standard demand that "the occurrence of intolerable PNS in the patient and in the MR worker at any operating mode is minimized" (IEC, 2010). The PNS limit of new gradient coil prototypes is usually determined in an experimental study on healthy human volunteers (Feldman et al., 2009; Lee et al., 2016; Setsompop et al., 2013). The PNS limit of state-of-the-art gradient systems is often lower than the hardware limit, especially at short rise times that are relevant for fast imaging sequences such as EPI (Mansfield and Harvey, 1993; Mansfield and Maudsley, 1977). As a consequence, the technically achievable maximum gradient amplitude and slew rate can often not be used in human MRI because of PNS.

With the increasing hardware performance of recently developed gradient systems, stimulation of the heart by gradient-induced E-fields is becoming a growing safety concern (Irnich, 1994; Irnich and Schmitt, 1995; Nyenhuis et al., 1994; Reilly, 1991, 1992b; Schaefer et al., 2000). *Cardiac stimulation (CS)* can result in life-threatening arrhythmias such as ventricular fibrillation (VF) (Antoni, 1998; Reilly, 1992b), and thus poses a substantially more severe safety hazard than PNS. The IEC

60601-2-33 standard defines limits for the amplitude of the induced E-field and the magnetic field rate (dB/dt) to prevent CS by MRI gradient fields:

$$E < \frac{2\ \mathrm{V/m}}{1 - \exp\{-\frac{t_{s,\mathrm{eff}}}{3}\}} \tag{2.71}$$

$$\frac{dB}{dt} < \frac{20\ \mathrm{T/s}}{1 - \exp\{-\frac{t_{s,\mathrm{eff}}}{3}\}}. \tag{2.72}$$

Here, $t_{s,\mathrm{eff}}$ denotes the effective stimulus duration in ms, which is defined as the ratio of the peak-to-peak field variation and the maximum time derivative of the gradient field during that period (IEC, 2010). The IEC cardiac safety limit is based on the exponential strength-duration curve (Equation 2.70), with a rheobase of $dB/dt_{\mathrm{rheo}} = 20\ \mathrm{T/s}$ and $E_{\mathrm{rheo}} = 2\ \mathrm{V/m}$, respectively.

For some high-amplitude gradient systems, this limit can become lower and thus more restricting than the PNS limit at long gradient rise times. For the Siemens Connectome MRI scanner, for example, the cardiac limit is lower than the PNS limit for rise times $t_{\mathrm{rise}} > 1.5$ ms and gradient field amplitudes >100 mT/m (Setsompop et al., 2013), as shown in Figure 2.6. This example shows that CS can become a relevant limitation for gradient performance, and thus for MR imaging speed and resolution.

2.4 NUMERICAL MODELING OF MAGNETOSTIMULATION

This section provides an overview of how tissue magnetostimulation can be characterized and investigated through numerical models. The first part describes the approximation of EM fields in the magneto-quasistatic regime, which is valid at low frequencies such as those used in MRI gradient field applications. The contents of this part are explained in more detail in, e. g., (Rodríguez and Valli, 2010) and (Rodríguez, 2015). The second part introduces the Hodgkin-Huxley formalism, which forms the basis for most mathematical models that describe the excitability of biological tissues such as nerve and cardiac cells. A good overview of such models is provided by references (Keener and Sneyd, 2009) and (Izhikevich, 2007).

2.4.1 *Electromagnetic field approximation at low frequencies*

The generation and interplay of EM fields is described by Maxwell's equations (given here in the differential formulation):

$$\text{Gauss's law:} \qquad \vec{\nabla} \cdot \vec{E} = \frac{\rho}{\epsilon_0} \tag{2.73}$$

$$\text{Gauss's law for magnetism:} \qquad \vec{\nabla} \cdot \vec{B} = 0 \tag{2.74}$$

$$\text{Faraday's law of induction:} \qquad \vec{\nabla} \times \vec{E} = -\frac{\partial \vec{B}}{\partial t} \tag{2.75}$$

$$\text{Ampère's circuital law:} \qquad \vec{\nabla} \times \vec{B} = \mu_0 \left(\vec{J} + \epsilon_0 \frac{\partial \vec{E}}{\partial t} \right), \tag{2.76}$$

where $\vec{E}$ denotes the electric field density, ρ the electric charge density, $\vec{B}$ the magnetic flux density, and $\vec{J}$ the electric current density. ϵ_0 and μ_0 are the electric permittivity and the magnetic permeability of vacuum, respectively. Taking the divergence of Equation 2.76 in combination with Equation 2.73 yields the *charge continuity equation*

$$\frac{\partial \rho}{\partial t} + \vec{\nabla} \cdot \vec{J} = 0, \tag{2.77}$$

which states that the local charge density can only change if there is a change of current flow. The derivation of Equation 2.77 made use of the fact that the divergence of the curl of a vector field is zero: $\vec{\nabla} \cdot \vec{\nabla} \times \vec{B} = 0$.

The above equations describe the interdependence of magnetic and electric fields in free space or at a microscopic scale. In a dielectric medium, an electric field $\vec{E}$ causes a separation of the bound charges, i. e., nucleons and electrons, which form a local electric dipole moment. This effect is described by the displacement field

$$\vec{D} \equiv \epsilon_0 \vec{E} + \vec{P}, \tag{2.78}$$

where $\vec{P}$ is the polarization field that describes the density of magnetic dipole moments in the medium. Similarly, a magnetic flux density $\vec{B}$ magnetizes the bound microscopic constituents of a medium, causing a macroscopic magnetic magnetization $\vec{M}$. The total magnetic field $\vec{H}$ can thus be defined as

$$\vec{H} \equiv \frac{\vec{B}}{\mu_0} - \vec{M}. \tag{2.79}$$

In matter, Ampère's law becomes

$$\vec{\nabla} \times \vec{H} = \vec{J} + \frac{\partial \vec{D}}{\partial t} \tag{2.80}$$

with the divergence

$$\vec{\nabla} \cdot \vec{\nabla} \times \vec{H} = 0 = \vec{\nabla} \cdot \vec{J} + \frac{\partial}{\partial t} \vec{\nabla} \cdot \vec{D}. \tag{2.81}$$

Inserting Equation 2.77 yields

$$\frac{\partial \rho}{\partial t} = \frac{\partial}{\partial t} \vec{\nabla} \cdot \vec{D}, \tag{2.82}$$

which is the temporal derivative of Gauss's law in matter. Similarly, taking the divergence of Faraday's law yields the temporal derivative of Gauss's law for magnetism:

$$\vec{\nabla} \cdot \vec{\nabla} \times \vec{E} = 0 = -\frac{\partial}{\partial t} \vec{\nabla} \cdot \vec{B}. \tag{2.83}$$

Thus, as long as the initial conditions $\vec{\nabla} \cdot \vec{D} = \rho$ and $\vec{\nabla} \cdot \vec{B} = 0$ are fulfilled, the temporal evolution of the electric and the magnetic field is completely specified by

$$\frac{\partial \vec{D}}{\partial t} = \vec{\nabla} \times \vec{H} - \vec{J} \tag{2.84}$$

$$\frac{\partial \vec{B}}{\partial t} = -\vec{\nabla} \times \vec{E}. \tag{2.85}$$

In linear media, the relationships

$$\vec{D} = \epsilon\vec{E} = \epsilon_0\epsilon_r\vec{E} \tag{2.86}$$

$$\vec{B} = \mu\vec{H} = \mu_0\mu_r\vec{H} \tag{2.87}$$

hold, with the relative permittivity ϵ_r and relative permeability μ_r. In the case of homogeneous isotropic media, ϵ and μ are scalars. Using these relationships, Equation 2.84 and Equation 2.85 can be combined to yield a single second-order differential equation in time:

$$\vec{\nabla} \times \frac{1}{\mu}\vec{\nabla} \times \vec{E} + \epsilon\frac{\partial^2\vec{E}}{\partial t^2} = -\frac{\partial\vec{J}}{\partial t}. \tag{2.88}$$

In the harmonic or time-periodic regime $\left[\vec{X}(\vec{r},t) = \Re\left(e^{i\omega t}\vec{X}(\vec{r})\right)\right]$, it is assumed that the applied source current $\vec{J}$, and thus also the electric field $\vec{E}$, vary periodically in time: $\vec{J} \propto \sin(\omega t)$, with ω denoting the angular frequency of the system. $\vec{X}(\vec{r})$ is the complex-valued amplitude ("phasor" (Rodríguez and Valli, 2010; Rodríguez, 2015)) of the magnetic or electric field. In the harmonic regime, the temporal derivative $\partial/\partial t$ simply becomes $i\omega$, and Equation 2.88 can be expressed as

$$\vec{\nabla} \times \frac{1}{\mu}\vec{\nabla} \times \vec{E} - \epsilon\omega^2\vec{E} = -i\omega\vec{J}. \tag{2.89}$$

MRI gradient fields generally operate at frequencies $\omega/2\pi$ below 10 kHz (Bowtell and Bowley, 2000). The corresponding wavelengths are on the order of thousands of meters and thus much larger than the patient.

MRI gradient fields operate in the low-frequency (LF) regime, in which the EM field wavelength is much larger than the diameter of the physical domain. In this regime, ohmic currents dominate displacement currents (Bowtell and Bowley, 2000), which can be included in Maxwell's equations by setting ϵ to zero. This results in

$$\vec{\nabla} \times \frac{1}{\mu}\vec{\nabla} \times \vec{E} = -i\omega\left(\vec{J}_s + \sigma\vec{E}\right). \tag{2.90}$$

Here, the electric current density is divided into an imposed (or "source") part and an ohmic part:

$$\vec{J} = \vec{J}_s + \vec{J}_{ohm} = \vec{J}_s + \sigma\vec{E}, \tag{2.91}$$

where σ is the electric conductivity of the medium (Rodríguez and Valli, 2010; Rodríguez, 2015). The source current density $\vec{J}_s$ can, e. g., be described by a current-carrying coil wire path.

Equation 2.90 can be solved by introducing a magnetic vector potential $\vec{A}(\vec{r},t)$ that satisfies

$$\vec{B} = \vec{\nabla} \times \vec{A}, \tag{2.92}$$

and that is divergence free ($\nabla \cdot \vec{A} = 0$). The electric field is given in terms of the vector potential $\vec{A}$ and the scalar electric potential Φ as

$$\vec{E} = -\vec{\nabla}\cdot\Phi - \frac{\partial\vec{A}}{\partial t} = -\vec{\nabla}\cdot\Phi - i\omega\vec{A}. \tag{2.93}$$

Substituting this expression for the electric fields in Equation 2.90 yields

$$\vec{\nabla} \times \frac{1}{\mu}\vec{\nabla} \times \vec{A} + \sigma\left(\vec{\nabla}\cdot\Phi + i\omega\vec{A}\right) = \vec{J}_s. \tag{2.94}$$

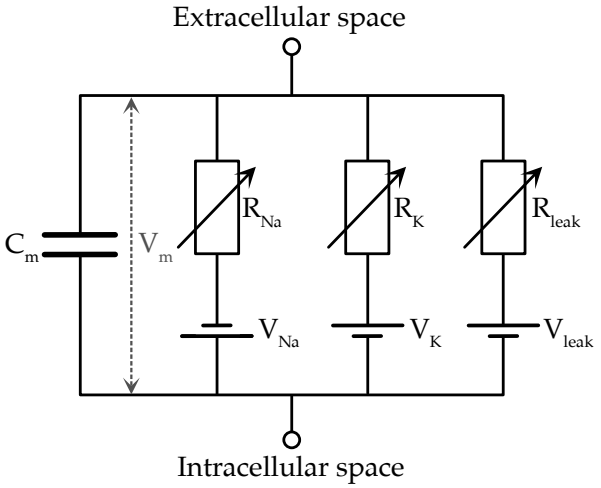

Figure 2.7: Electrical-circuit model representing the electrical properties of a nerve membrane. The figure is adapted from (Hodgkin and Huxley, 1952).

From Maxwell's equations, it follows that the current density (i. e., both the source and the ohmic current density) is divergence free if $\epsilon = 0$:

$$\vec{\nabla} \cdot \vec{J}_s = 0, \tag{2.95}$$

and thus

$$\vec{\nabla} \cdot \sigma \left(\vec{\nabla} \cdot \Phi + i\omega \vec{A} \right) = 0. \tag{2.96}$$

This approximation of Maxwell's equations in the low-frequency regime is referred to as the *eddy current* or *magneto-quasistatic approximation* (Rodríguez and Valli, 2010; Rodríguez, 2015).

2.4.2 *The Hodgkin-Huxley formalism*

The (passive) conduction of electrical current along nerve fibers can be described using the classical *cable theory*, which was originally developed by William Thomson (also known as Lord Kelvin) in the the 1850s to describe signal conduction along transatlantic telegraphy cables. This theory models cables as patches consisting of a capacitance and resistance connected in parallel. Sir Alan L. Hodgkin and Sir Andrew F. Huxley were among the first to apply cable theory to nerve cell behavior. In 1952, they published experiments conducted on the giant squid nerve fiber, and developed a numerical model of the excitability of the nerve fiber membrane (Hodgkin and Huxley, 1952). Together with Sir John F. Eccles they were awarded the Nobel Prize in Physiology or Medicine in 1963 "for their discoveries concerning the ionic mechanisms involved in excitation and inhibition in the peripheral and central portions of the nerve cell membrane".

Figure 2.7 shows the basic electrical circuit model representing the nerve membrane. The capacitance C_m represents the lipid bilayer of the nerve membrane. The resistance of ion i

$$R_i = \frac{1}{g_i} \tag{2.97}$$

represents the voltage-gated sodium Na^+ and potassium K^+ channel, as well as a voltage-independent ion channel for the leakage current. g_i is the conductance of the respective ion channel. It is a measure of the permeability of the nerve membrane for each ion. A TMV V builds up either through charging of the membrane capacitance or through movement of ions through the ion channels. The ionic currents are given by the difference between the TMV V and the equilibrium ionic voltage V_i:

The leakage current is made up by chloride and other ions (Hodgkin and Huxley, 1952)

$$I_{Na} = g_{Na}(V - V_{Na}) \tag{2.98}$$
$$I_K = g_K(V - V_K) \tag{2.99}$$
$$I_l = g_l(V - V_l). \tag{2.100}$$

The equilibrium voltage V_i of ion i is given by the Nernst equation (Izhikevich, 2007):

$$V_i = \frac{RT}{zF} \ln\left(\frac{[\text{Ion}]_{out}}{[\text{Ion}]_{in}}\right), \tag{2.101}$$

with the universal gas constant $R = 8.315\ \text{mJ/K} \cdot \text{Mol}$, the temperature T in Kelvin, Faraday's constant $F = 96.480\ \text{C/Mol}$, and the valence z of the electron. $[\text{Ion}]_{out}$ and $[\text{Ion}]_{in}$ are the extra- and intracellular ion concentrations. At the equilibrium voltage, the ionic concentration gradient and the electric potential gradient across the nerve membrane cancel each other out, thus there is no net ionic current flow.

$z = 1$ for Na^+ and K^+, $z = -1$ for Cl^-.

In the Hodgkin-Huxley formalism (Hodgkin and Huxley, 1952), the temporal change of V is given by:

$$\frac{dV}{dt} = \frac{1}{C_m}(I - I_{ion}) \tag{2.102}$$

with the applied current I (e. g., a current injected via an electrode), and the total ionic current

$$I_{ion} = I_{Na} + I_K + I_{leak} \tag{2.103}$$
$$= \bar{g}_{Na} m^3 h\,(V - V_{Na}) \tag{2.104}$$
$$+ \bar{g}_K n^4\,(V - V_K) \tag{2.105}$$
$$+ g_{leak}\,(V - V_{leak}), \tag{2.106}$$

where $\bar{g}_i$ denotes the maximum conductance of ion i. The temporal dynamics of the ionic currents are governed by the voltage-dependent gating variables m and n (activation variables for Na^+ and K^+), and h (inactivation variable for Na^+). The gating variables, in the following summarized under the generalized designation y, can in turn be determined from the following first-order differential equations:

$$\frac{dy}{dt} = (y_\infty(V) - y)/\tau_y(V) \tag{2.107}$$

with

$$y_\infty = \alpha_y/(\alpha_y + \beta_y) \tag{2.108}$$

and

$$\tau_y = 1/(\alpha_y + \beta_y), \tag{2.109}$$

where α_y and β_y are exponential functions of the TMV V, whose parameters have to be determined from experiments. Figure 2.8 shows the kinetics of the TMV and

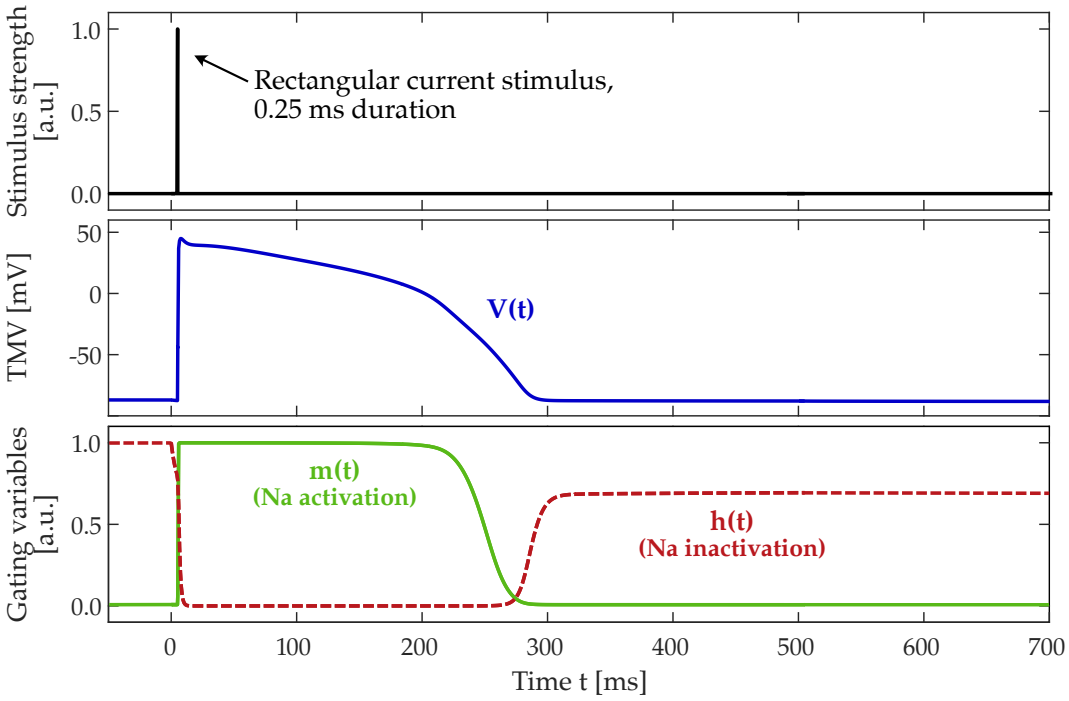

Figure 2.8: Transmembrane voltage (TMV, middle row) and two of the gating variables (bottom row) of the membrane model of a human ventricular cardiomyocyte (O'Hara et al., 2011). The model was excited by a 0.25-ms rectangular current stimulus (top row).

the gating variables of a cardiac cell membrane model using the Hodgkin-Huxley formalism. In this example, the cell membrane is stimulated with a rectangular current stimulus applied with supra-threshold amplitude. This stimulus causes an AP that is characterized by a transient spike in the TMV (see Section 2.3.2).

The Hodgkin-Huxley equations of the form of Equation 2.102 only describe the temporal dynamics of the TMV at a single point of the cell membrane and do not include spatial effects such as currents flowing along the nerve axon or cardiac fiber. Cable theory can be used to express the transmembrane current I in terms of voltage:

$$I = G_a \frac{\partial^2 V}{\partial x^2}, \tag{2.110}$$

where x is the position along the axon, and G_a is the axial conductance of the axoplasm. Substituting Equation 2.110 into Equation 2.102 yields

$$\frac{\partial V(t,x)}{\partial t} = \frac{1}{C_m}\left(G_a \frac{\partial^2 V(t,x)}{\partial x^2} - I_{ion}\right). \tag{2.111}$$

This formulation is commonly referred to as the *Hodgkin-Huxley cable equation* (Izhikevich, 2007) and allows modeling of both the initiation and conductance of action potentials along excitable nerve and cardiac fibers (Rudy and Quan, 1987, 1991; Sharp and Joyner, 1980). The effect of an extracellular voltage V_{ext} applied along the fiber

can be modelled by simply adding the second spatial derivative of V_{ext} to Equation 2.111:

$$\frac{\partial V(t,x)}{\partial t} = \frac{1}{C_m}\left(G_a\left(\frac{\partial^2 V(t,x)}{\partial x^2} + \frac{\partial^2 V_{ext}(t,x)}{\partial x^2}\right) - I_{ion}\right). \tag{2.112}$$

The Hodgkin-Huxley equations form the basis for most neurodynamic models that were developed in the past decades. These models describe the dynamics of myelinated (McIntyre et al., 2002) and unmyelinated (Pelot et al., 2021) peripheral nerve fibers with increasing complexity. Early nerve models assumed the axon to be perfectly electrically isolated from the extracellular space except at the nodes of Ranvier (McNeal, 1976; Reilly, 1985). This assumption ignores the finite impedance of the myelin sheath. More sophisticated models, such as the double-cable *McIntyre-Richardson-Grill (MRG)* model (McIntyre et al., 2002), represent the mammalian nerve membrane with a higher level of detail. The MRG model explicitly represents the nodes of Ranvier, a variety of para- and internodal compartments, and the finite-impedance myelin sheath for axons with discrete radii. As discussed in Section 2.3.2, cardiomyocytes have a larger variety of ion channels that play a role in the initiation of APs in comparison to peripheral nerve fibers. However, the basic mechanisms underlying the generation of APs is similar for both cell types, thus most electrophysiology models of different cardiomyocyte types are also based on the Hodgkin-Huxley formalism. A comprehensive overview of these models is provided in (Amuzescu et al., 2021).

3 MATERIALS AND METHODS

This chapter is divided into three sections. The first section describes the modeling framework developed in this work to predict cardiac stimulation (CS) by time-varying magnetic fields in computational anatomical models and explains the preliminary validation of the modeling pipeline through a comparison with previous canine experiments. The second section covers the materials and methods employed for the experimental study that measured cardiac magnetostimulation thresholds in in vivo in healthy pigs. Finally, the third section describes the prediction of CS thresholds in porcine models of the specific animals used in the experiments. Parts of this chapter have been published in (Klein et al., 2021) by John Wiley & Sons[1] and submitted as (Klein et al., 2022). The description of the corresponding materials and methods is partly replicated here.

3.1 MODELING FRAMEWORK FOR THE PREDICTION OF CARDIAC STIMULATION

In this work, a modeling framework was developed that allows prediction of the threshold at which the heart is stimulated by E-fields induced by time-varying magnetic fields. The basic steps of this modeling pipeline were based on the recently developed simulation framework for peripheral nerve stimulation (PNS), which was validated against experimental data for several whole-body and head gradient systems (Davids et al., 2019a,b) as well as an MPI drive coil (Davids et al., 2017). In short, the modeling workflow is as follows (Figure 3.1): First, the EM fields generated by a given coil wire geometry are simulated in computational models of a human male and female adult. Second, the electric field (E-field) is projected onto paths of electrically excitable fibers in the heart, in particular the cardiac Purkinje and ventricular muscle fibers. The projected E-field is integrated along the fiber paths, yielding electric potential differences, and modulated in time with the coil current waveform. In the final step, the resulting spatio-temporal electric potential is fed into electrical-circuit models of Purkinje and ventricular muscle fibers. The following paragraphs will explain each of these steps in more detail.

Except for the EM field simulations, all computational methods were implemented in Matlab (The MathWorks, Natick, MA, USA).

3.1.1 *Computational human body models*

Figure 3.2 shows the male and female human body models used for the EM field simulations. The models were derived from the commercially available anatomical surface data of a male (weight 82 kg, height 176 cm) and female adult (weight 53 kg, height 163 cm) provided by Zygote (American Fork, UT, USA). As described in references (Davids et al., 2017) and (Davids et al., 2018), the Zygote surfaces were processed to make them suitable for finite-element EM simulations. To this end, a re-

1 © 2020 The Authors. Magnetic Resonance in Medicine published by Wiley Periodicals LLC on behalf of the International Society for Magnetic Resonance in Medicine.

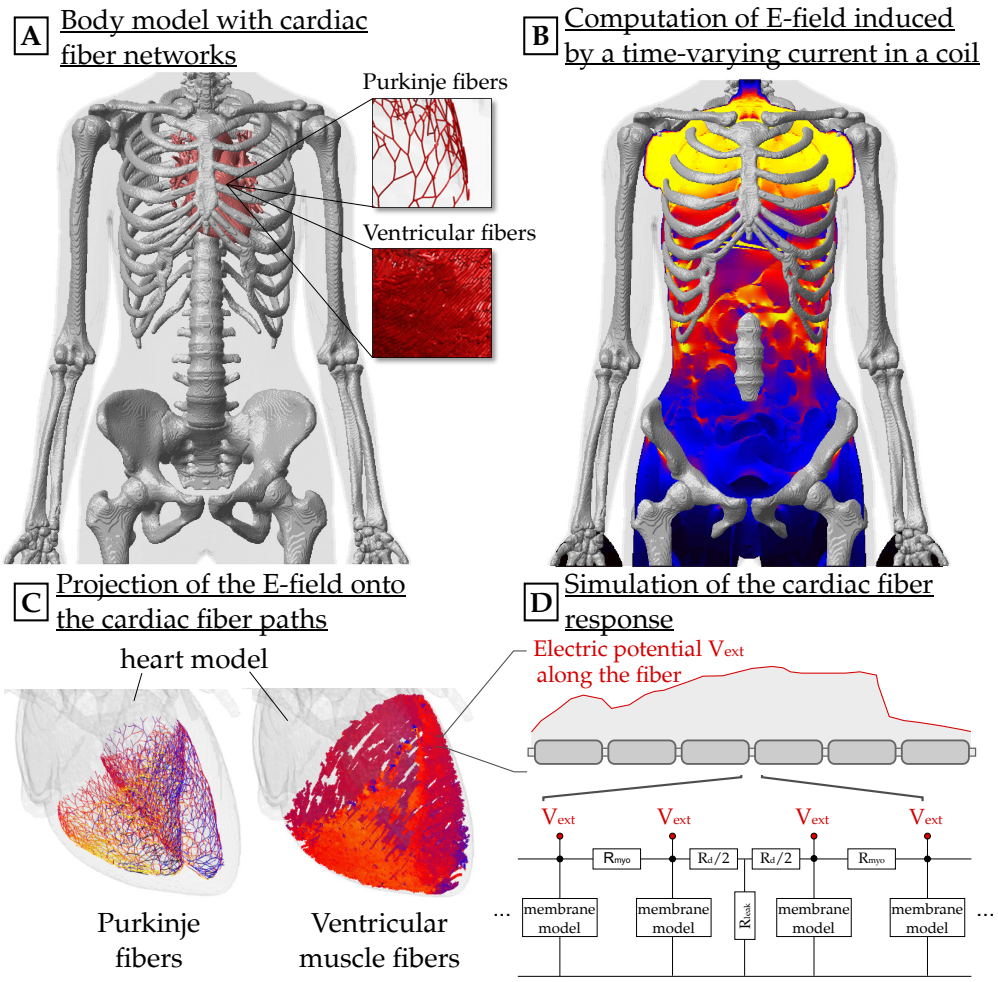

Figure 3.1: Overview of the modeling pipeline for the prediction of cardiac stimulation. (A) Detailed body model (shown here: bones, skin, and heart of the female human model) with added realistic networks of cardiac Purkinje and ventricular muscle fibers. (B) Coronal slices of the simulated electric field (E-field) induced by a time-varying current in a coil. (C) The E-field is projected onto the cardiac fiber paths. (D) The cardiac response to the extracellular electric potential is predicted using electrical-circuit models of Purkinje and ventricular muscle fibers. The figure is adopted from (Klein et al., 2021).

A fiber diameter of 20 µm was chosen for motor nerve fibers, 12 µm for sensory nerve fibers, and 2 µm for autonomic nerve fibers.

meshing strategy was used to ensure that the surface mesh description of the organs is topologically correct, i. e., two-manifold, watertight, and without intersections. The resulting models contain hundreds of surfaces that were classified into 25 tissue types as well as a detailed atlas of the largest peripheral nerves in the body. The nerve atlas contains approximately 1900 nerve tracks and is geometrically registered with the other tissues and organs. Each nerve segment was manually labeled by nerve type (motor, sensory, or autonomic) and fiber diameter based on physiological data of the human peripheral nervous system (Davids et al., 2017). The nerve fiber diameter determines the properties of the neurodynamic MRG model (McIntyre et al., 2002) that was used for the PNS predictions in this work. A more detailed description of the PNS prediction model can be found in references (Davids et al.,

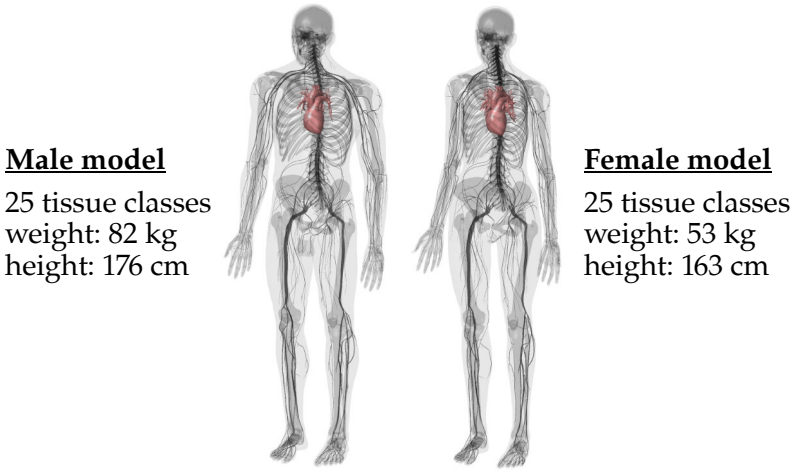

Figure 3.2: Male and female adult body models (Zygote, American Fork, UT, USA). For clarity, only the heart, peripheral nerve, bone, and skin surfaces are shown.

2019a, 2017; Klein et al., 2019). In the last step, the body models were voxelized with a resolution of 1 mm^3 to be compatible with the hexahedral solver used for the EM field simulations, as described in Section 3.1.3.

3.1.2 *Rule-based modeling of cardiac fiber paths*

The Zygote body models contain a detailed geometrical description of the gross heart anatomy, including in particular the atria and ventricles, large papillary muscles, the heart valves, and the large blood vessels that supply the heart. However, the body models do not contain a microscopic description of the cardiac conduction system and the myocardial fibers involved in cardiac excitation. Paths of cardiac Purkinje and ventricular muscle fibers were thus added to the body models using rule-based fiber generation algorithms.

Model of the subendocardial Purkinje fiber network

In humans and canines, the cardiac Purkinje fibers form a dense network beneath the endocardium (Ono et al., 2009). In this work, the subendocardial network was modeled with the rule-based algorithm developed by Ijiri et al., which is based on histological data of cardiac Purkinje fibers in sheep (Ijiri et al., 2008). The algorithm starts with a single fiber segment, which is iteratively grown in a tree-like fashion into "children" segments, the length of which is random and drawn from a Gaussian distribution. In this work, a mean fiber length of 3.0 mm was used, with a 0.2-mm standard deviation. Each parent segment divides into two children segments. The angle between these children segments is random following a Gaussian distribution. In this work, a mean angle between segments of 60° and a standard deviation of 6° was chosen. Realistic Purkinje fibers are not straight, which is modeled by dividing each fiber segment into sub-segments, whose relative orientation controls the curvature of the overall segment. The order in which the parent segments are grown into children is randomized in order to avoid systematic bias in the network topol-

The endocardium denotes the innermost tissue layer lining the heart chambers.

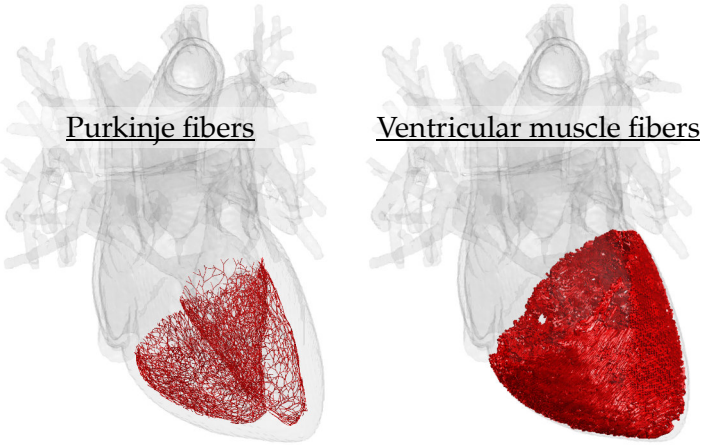

Figure 3.3: Purkinje and ventricular muscle fibers generated on the three-dimensional heart mesh of the female adult body model using rule-based modeling algorithms (Bayer et al., 2012; Ijiri et al., 2008). The figure is taken from (Klein et al., 2021).

ogy. The iterative fiber growth stops when segments collide or when the distance between a segment and the endocardial surface becomes larger than ca. 1.5 mm. The left-hand side of Figure 3.3 shows a Purkinje fiber network generated using this algorithm in the ventricles of the female human body model.

Model of ventricular muscle fibers

Paths of cardiac muscle fibers are commonly modeled using the Laplace-Dirichlet Rule-Based (LDRB) method (Piersanti et al., 2021). This method solves the Laplace equation on a three-dimensional mesh representation of the myocardium to parameterize and assign basic directions in the heart, such as the apico-basal and transmural directions. Fiber directions are then assigned with a set of mathematical rules determined from histological or MR Diffusion Tensor Imaging data (Piersanti et al., 2021).

In this work, the LDRB algorithm proposed by Bayer et al. was used to model ventricular muscle fiber paths (Bayer et al., 2012). This algorithm uses a tetrahedral mesh of the myocardium on which vector fields are defined for the apico-basal and transmural directions based on solutions of the Laplace equation with Dirichlet-Neumann boundary conditions. The "potential energy" function $\Theta(\vec{x})$ (Bayer et al., 2012) in each mesh node is found by solving

The apico-basal vector points from the apex, i. e., the tip of the heart, to the base of the heart. The transmural vector points from the endocardium to the epicardium, i. e., from the inner to the outer surface of the myocardium.

$$\vec{\nabla}^2\Theta(\vec{x}) = 0 \text{ in } \Omega, \tag{3.1}$$

where Ω is the computational domain, i. e., the tetrahedral myocardial mesh. The boundary conditions used in the Bayer LDRB algorithm are as follows:

$$\Theta = 1 \text{ on } \Gamma_1 \tag{3.2}$$

$$\Theta = 0 \text{ on } \Gamma_2 \tag{3.3}$$

$$\vec{\nabla}\Theta \cdot \vec{n} = 0 \text{ on } \partial\Omega - \Gamma_1 - \Gamma_2. \tag{3.4}$$

In case of the transmural potential energy function, Γ_1 is the epicardium and Γ_2 the endocardium (Bayer et al., 2012). The apico-basal and transmural directions are

found by taking the gradient of the Laplace solution $\vec{\nabla}\Theta$ of the respective potential energy function $\Theta(\vec{x})$. A coordinate system is then constructed with the unit vector $\hat{e_0}$, which is oriented circumferentially around the ventricles, and the apico-basal and transmural vectors $\hat{e_1}$ and $\hat{e_2}$. Using this coordinate system, longitudinal and transverse fiber directions are assigned to each mesh node at specific angles with respect to $\hat{e_0}$. In the ventricular walls, for example, the angle α between the fiber direction and $\hat{e_0}$ is given by

$$\alpha(d) = \alpha_{endo}(1-d) + \alpha_{epi} \cdot d. \tag{3.5}$$

Here, d denotes the normalized transmural depth, i. e., the distance between endo- and epicardium. $\alpha_{endo} = 40°$ is the fiber angle on the endocardium, and $\alpha_{epi} = -50°$ is the fiber angle on the epicardium (Bayer et al., 2012). Finally, streamlines are computed from the fiber orientation data, representing the fiber paths. The right-hand side of Figure 3.3 shows the resulting fiber paths that were generated in the ventricles of the female body model.

3.1.3 *Electromagnetic field simulations*

The EM fields induced in the body models by a given wire path of an external coil were calculated using the hexahedral finite-element method (FEM) magneto quasi-static solver of Sim4Life (Zurich MedTech, Zurich, Switzerland) at 1 mm^3 spatial resolution for a $I_0 = 1$ A, $f_0 = 1$ kHz sinusoidal coil current. The E-field amplitude induced by an arbitrary coil current waveform and target gradient field amplitude G_{target} in the region-of-interest was calculated from the simulated E-field amplitude $E_{sim}(1\,A, 1\,kHz)$ using the following formula:

$$E = \frac{E_{sim}(1\,A, 1\,kHz)}{2\pi f_0 I_0} \frac{G_{target}}{\epsilon_G} \frac{dW(t)}{dt}, \tag{3.6}$$

where ϵ_G is the gradient field efficiency of the coil in mT/m/A, and $W(t)$ is the unit-less waveform profile scaled between -1 and $+1$. Alternatively, the E-field can be scaled based on the target magnetic field amplitude B_{target}, in which case ϵ_G is replaced by the coil's B-field efficiency ϵ_B. This simple linear scaling of the E-field is valid in the quasi-static (low-frequency) regime and is thus applicable to standard gradient waveforms, which normally operate at frequencies below ca. 10 kHz (Bowtell and Bowley, 2000) (see Section 2.4.1).

The gradient efficiency is the gradient field amplitude created by the coil in the FOV at 1 A current.

The simulation of E-fields requires knowledge of the spatial distribution of electrical conductivity values $\sigma(\vec{x})$. These values were assigned to the different tissue classes in the body models based on the IT'IS (Zurich, Switzerland) low-frequency material database (Hasgall et al., 2018). This database provides conductivity values as a combination of the dispersion relations detailed by Gabriel et. al. (Gabriel et al., 1996a,b) and experimental conductivity values averaged across different studies conducted at frequencies below 1 MHz (Hasgall et al., 2018). The permittivity values in the database are the same as in (Gabriel et al., 1996a,b).

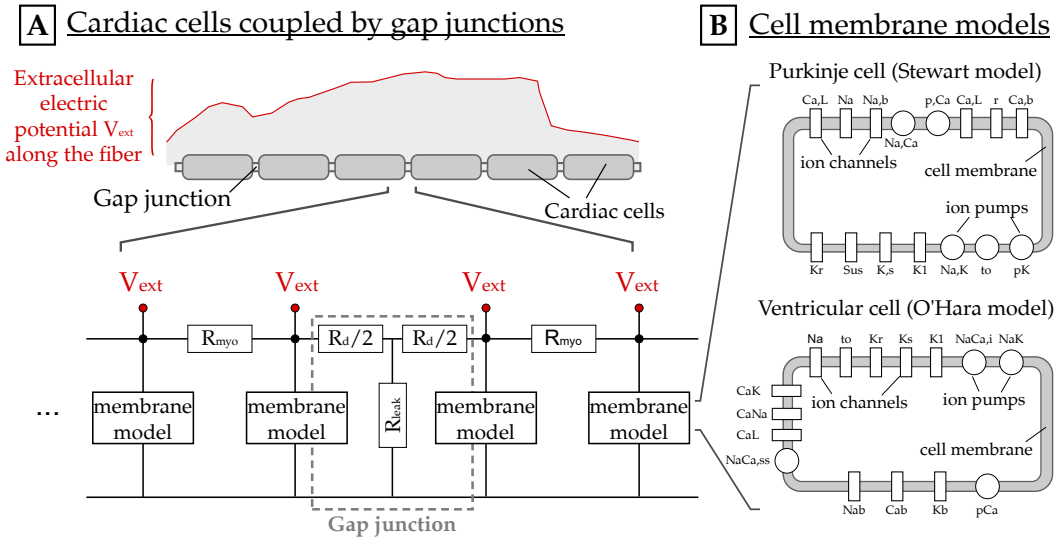

Figure 3.4: Electrical-circuit model of a cardiac fiber. Adjacent cells are connected by gap junctions, which are represented by a resistive T-network. The ion dynamics of the Purkinje cell membrane are represented by the Stewart model (Stewart et al., 2009), and by the O'Hara model for ventricular myocytes (O'Hara et al., 2011), respectively. The figure is taken from (Klein et al., 2021).

3.1.4 *Electrophysiological models of cardiac fibers*

In the next step, the E-field was projected onto the Purkinje and ventricular muscle fiber trajectories and integrated along those paths, to determine the electric potential along the fiber paths. The E-field, and hence also the potential, was modulated in time by the coil current waveform $W(t)$ (Equation 3.6). The electric potential, which thus depends both on space and time, was fed into electrophysiological models of the cardiac fibers that are described in more detail in the following.

The modeled Purkinje and ventricular muscle fiber paths were divided into approximately 3000 and 7000 fiber "segments", respectively. A segment describes a part of a fiber that contains no bifurcations and can be processed independently from the rest of the fiber network. Each segment contained between five and ca. 1000 Purkinje cells or ventricular myocytes. Each cell was modeled as a cylinder with a length of 100 µm, and the electrophysiological properties of the cardiac fiber segments were modeled using the one-dimensional discrete cable model proposed by Rudy and Quan (Rudy and Quan, 1987, 1991). In this model, the cardiac cells are connected longitudinally by gap junctions that are 80 Å in length and are modeled as a resistive T-network (Rudy and Quan, 1991) (Figure 3.4). The T-network consists of an effective axial resistance R_d and a leakage resistance R_{leak} to extracellular space. The respective parameter values used in the simulations are given in Table 3.1. The choice of a purely resistive representation of the gap junction is based on the assumption that the interaction between cells is passive (Rudy and Quan, 1987, 1991). In contrast, the charge flow across the cell membrane between the intra- and extracellular space is considered to be an active process, as the membrane contains active elements such as ion pumps.

Table 3.1: Definitions and values of parameters used in the electrophysiological simulations. Unless specified otherwise, the same parameter values were used for the Purkinje fiber (PF) and the ventricular fiber (VF) models. The remaining model parameters of the Purkinje cell and the ventricular myocyte membrane models can be found in the respective publications (O'Hara et al., 2011; Stewart et al., 2009).

Parameter	Value and reference
Cell length l	100 µm (Rudy and Quan, 1987, 1991)
Fiber diameter d (PF)	80 µm (Legato, 1973)
Fiber diameter d (VF)	15 µm (Legato, 1973)
Spec. mem. capacitance c_m (PF)	2 $\mu F/cm^2$ (Stewart et al., 2009; Tusscher et al., 2004)
Spec. mem. capacitance c_m (VF)	1 $\mu F/cm^2$ (O'Hara et al., 2011; Rudy and Quan, 1991)
Axial gap junction resistance R_d	1 Ωcm^2 (Rudy and Quan, 1991)
Leakage resistance R_{leak}	10^{10} kΩ (Rudy and Quan, 1991)
Intracellular resistivity ρ_{int}	162 Ωcm (Stewart et al., 2009; Tusscher et al., 2004)
Spatial resolution Δx	$\leqslant$ 50 µm
Temporal resolution Δt	$\leqslant$ 1 µs

The membrane of individual cells in the fiber models was modeled using the experimentally validated electrical-circuit Stewart model for Purkinje cells (Stewart et al., 2009), and the O'Hara model for ventricular cardiomyocytes (O'Hara et al., 2011). Both models are implemented in the CellML model repository (Lloyd et al., 2008). The models are based on the Hodgkin-Huxley formalism (see Section 2.4.2), and include a large number of ionic currents that play a role in the cardiac AP generation, such as different sodium, potassium, and calcium currents Figure 3.4. The O'Hara model, e.g., has 41 state variables (O'Hara et al., 2011). For comparison, the original Hodgkin-Huxley model of the squid axon has only four state variables (Hodgkin and Huxley, 1952).

Mathematically, the Purkinje and ventricular fiber models are represented by a set of coupled differential equations that describe the ionic current flow dynamics (calcium, sodium, and potassium) across the cell membrane, as well as axial signal propagation through the cells and gap junctions. Most importantly, the fiber models can predict the creation of APs, i. e., the rapid upstroke of the membrane potential $V(x,t)$ that indicates electrical excitation of the fiber. Each cell was divided into two or more sections for which the TMV was computed by solving the Hodgkin-Huxley cable equation (Equation 2.111) with a spatial resolution of $\Delta x \leqslant 50$ µm. The axial conductance of the fibers was calculated according to

$$G_a = (\pi a^2)/(\rho_{int}\Delta x), \tag{3.7}$$

with the intracellular resistivity ρ_{int} and the respective fiber radius $a = d/2$ (Table 3.1). The largest physiological diameters of human cardiac fibers were assigned to the models, i. e., 80 µm for Purkinje fibers, and 15 µm for ventricular muscle fibers (Legato, 1973). This represents a conservative assessment of the stimulation threshold, as larger fibers are generally more excitable (Davids et al., 2017; Enoka, 2002).

The membrane capacitance C_m was calculated from the specific membrane capacitance c_m, which is the capacitance per cell membrane area, and the area A_m of one section of cell membrane according to:

$$C_m = A_m \cdot c_m = 2\pi a \Delta x \cdot c_m. \tag{3.8}$$

Physiological values for the specific membrane capacitance were chosen based on the published cell membrane models for Purkinje cells (Stewart et al., 2009; Tusscher et al., 2004) and ventricular myocytes (O'Hara et al., 2011; Rudy and Quan, 1991), as listed in Table 3.1. Note that simulations in a previous publication (Klein et al., 2021) used larger membrane capacitance values. The temporal resolution with which the models were solved was chosen such that at least 100 time points per E-field (or, equivalently, dB/dt) pulse duration were used. This number of time points has previously been found to produce accurate results in PNS simulations (Klein et al., 2019). The maximum time step used in this work was $\Delta t = 1$ µs to accurately capture the fast upstroke of the cardiac AP. The coupled differential equations were solved using the Rush-Larsen algorithm (Rush and Larsen, 1978) to increase computational speed.

The Stewart model reproduces the pacemaking activity (Stewart et al., 2009), which is the ability of Purkinje fibers to generate APs at a default rate (ca. 50 beats per minute), even in the absence of an external stimulus like an extracellular E-field (Figure 3.5a). This phenomenon is referred to as *autorhythmicity* (Antoni, 1998), and is not present in the ventricular myocardium. So-called "pacemaking currents" cause a linear increase of the TMV of the Purkinje fiber model until a pacemaking AP is initiated spontaneously (Stewart et al., 2009). The fiber is most sensitive to stimulation right before the start of a pacemaking AP, when the highest resting potential is reached. In this work, external stimuli were applied ca. 200 µs before the next pacemaking AP in the Purkinje fiber model to target the most sensitive phase of the fiber model and thus find the lowest stimulation threshold that leads to an ectopic AP (Figure 3.5b).

Successful stimulation by an external stimulus was defined as an AP created in either the ventricular muscle or Purkinje fiber model. An AP in a single fiber can lead to excitation of the entire myocardium (Tacker and Geddes, 1996), and can therefore be taken as a conservative indicator for cardiac stimulation. For the Purkinje fibers, such an ectopic AP had to occur within ca. 180 µs after the application of the stimulus to make sure that the AP did not result from the Purkinje autorhythmicity. Since the ventricular fiber model does not initiate spontaneous APs, ectopic APs were detected more easily in these fibers (Figure 3.5c).

3.1.5 *Prediction of cardiac stimulation thresholds of gradient coils*

Cardiac stimulation thresholds were simulated for the X-, Y-, and Z-axis coils of the actively shielded whole-body Siemens Sonata gradient ($G_{max} = 40$ mT/m, $S_{max} = 200$ T/m/s, Siemens Healthineers, Erlangen, Germany). The coil was loaded with the male and female human body models head-first supine with the head at isocenter. The body models were cropped above the neck and below the hips to simplify the simulations with no significant effect on the cardiac threshold prediction. Fig-

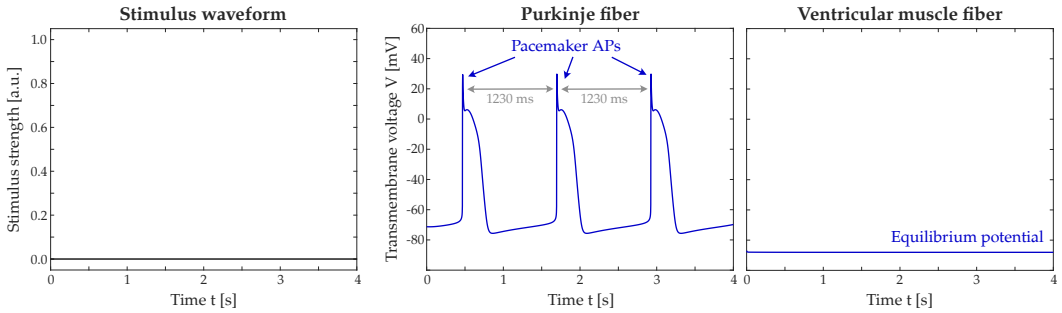

(a) No external stimulus is applied. The ventricular fiber model remains at its equilibrium potential of ca. −87 mV (O'Hara et al., 2011), while the Purkinje fiber model initiates spontaneous pacemaking action potentials every 1230 ms.

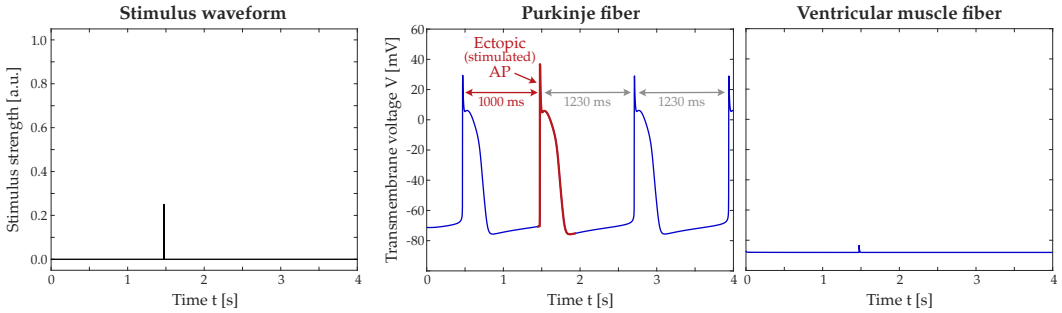

(b) An external stimulus is applied as a block pulse at $t_0 = 1475$ ms with a duration of 0.25 ms. The Purkinje fiber model produces an ectopic action potential right after application of the stimulus at t_0, after which it returns to its normal pacemaking rhythm. The ventricular fiber model only shows a transient increase in transmembrane potential in response to the stimulus before returning to its equilibrium potential.

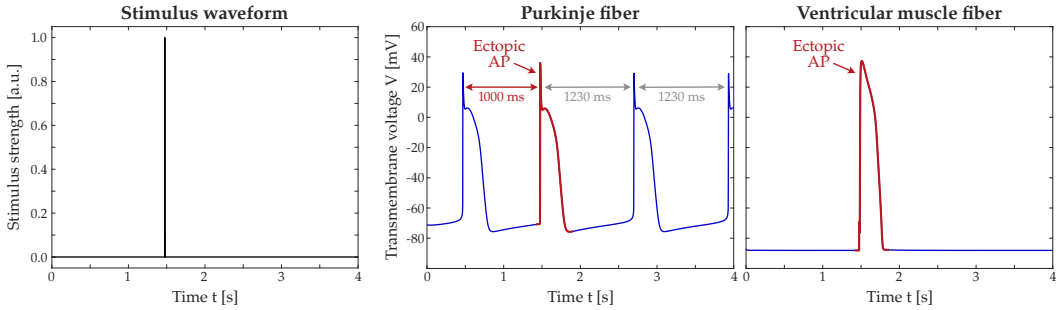

(c) The amplitude of the external stimulus is increased by a factor of four. In this case, both fiber models generate ectopic action potentials right after application of the stimulus at $t = t_0$.

Figure 3.5: Generation of action potentials (APs) in the Purkinje model (Stewart et al., 2009) and the ventricular muscle fiber model (O'Hara et al., 2011) by extracellular electric field stimuli. The left column shows the amplitude of the electric field stimulus as a function of time. The central column shows the transmembrane voltage (TMV) at the central point of the Purkinje fiber, and the right column shows the TMV at the central point of the ventricular muscle fiber over time. Both simulated fibers were 50 mm long, and stimulated by the electric field created by a point source located 10 mm above the fiber center.

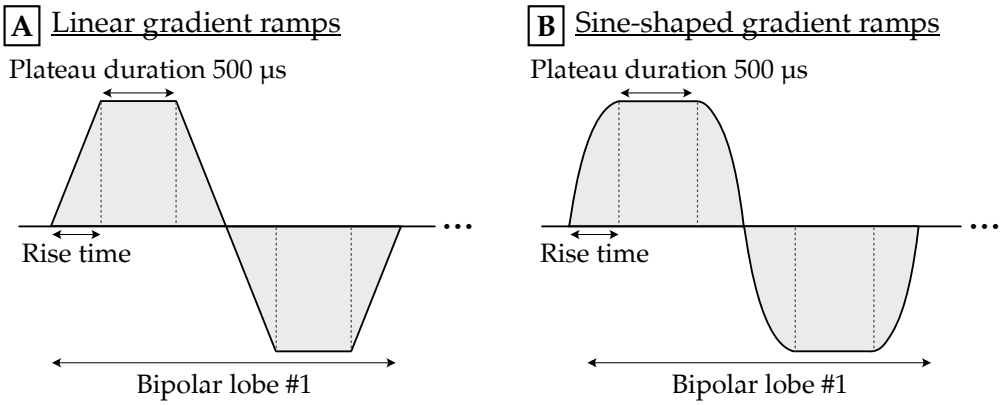

Figure 3.6: Gradient waveforms with linear (A) and sine-shaped (B) ramps used for the simulation of cardiac stimulation thresholds of two commercial MRI gradient systems. Only one of ten bipolar lobes is shown.

ure 3.6 shows the simulated gradient waveforms with sinusoidal and linear ramps and a plateau duration of 500 µs between the ramps. The modeled waveforms consisted of ten bipolar pulses, and CS thresholds were simulated for ten discrete rise times between 0.1 ms and 5.0 ms. In addition to the Sonata gradient, the Y-axis coil of the Siemens Connectome gradient ($G_{max} = 300$ mT/m, $S_{max} = 200$ T/m/s) was loaded with the female body model with the head at isocenter and CS thresholds were simulated for a gradient waveform with sinusoidal ramps.

Stimulation thresholds G_{thresh}, i. e., the smallest gradient field amplitude that triggered an AP, were determined with a titration process: The fibers were stimulated with a given gradient amplitude G_{stim}. If no AP was created in response to the stimulus, the current gradient amplitude was set as the lower limit G_{low}, and the stimulus amplitude was doubled ($2 \cdot G_{stim}$) for the next excitation. If an AP was created, the current gradient amplitude was set as the upper limit G_{high} and the stimulus amplitude was halved ($0.5 \cdot G_{stim}$) for the next excitation. This process was repeated until the difference between the maximum gradient amplitude G_{low} that did not create an AP and the minimum gradient amplitude G_{high} that did create an AP was less than a certain titration tolerance G_{tol}:

$$G_{upper} - G_{lower} \leqslant G_{tol}. \tag{3.9}$$

G_{tol} was chosen to be $\leqslant 1\%$ of the stimulation threshold. The threshold titration was repeated for both Purkinje and ventricular muscle fibers and for all gradient waveforms with different rise times and ramp shapes.

In addition to these threshold simulations, the influence of the plateau duration and the number of bipolar lobes (Figure 3.6) on the CS threshold was investigated. To this end, thresholds were simulated in the female body model placed in the Z-axis coil of the Sonata gradient with the head at isocenter. A total of 39 waveforms with a constant rise time of 0.5 ms were simulated. For each waveform, either the plateau duration was varied between 0.0 ms and 10.0 ms, or the number of bipolar pulses was varied between one and 20.

3.1.6 *Prediction of electric field strength-duration curves*

As explained in Section 2.3.3, the response of excitable nerve and muscle tissue to an externally applied E-field is commonly evaluated using strength-duration curves (Geddes and Bourland, 1985a; Irnich, 2008; Mogyoros et al., 1996; Mouchawar et al., 1989). These curves quantify the threshold for AP generation in terms of the smallest amplitude of a unipolar rectangular E-field pulse as a function of the pulse duration. In most magnetostimulation studies, such an E-field pulse is created experimentally by playing a trapezoidal coil current (or, equivalently, B-field) pulse with a linear ramp. In this case, the duration of the E-field pulse is equal to the duration of the magnetic field ramp dB/dt. Typically, a long flat-top period of the B-field pulse is chosen, i. e., long in comparison to the chronaxie or time constant of the tissue (Equation 3.10 and Equation 3.11). This allows the membrane potential of the excited tissue to go back to equilibrium before the B-field is ramped back down to zero, which induces a second rectangular E-field pulse with negative amplitude that may affect the stimulation threshold if applied shortly after the first E-field pulse.

The male and female body models were placed in the Siemens Sonata gradient coil head-first supine with the head at isocenter, and ten discrete dB/dt or E-field pulse durations between 0.2 ms and 10.0 ms were simulated. The slope of the magnetic field ramp dB/dt was increased until an ectopic AP was elicited in the Purkinje or ventricular muscle fiber networks. The stimulation threshold was determined with a titration process, as described above. The amplitude of the induced E-field was then sampled along the path of the most sensitive cardiac fiber, and scaled with the threshold coil current derivative (Equation 3.6). The maximum E-field value along the fiber was evaluated as a function of the pulse duration to determine the strength-duration curve. The simulated curves were fitted with a non-linear least-squares solver (function `lsqcurvefit` in Matlab) with two expressions that are widely used in the tissue stimulation literature:

- The hyperbolic *Lapicque* expression (Lapicque, 1909):

$$E(\tau) = E_{rheo} \cdot (1 + t_{chron}/\tau), \tag{3.10}$$

  where τ is the E-field pulse duration, and t_{chron} is the chronaxie time, defined as the time at which the stimulation threshold is twice the long-duration asymptote E_{rheo}, the so-called "E-field rheobase".

- The exponential *Blair* expression (Blair, 1932):

$$E(\tau) = E_{rheo}/(1 - \exp(-\tau/t_c)). \tag{3.11}$$

  Here, τ is the pulse duration, E_{rheo} denotes the E-field rheobase, and t_c the membrane time constant.

3.1.7 *Preliminary model validation in canine models*

A preliminary validation of the CS modeling framework was based on a comparison with canine experiments conducted by Mouchawar and Nyenhuis and colleagues in

the early 1990s (Mouchawar et al., 1992; Nyenhuis et al., 1992). These experimental studies measured the cardiac magnetostimulation threshold in anesthetized canines by discharging capacitors into coils placed close to the canine chest. The resulting electromagnetic pulses (EMPs) evoked ectopic heartbeats that were detected on ECG and arterial blood pressure signals (Mouchawar et al., 1992; Nyenhuis et al., 1992). The canine experiments were replicated as closely as possible with the simulation workflow described above.

Generation of canine body models

The HML voxel models are freely available for research purposes (Kramer et al., 2012).

For the canine simulations, the Human Monitoring Laboratory (HML) body model of an adolescent dog (Kramer et al., 2012) (14 kg, height to withers 44 cm, 20 tissue classes) was used. This model has originally been developed for radiation dosimetry simulations and was created from computed tomography (CT) images of a sedated Doberman (Kramer et al., 2012). The HML model only possesses a description of the outer myocardial surface, but does not include a description of the blood-filled heart chambers, i. e., the atria and ventricles. It is important to distinguish the heart chambers from the myocardium to 1) correctly model the effect of myocardium/blood conductivity interfaces in the E-field simulations, and 2) allow modeling of the cardiac fiber networks. The insufficient detail of the HML canine model was thus remedied by inserting the atrial and ventricular surfaces of the female Zygote body model using scaling, translation, and rotation operations.

In the next step, five larger canine models were generated from the HML model by applying geometrical scaling to all tissues and organs, including the heart. The scaling factor was chosen so the resulting models matched the minimum, mean, or maximum weight of the canines used in the Mouchawar study (Mouchawar et al., 1992) (minimum 17 kg, mean 21.5 kg, maximum 26 kg) and the Nyenhuis study (Nyenhuis et al., 1992) (minimum 17 kg, mean 24.5 kg, maximum 32 kg).

For the electrophysiological simulations, the same cardiac fiber diameters were used as for the simulations in the human body models, i. e., 80 µm for the Purkinje and 15 µm for the ventricular muscle fibers. This should be a reasonable choice, since for canines, Purkinje fiber diameters are in the 20-200 µm range (Argentieri et al., 1990; Rosen et al., 1981), while ventricular fibers are around 12 µm in diameter (Carew and Covell, 1979).

Simulation of the experimental setup

Figure 3.7 shows the simulation setup that was used for the prediction of CS thresholds in the canine body models. The same coils were modeled as used in the experimental studies (Mouchawar et al., 1992; Nyenhuis et al., 1992), namely: 1) a pair of coplanar flat spiral coils placed on the left side of the canine's torso (30 wire turns each, inner coil diameter 7 cm, outer diameter 17 cm, referred to as "COP") (Mouchawar et al., 1992), and 2) a solenoid coil enclosing the canine's torso (24 wire turns, coil diameter 26 cm, length 13 cm, referred to as "SOL") (Nyenhuis et al., 1992). Both coil configurations were centered on the canine heart. The study using the solenoid coil measured CS thresholds for different orientations of the coil's B-field relative to an external static B-field of $B_0 = 1.5$ T that was oriented from the

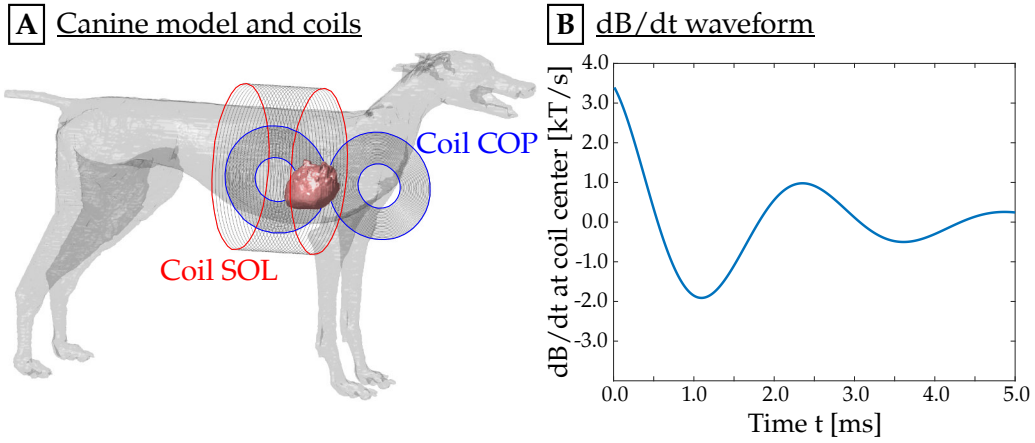

Figure 3.7: Simulation setup for comparison of the cardiac stimulation modeling framework with previous canine experiments (Mouchawar et al., 1992; Nyenhuis et al., 1992). (A) Canine body model (only the skin and myocardial surfaces are shown) with a pair of coplanar coils (COP) and a solenoid coil (SOL). (B) Damped sinusoidal dB/dt waveform as generated in the experimental studies by discharging a capacitor into the coils. The figure is taken from (Klein et al., 2021).

canine's tail to head or head to tail (Nyenhuis et al., 1992). Comparing their results to another study in canines conducted with $B_0 = 0$ T (Bourland et al., 1991), the authors concluded that the static B-field had no significant effect on the CS threshold (Nyenhuis et al., 1992). In this work, all simulations were done without an external static B-field, i. e., $B_0 = 0$ T. The solenoid coil study also reported CS thresholds for different positions of the canines in the coil (dorsal, left and right lateral). Since the HML canine model was based on CT images of a sedated canine lying supine (Kramer et al., 2012), the simulated results were compared to the measurements with canines placed in the dorsal position to mimic a similar positioning of the internal organs in the computational body model compared to the experiments.

In the experiments, capacitors with capacitances of 682 µF (Mouchawar et al., 1992) and 820 µF (Nyenhuis et al., 1992), respectively, were discharged into the coils. The capacitor discharges resulted in damped sinusoidal coil current waveforms (Equation 3.12). The durations from onset to the first zero-crossing of the induced current (or, equivalently, the dB/dt waveform) was equal to 571 µs for COP and 540 µs for SOL (Mouchawar et al., 1992; Nyenhuis et al., 1992). These waveforms were reproduced in the simulations (Figure 3.7).

3.2 EXPERIMENTAL STUDY OF CARDIAC MAGNETOSTIMULATION IN PIGS

In the second part of this work, an experimental study was performed to measure the magnetostimulation threshold of the porcine heart. The following section describes the materials and methodology used to perform these measurements.

3.2.1 *Comparison of different coil and amplifier configurations*

First, a magnetic stimulator had to be constructed to generate EMPs strong enough to stimulate the porcine heart. To this end, different coil and current amplifier configurations were tested prior to construction with the help of EM field simulations. The IT'IS model of a male pig shown in Figure 3.8 was used to simulate E-fields using Sim4Life's low-frequency magnetoquasistatic solver for a 1 A, 1 kHz sinusoidal coil current. The IT'IS porcine model has a weight of 35 kg and includes 65 tissue classes, to which electrical conductivity values were assigned using the dispersion relations by Gabriel et al. (Gabriel et al., 1996a,b). E-fields were simulated at 2x2x2 mm^3 isotropic resolution for different coil geometries. Figure 3.8 shows a subset of the candidate coil geometries that were simulated:

The IT'IS porcine model can be downloaded from `https://doi.org/10.13099/VIP91301-01-0`.

- A commercial transcranial magnetic stimulation (TMS) coil (MagVenture MRi-B91, Alpharetta, GA, USA) that consisted of two coplanar coils with four wire loops each, wound in two parallel layers. The coil inductance and resistance were 11 µH and 17 mΩ, respectively, according to the manufacturer. The coil was placed in different orientations with respect to the porcine body model to find the configuration that led to the highest E-field in the heart.
- The coplanar coil pair with 30 wire turns per coil, inner coil diameter $D_{in} = 7$ cm, and outer diameter $D_{out} = 17$ cm. A similar coil was used in one of the previous canine experiments (Mouchawar et al., 1992), which reported the coil inductance as 220 µH.
- Solenoid coils enclosing the pig's torso with varying parameters: 40 to 50 cm diameter, 10 to 20 cm length, and between 10 and 40 wire turns (shown in Figure 3.8: 40 cm diameter, 10 cm length, 20 turns). The coil inductance was simulated using the tool `FastHenry2` to be ca. 230 µH.

`FastHenry` is an open-source software for the simulation of self- and mutual inductances and resistances of generic conductive structures developed by Mattan Kamon at the Massachusetts Institute of Technology, Cambridge, MA, USA.

- A curved spiral coil fitting the porcine torso ($D_{out} = 30$ cm, $D_{in} = 10$ cm, 30 turns). The left front leg of the pig model was placed inside the inner opening of the coil. The coil inductance was ca. 180 µH (simulated with `FastHenry2`).
- Flat spiral coils with varying parameters: D_{out} = 20-40 cm, D_{in} = 1-30 cm, between 20 and 50 turns (shown in Figure 3.8: $D_{out} = 40$ cm, $D_{in} = 2.5$ cm, and 38 turns). The coil inductance was ca. 230 µH (simulated with `FastHenry2`).

Three types of coil current amplifiers were compared in the simulations:

- A commercial TMS amplifier by MagVenture. The TMS amplifier in combination with an inductive coil forms an RLC circuit with a maximum charging voltage $U_{max} = 1.8$ kV and a capacitance $C = 180$ µF. It is compatible with coil inductances of up to 18 µH and resistances of up to 20 mΩ.
- A commercial GPA by Siemens Healthineers with a peak voltage of $U_{max} = 2.0$ kV.
- A 680-µF capacitor with a maximum charging voltage of $U_{max} \approx 10$ kV, similar to the setup used in one of the previous experimental canine studies (Mouchawar et al., 1992).

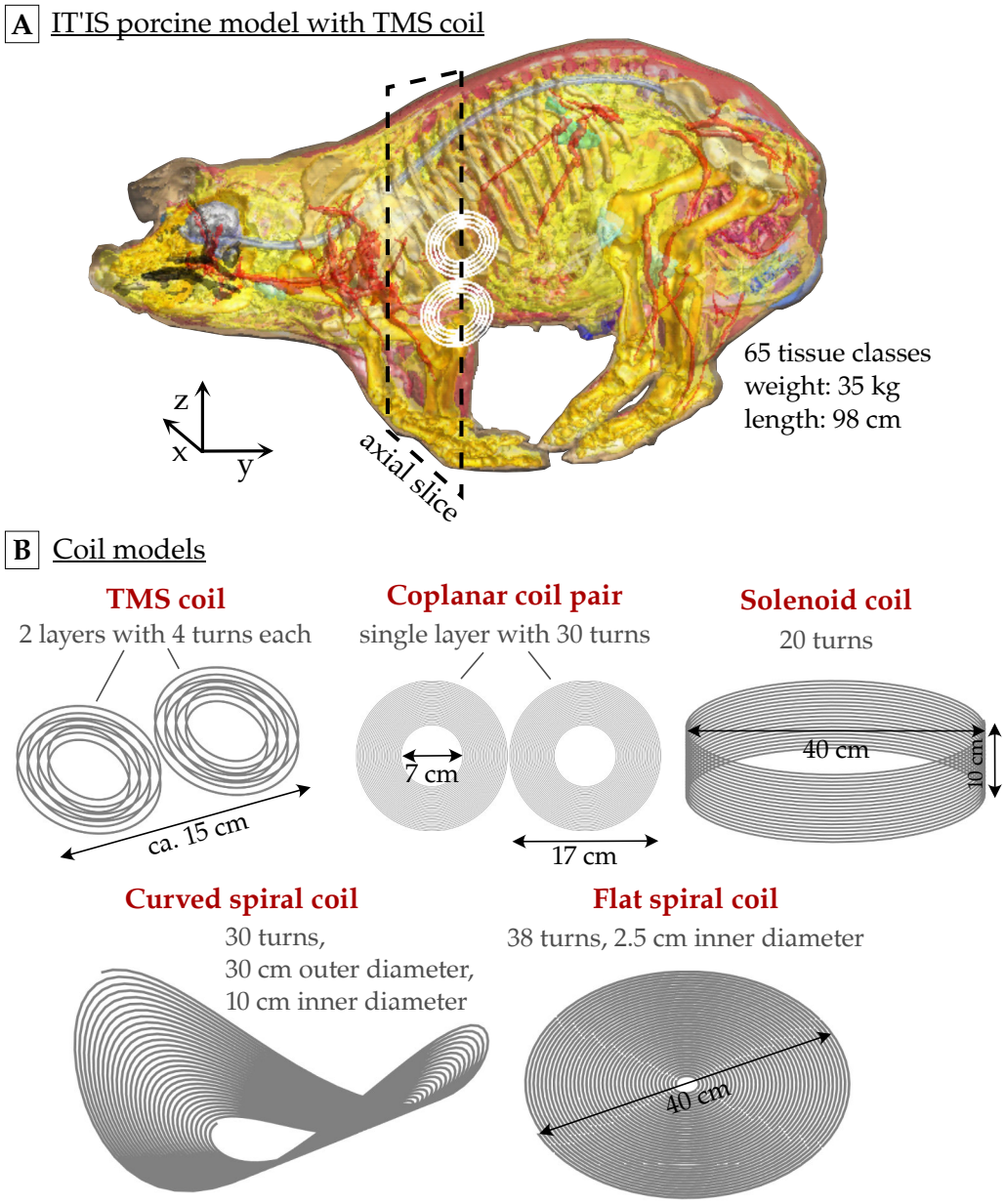

Figure 3.8: (A) IT'IS male porcine body model (IT'IS Foundation, Zurich, Switzerland) with a transcranial magnetic stimulation (TMS) coil placed on the left side of the torso and centered below the heart. (B) Coil geometries for which electromagnetic fields were simulated in the porcine model. The electric field amplitudes created in the porcine heart were compared for different combinations of coils and current amplifiers.

For each coil and amplifier combination, E-fields were simulated in the heart of the IT'IS porcine body model and scaled with the maximum achievable coil current derivative (Equation 3.6). For the resonant circuits, i. e., for coils in combination with the TMS amplifier or the capacitor, the coil current waveform is a damped sinusoid given by

$$I(t) = \frac{U}{\omega L} e^{-\alpha t} \sin(\omega t), \tag{3.12}$$

$$\text{with } \alpha = \frac{R}{2L} \tag{3.13}$$

$$\text{and } \omega = \sqrt{(1/LC) - \alpha^2}, \tag{3.14}$$

where L and R are the total inductance and AC resistance of the circuit, C is the capacitance, and U is the voltage across the capacitor, in the following referred to as "charging voltage". The maximum current derivative is thus reached at $t = 0$ s and is given by

$$\left(\frac{dI}{dt}\right)_{max} = \frac{U_{max}}{L}. \tag{3.15}$$

The same equation can be used to calculate the maximum current derivative generated by the GPA (compare to Equation 2.66). Based on these simulations, a magnetic stimulator consisting of a capacitor bank and a flat spiral coil was constructed, as described in Section 4.2.2.

3.2.2 *Animal preparation*

The study was conducted under a protocol approved by the Massachusetts General Hospital (MGH, Boston, MA, USA) Institutional Animal Care and Use Committee. Ten healthy three-month-old Yorkshire pigs (seven male, three female) with body weights of 20-35 kg were used in the experiments. The animals were pre-anesthetized with Telazol and Atropine, intubated, ventilated with O_2 (mixed with 1-3% isoflurane), and maintained under anesthesia with isoflurane (1-3%). Injections of vecuronium bromide were applied every 20 minutes to suppress motion caused by unwanted skeletal muscle stimulation. The dosage of the first vecuronium injection was 0.25 mg/kg to accustom the animal to the muscle relaxant, subsequent injections were given with a dosage of 0.50 mg/kg.

Vecuronium bromide is a potent muscle relaxant.

3.2.3 *Measurement of cardiac magnetostimulation thresholds*

Figure 3.9 shows the setup of the experiments that were conducted in the control room of a 3T MRI scanner outside of the magnetic B_0-field environment. The pigs were placed in left lateral recumbency on a fiberglass table mounted on a movable cart. Hemodynamic traces were measured during the experiments using a piezo-electric pressure transducer attached to the front right leg of the animal (non-invasive blood pressure) and an infrared photoelectric sensor attached to the right ear (peripheral oximetry, both devices from ADInstruments, Sydney, Australia). These sensor waveforms were acquired with a PowerLab data acquisition device and

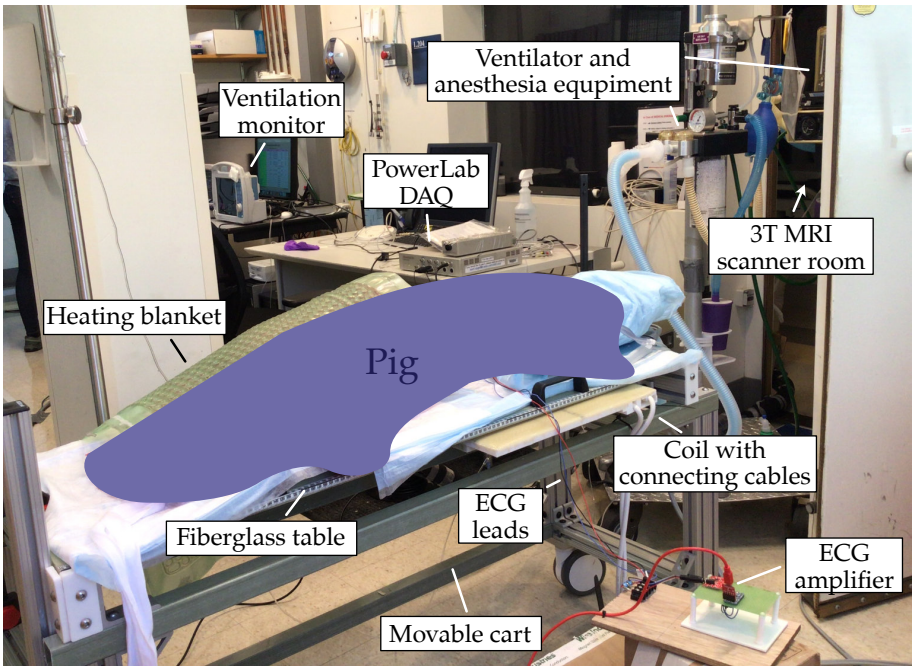

Figure 3.9: Setup of the cardiac magnetostimulation experiments. The pigs were intubated, anesthetized, and placed in left lateral recumbency on a fiberglass table mounted on a movable cart that was constructed mainly from fiberglass beams. The spiral coil was mounted below the fiberglass table.

recorded with the software LabChart (ADInstruments, Sydney, Australia). In seven of the ten pigs, single-lead ECG signals were also acquired during stimulation with electrodes and an ECG amplifier (SparkFun Electronics, Boulder, CO, USA). The ECG signal was recorded with a laptop, and Matlab was used to generate trigger signals at specific delays after the R-wave. These digital signals were converted into optical signals and sent to the magnetic stimulator using a data acquisition device (USB-1208FS by Measurement Computing Corporation, Norton, MA, USA). The delay was chosen manually based on examination of the ECG trace. In the other three pigs, the blood pressure signal was used to trigger the pulses. For those animals, a single-lead BioAmp ECG amplifier (ADInstruments, Sydney, Australia) was used to determine the delay between the peak pressure signal and the R-wave. The BioAmp ECG amplifier was then disconnected prior to stimulation to avoid damages to the device caused by the strong EMPs.

Stimulation experiments were performed at two cardiac phases: on or right after the T-wave (early ventricular diastole) and before the P-wave (late diastole). For each cardiac phase, the stimulation threshold of the heart was established by charging the capacitors at a low voltage (the lowest applied voltage was $U_{min} = 2.0$ kV), and increasing it in increments of 0.25-0.50 kV until stimulation occurred. Stimulation in the form of cardiac capture was assessed by visual inspection of the ECG, blood pressure and oximetry traces. For each pig and trigger time, several charging voltages were applied above and below the threshold for cardiac capture. All measured physiological signals, i. e., ECG, blood pressure and peripheral oximetry, were analyzed and evaluated by an experienced cardiologist.

Ventricular diastole is the part of the cardiac cycle during which the ventricles are relaxed and at resting potential.

Cardiac stimulation thresholds in terms of charging voltage U_{thresh} were determined after the measurement by plotting the binary cardiac response, i. e., successful or unsuccessful cardiac capture, as a function of the charging voltage U and fitting sigmoid functions to the resulting voltage-threshold distribution:

$$F(U) = 1/\left(1 + e^{-(U-U_{thresh})/W}\right), \tag{3.16}$$

where W is the width of the sigmoid function F.

3.2.4 *MR image acquisition*

For eight of the ten pigs, MR image volumes were acquired immediately after the cardiac stimulation experiment. The spiral coil was removed from the fiberglass table, and the animals were moved into a 3T Siemens Connectome MRI scanner. During this procedure, the animal's posture and position on the table was changed as little as possible. For two of the pigs, it was not possible to acquire images because of technical difficulties concerning the MRI scanner and experimental time constraints. Fat-water separated Dixon volumes (500x325x344 mm^3 FOV, 2x2x2 mm^3 isotropic resolution, $TR/TE_1/TE_2$=5.00/1.23/2.46 ms) as well as CINE measurements of the beating heart (1.9x1.9x3.0 mm^3 resolution, 45 slices, 23 timeframes, TE/TR=4.9/35.4 ms, double oblique along the heart short axis) were acquired. The Dixon volumes were acquired in four bed positions separated by 200 mm along the z-axis, which were concatenated in postprocessing to obtain whole-body fat-water-separated images.

Dixon imaging uses two distinct echo times to separate fat and water signals (Section 2.1.6).

The position of the heart relative to the fiberglass table was inferred using four fiducial markers (vitamin E capsules), which were attached to the table and visible in the Dixon images. The longitudinal and lateral position of the coil relative to the table was measured during the stimulation experiments. These measurements enabled retrospective calculation of the coil position with respect to the animal's heart. The vertical distance of the wire from the table surface was 19 mm. This is the sum of the table thickness, the depth of the wire in the coil former, and the thickness of the combination of fiberglass cloth and epoxy resin that was added on top of the coil, as described in Section 4.2.2.

3.2.5 *Generation of porcine body models from MR images*

Porcine body models were generated from the MR Dixon and CINE images acquired in eight of the ten pigs (Section 3.2.4) using a semi-automatic segmentation pipeline. Electric conductivity values were assigned to the different tissue classes based on the IT'IS low-frequency material database (Hasgall et al., 2018) for subsequent E-field simulations.

First, the local relative fat/water content $S_{FW} = S_F/(S_F + S_W)$ was determined based on the fat- and water-weighted Dixon images S_F and S_W. Electric conductivity values were assigned to each voxel according to

$$\sigma = S_{FW} \cdot \sigma_F + (1 - S_{FW}) \cdot \sigma_M, \tag{3.17}$$

with the fat conductivity $\sigma_F = 0.057$ S/m (Hasgall et al., 2018) and the muscle conductivity $\sigma_M = 0.355$ S/m (Hasgall et al., 2018). The voxels were then grouped into six different tissue classes according to their conductivity, ranging from pure fat to pure muscle, as well as mixed tissue classes with 30%, 50%, 70%, and 90% water/-muscle content. In the next step, the lung was segmented semi-manually using the flood-filling algorithm of Matlab's `Image Segmentation` application and assigned with a conductivity of 0.11 S/m (Hasgall et al., 2018). The outermost voxel layer was assigned as skin (0.17 S/m (Hasgall et al., 2018)). Voxels with low signal intensity of less than 20% on both the fat- and water-weighted Dixon images were set as low-conductive tissue and assigned with the conductivity of cortical bone (3.5 mS/m (Hasgall et al., 2018)). Finally, the resulting segmentation was interpolated at 1x1x1 mm^3 isotropic spatial resolution.

The myocardium (0.381 S/m (Hasgall et al., 2018)), the ventricles, atria, and major blood vessels connecting to the heart (all set to blood with 0.660 S/m (Hasgall et al., 2018)) were segmented manually on a diastolic timeframe of the CINE data. A tetrahedral mesh was created of the segmented heart, which was then smoothed and re-voxelized at an isotropic resolution of 1x1x1 mm^3 using the `iso2mesh` toolbox in Matlab. This was done to reduce unrealistically sharp edges at the tissue boundaries in the E-field simulation. Finally, the heart segmentation was transferred into the whole-body voxel model using translation and rotation operations based on the relative orientations of the CINE and Dixon image volumes. In the last step, the final voxel model was smoothed with a 3x3x3-voxel median filter.

`iso2mesh` is an open-source mesh generation and processing toolbox developed by Qianqian Fang at the Northeastern University, Boston, MA, USA.

3.2.6 *Biot-Savart and E-field simulations*

For each animal, the spiral coil's B-field map registered to the MRI-based porcine body model was calculated using Biot-Savart's law at 1 A coil current. The B-field was then scaled with the experimental threshold current amplitude I_{thresh} leading to cardiac capture, i. e., stimulation of the heart. This calculation allowed to estimate the B-field and dB/dt values at threshold (B_{thresh} and dB/dt_{thresh}) in the body model created for each animal. In particular, dB/dt_{thresh} was evaluated at the center of the heart, as average, minimum, and maximum values in the heart volume, and as a maximum in the whole porcine body. For the two pigs for which no MR images were acquired, dB/dt was instead evaluated 11 cm above the coil center, which corresponded to the average distance between the coil and heart center in the other pigs.

Electric fields were simulated in the eight porcine body models using the low-frequency magnetoquasistatic solver by Sim4Life for a 1 A, 1 kHz sinusoidal coil current. The E-field was then scaled with the derivative of the measured threshold current $(dI/dt)_{thresh}$:

$$E_{thresh} = \frac{E_{sim}\,(1\text{ A}, 1\text{ kHz})}{2\pi \cdot 1\text{ kHz}} \left(\frac{dI(t)}{dt}\right)_{thresh}. \tag{3.18}$$

This scaling is equivalent to the one used previously to calculate E-fields induced by gradient coils in human body models (Equation 3.6). The E-field in the porcine heart was evaluated as the 95^{th} percentile of all voxels in the myocardium to reduce bias

by unphysically high E-field amplitudes simulated at tissue boundaries (staircasing artifacts).

In the next step, simulations were performed to compare the experimental porcine threshold dB/dt and E-field values with maximum values induced by MRI gradient coils in the human heart. To this end, dB/dt and E-field values created by the X-, Y-, and Z-axis coils of three commercial MRI gradient systems were simulated in the heart of the male adult Zygote body model, which was described in detail in Section 3.1.1. The body model was placed in the Siemens Sonata ($G_{max} = 40$ mT/m, $S_{max} = 200$ T/m/s), Quantum ($G_{max} = 40$ mT/m, $S_{max} = 140$ T/m/s), and Connectome gradient coils ($G_{max} = 300$ mT/m, $S_{max} = 200$ T/m/s). The simulated dB/dt and E-field values were scaled to the maximum output of each gradient system within its respective hardware limits for a gradient waveform with linear ramps and an effective stimulus duration of $t_{s,eff} = 0.45$ ms, which is equal to twice the rise time. According to the IEC definition (IEC, 2010), this stimulus duration corresponds to the damped sinusoidal B-field waveform used in the porcine experiments. The workflow for these calculations was as follows:

The effective stimulus duration is equivalent to the duration it takes to slew from the minimum to maximum gradient field amplitude (IEC, 2010).

- First, the gradient coil's B-field was simulated for a 1 A coil current (B_{1A}).
- The maximum gradient field amplitude G_{scale} achievable with the gradient's maximum slew rate S_{max} was calculated for $t_{s,eff} = 2 \cdot t_{rise} = 0.45$ ms as follows:

$$G_{scale} = \frac{S_{max} \cdot t_{s,eff}}{2}. \tag{3.19}$$

  If $G_{scale} > G_{max}$, then G_{scale} was derated to the maximum gradient field amplitude ($G_{scale} = G_{max}$).
- B_{1A} was scaled with the maximum achievable coil current, which is given by the gradient strength G_{scale} and the gradient field efficiency ϵ_G (in mT/m/A):

$$B_{max} = \frac{G_{scale}}{\epsilon_G} \cdot B_{1A}. \tag{3.20}$$

- Finally, the gradient coil's maximum B-field rate dB/dt_{max} achievable for $t_{s,eff} = 0.45$ ms was calculated as

$$dB/dt_{max} = \frac{B_{max}}{t_{s,eff}/2}. \tag{3.21}$$

The B-field rate dB/dt_{max} was evaluated at two locations in the coil: 1) within a 0.2-m radius cylinder placed along the *z*-axis, which corresponds to the IEC definition of the "compliance volume" within which the dB/dt safety limits are defined (IEC, 2010), and 2) within the heart of the body model. The heart location in each gradient system was estimated for two scan positions, namely for placing the body model with the head or the heart at the gradient isocenter, respectively, as shown in Figure 3.10.

As for the previous E-field simulations (Section 3.1.3), the 25 tissue classes of the body model were assigned with electrical conductivity values based on the IT'IS low-frequency material database (Hasgall et al., 2018). The E-field was again simulated

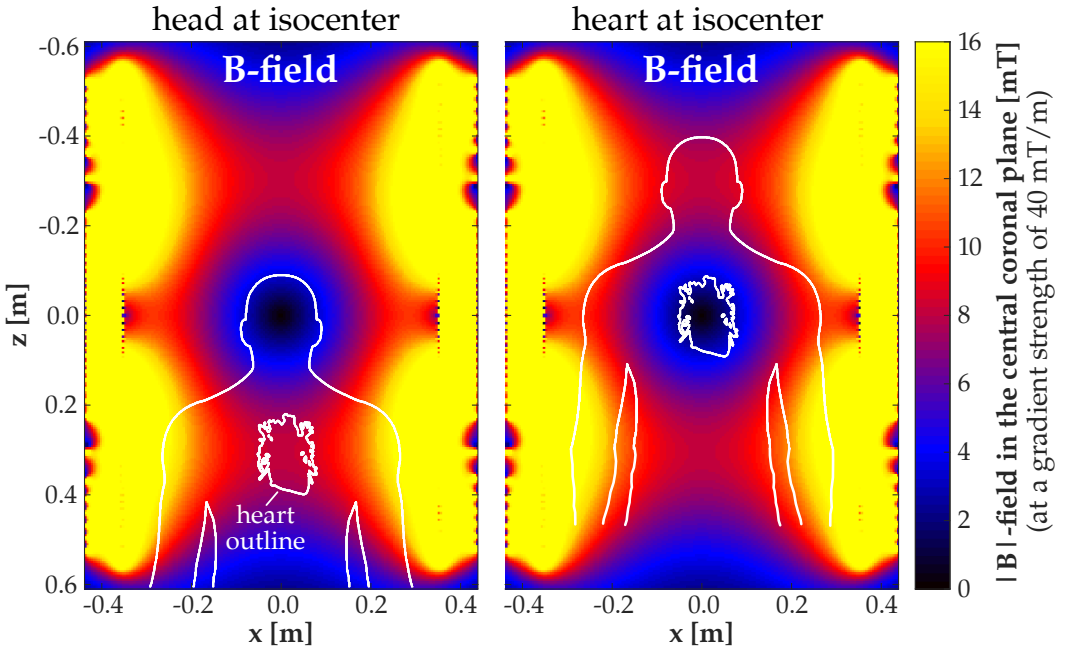

Figure 3.10: Male human Zygote body model (skin and heart outline shown as projections onto the coronal plane) placed in the magnetic field created by the Y-axis coil of the Siemens Sonata gradient system at maximum gradient strength ($G_{max} = 40$ mT/m). The left plot shows the body model with its head placed at isocenter, the right plot shows the body model with its heart placed at isocenter. The figure is taken from (Klein et al., 2022).

for a 1 A, 1 kHz sinusoidal coil current and then scaled according to Equation 3.18 to match a gradient waveform with a rise time of $t_{s,eff}/2$. In this case, the maximum current derivative of the gradient coil is given by

$$\frac{dI}{dt} = \frac{G_{scale}}{\epsilon_G} \cdot \frac{1}{t_{s,eff}/2}, \tag{3.22}$$

with the maximum gradient field amplitude G_{scale} achievable for $t_{s,eff} = 0.45$ ms calculated according to Equation 3.19.

3.3 PREDICTION OF CARDIAC MAGNETOSTIMULATION IN PORCINE MODELS

The third part of this thesis combined the cardiac magnetostimulation threshold measurements in pigs with the modeling pipeline developed for the prediction of CS by time-varying magnetic fields.

3.3.1 *Prediction of porcine cardiac stimulation thresholds*

Cardiac stimulation thresholds were simulated in the eight MRI-based porcine body models using the same modeling pipeline as described in Section 3.1 for the human and canine body models. First, subendocardial Purkinje fiber networks and ventricular myocardial fibers were added to the 3D segmentation of the porcine myocardium using rule-based algorithms (Bayer et al., 2012; Ijiri et al., 2008). Next, the

E-field simulated in the porcine body models was interpolated along the cardiac fiber paths, projected, and integrated to obtain electric potential changes along the fibers. The electric potential was modulated in time with the magnetic field waveform used in the porcine cardiac magnetostimulation experiments (a damped sine wave with $t_{s,eff} = 0.45$ ms). The resulting spatio-temporal potential changes were fed into the same electrophysiological models for Purkinje and ventricular muscle fibers used in the previous simulations (O'Hara et al., 2011; Stewart et al., 2009). A titration process was used to determine the threshold at which an AP was created in either fiber type. The output of the simulations in each porcine model was the predicted CS threshold in terms of capacitor charging voltage.

3.3.2 *Sensitivity analysis of simulated cardiac stimulation thresholds*

For each porcine model, five subendocardial Purkinje networks were generated using the semi-random rule-based fiber modeling algorithm proposed by Ijiri et. al (Ijiri et al., 2008). CS thresholds were simulated for each of these networks to quantify the effect of small changes in the Purkinje fiber paths. In one of the porcine body models (pig #7), a preliminary sensitivity analysis was performed to assess the effect of variations of important model parameters on the predicted CS threshold. For this analysis, CS thresholds were simulated in the most sensitive of the five Purkinje fiber networks modeled in pig #7.

The first investigated effect on the CS thresholds was the variation of important electrophysiological parameters of the Purkinje fiber model (Table 3.1). Specifically, the cell diameter, the specific membrane capacitance, the specific axial resistivity, and the gap junction conductance were each varied separately by ± 50 %, while all other parameters were held constant at their initial values. Note that the investigated parameters are not all independent: The cell diameter is proportional to the membrane capacitance (Equation 3.8) and the square root of the axial conductance (Equation 3.7). In addition to these model parameters, the impact of $\pm 50\%$ variations of the fast sodium conductance G_{Na} and the inward rectifier potassium conductance G_{K_1} was assessed. These conductances control the sodium and potassium ionic currents of the Stewart model (Stewart et al., 2009) of Purkinje cells (Figure 3.4).

The second investigated effect on the E-field in the heart and the predicted CS threshold was that of varying electrical conductivity values of the myocardium, muscle, blood, and lung tissues. The conductivity of each of these tissues was varied individually by $\pm 50\%$ relative to their default values (IT'IS LF database (Hasgall et al., 2018)). Additionally, one simulation was conducted in which the lung tissue was assigned the conductivity of "deflated lung" (0.529 S/m (Hasgall et al., 2018)), which is five-fold higher than the IT'IS database value for average lung tissue used in all other simulations (0.105 S/m (Hasgall et al., 2018)).

Finally, the effect of small changes in the coil position relative to the porcine body was investigated. To this end, the coil was shifted from its default position by ± 1 cm in the x-, y-, and z-direction, and E-fields and CS thresholds were simulated for each position.

4 RESULTS

This chapter is divided into three sections. The first section describes the prediction of cardiac magnetostimulation in human body models and the preliminary model validation study in canine body models. The second section reports the magnetostimulation measurements in the porcine heart. Finally, the third section presents the prediction of cardiac stimulation thresholds for the experimental setup of the porcine measurements. Parts of this chapter have been published in (Klein et al., 2021) by John Wiley & Sons[1] and submitted as (Klein et al., 2022). The description of the corresponding results is partly replicated here.

4.1 PREDICTION OF CARDIAC STIMULATION IN HUMAN MODELS

4.1.1 *Predicted cardiac stimulation thresholds of MRI gradients*

The simulated efficiency of the Siemens Sonata gradient was $\epsilon_G \approx 0.092$ mT/m/A for all axes in the FOV, which is in agreement with the manufacturer's specifications. Figure 4.1 shows the E-fields induced in the male and female human body models by the Sonata Z-axis gradient coil (head at isocenter). The E-fields in these plots were simulated for a 1 A, 1 kHz sinusoidal current waveform and then scaled to match a maximum slew rate of $SR_{max} = 100$ T/m/s. This was achieved by setting the term $G_{target} \cdot \frac{dW}{dt}$ in Equation 3.6, i. e., the temporal change of the gradient field strength, to the target slew rate.

As can be seen in the coronal E-field slice (central column), the E-field in the heart was significantly lower than in the surrounding tissues, especially in the adjacent lung tissue. In particular, the 95th percentile E-field amplitude in the myocardium was $E_{95} = 1.2$ V/m for the male model, and 0.9 V/m for the female model at a slew rate of 100 T/m/s. For comparison, the peak E-field amplitude in the whole torso was 9.5 V/m for the male model, and 14.2 V/m for the female model.

Figure 4.2 shows maximum intensity projections (MIPs) of the E-field induced in the heart of the body models by each axis of the Sonata gradient at $SR_{max} = 100$ T/m/s. The E-field distributions are highly heterogeneous, and the overall E-field amplitudes are higher in the male than in the female model. For both body models, the Z-axis coil induced the highest E-field values in the myocardium, followed by the X-axis coil, which induced particularly high E-field values around the apex, i. e., the tip of the heart. The Y-axis coil induced high E-field values in the vena cava, aorta and pulmonary artery, but comparatively low values in the myocardium itself.

Figure 4.3 shows CS thresholds simulated in the male and female body models for the three axes of the Sonata gradient driven with a gradient waveform with sinusoidal ramps, 500 µs plateau duration, and ten bipolar pulses. In addition to the

1 © 2020 The Authors. Magnetic Resonance in Medicine published by Wiley Periodicals LLC on behalf of the International Society for Magnetic Resonance in Medicine.

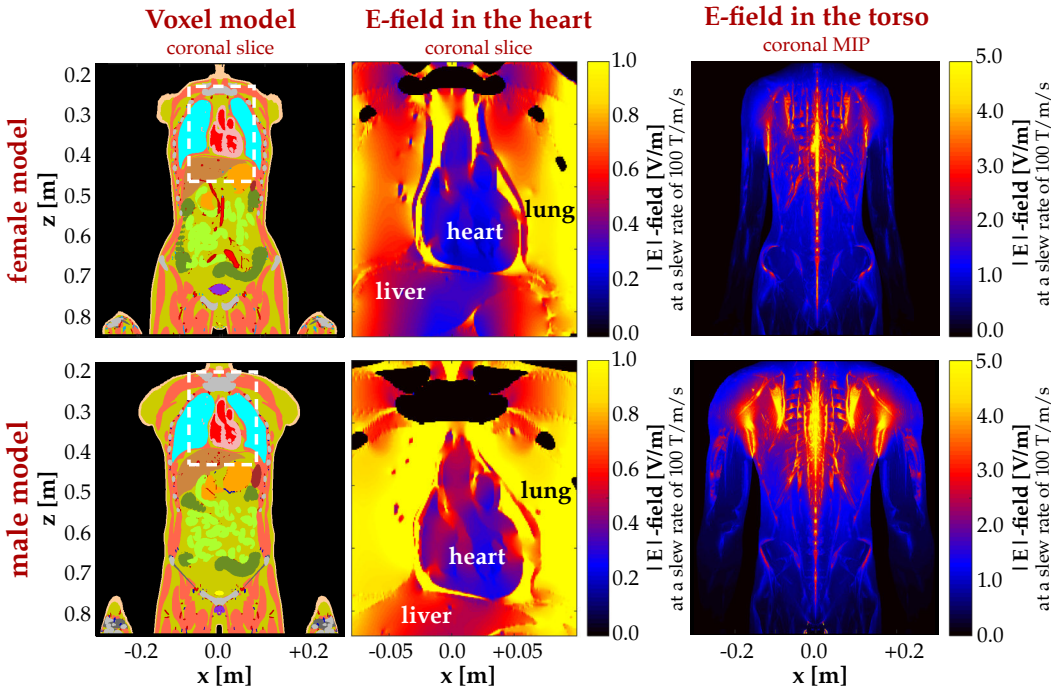

Figure 4.1: Coronal slices of the voxel models generated from the male and female Zygote body models (left column). The center column shows an enlarged section (indicated by the dashed box in the left column) of the electric field (E-field) induced in this slice by the Z-axis coil of the Siemens Sonata gradient at a slew rate of 100 T/m/s. The right column shows E-field maps in the whole torso as maximum intensity projections (MIPs) of E-field values along the y-direction onto the xz-plane. The E-field in the bones is set to zero for better visibility. The figure is taken from (Klein et al., 2021).

simulated stimulation thresholds of the Purkinje and ventricular fibers (red triangles and diamonds, respectively), the cardiac safety limit defined by the IEC 60601-2-33 regulatory guidelines (IEC, 2010) is shown in black, and the simulated PNS thresholds are shown in blue. For all gradient axes and both body models, the Purkinje fibers were between three and 20 times more sensitive to stimulation, i. e., had lower stimulation thresholds, than the ventricular fibers. For both body models and all axes of the Sonata gradient, the predicted Purkinje fiber thresholds were at least 6-fold (for rise times $t_{rise} > 2.5$ ms) to 25-fold ($t_{rise} < 0.5$ ms) higher than the predicted PNS thresholds, and also substantially higher than the IEC cardiac safety limit, e. g., $\geqslant 11$ times greater at $t_{rise} = 0.5$ ms.

The simulated stimulation thresholds for the gradient waveform with linear ramps (Figure 4.4) showed a qualitatively similar behavior, but were slightly higher than the thresholds for the sine-shaped waveform. In particular, the Purkinje fiber thresholds predicted in the female body model were 1%-33%, the ventricular fiber thresholds 6%-33%, and the simulated PNS thresholds 7%-51% higher for the trapezoidal waveform. For both gradient waveforms, the male body model had similar Purkinje fiber thresholds as the female model for the X- and Z-axis coils, but higher thresholds for the Y-axis coil. Overall, the predicted CS thresholds were lowest for the Z-axis, and highest for the Y-axis coil. This is in alignment with the observation that the Z-

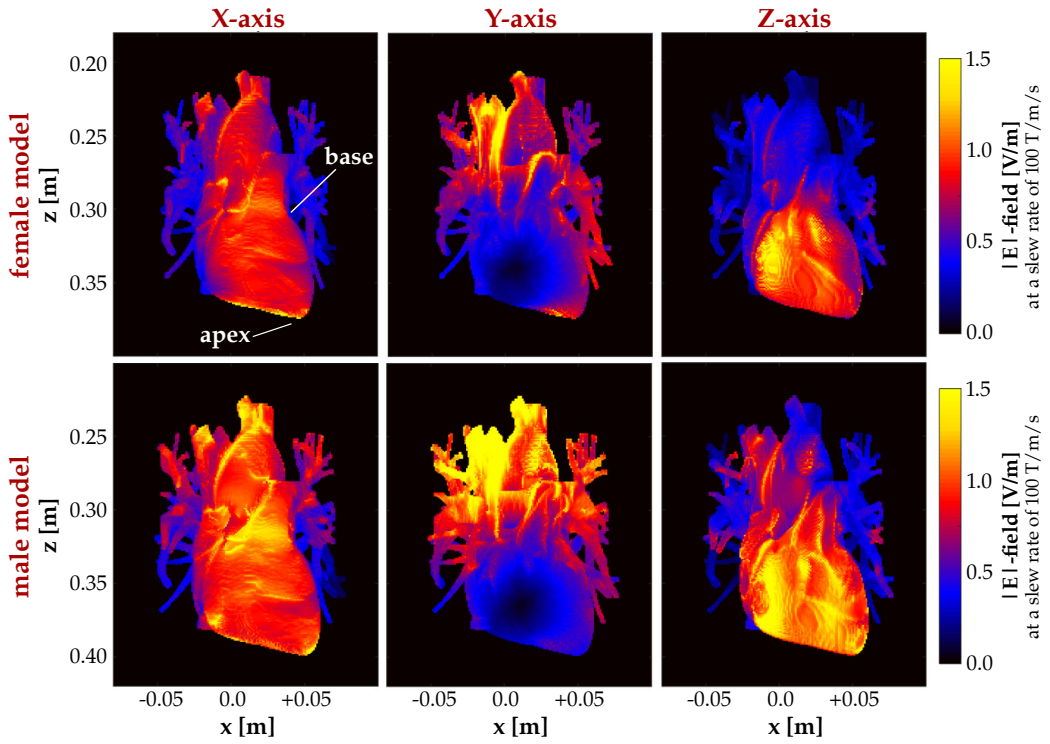

Figure 4.2: Electric field (maximum intensity projection) induced in the myocardium, the vena cava, aorta, and pulmonary arteries of the male and female body models (rows) by each axis of the Sonata gradient (columns) at a slew rate of 100 T/m/s. The electric field was simulated in the full torso model and set to zero outside the heart for better visibility. The figure is taken from (Klein et al., 2021).

axis induced the highest, and the Y-axis coil the lowest E-fields in the myocardium (Figure 4.2).

Figure 4.5 shows Purkinje and ventricular muscle fiber thresholds simulated in the female body model along with experimental PNS thresholds for the Y-axis coil of the Siemens Connectome gradient (Setsompop et al., 2013). For this coil, the margin between the predicted CS thresholds and the IEC cardiac safety limit was even greater than for all axes of the Sonata gradient (e. g., 40 times higher Purkinje fiber threshold at $t_{rise} = 0.5$ ms). The predicted CS thresholds were $\geqslant 30$ times higher than the hardware limit of the Connectome gradient, which is dictated by its maximum gradient strength ($G_{max} = 300$ mT/m) and slew rate ($S_{max} = 200$ T/m/s). Note that Figure 4.5 shows stimulation thresholds predicted for the Y-axis coil, which is in contrast to Figure 2.6, which shows PNS and IEC limits of the Connectome gradient for simultaneous slewing of the X-, Y-, and Z-axis coils.

4.1.2 *Threshold dependence on spatio-temporal electric field changes*

Figure 4.6 shows the E-field magnitude induced by the three axes of the Sonata gradient in the female body model, and sampled along the Purkinje fibers (top row). The bottom row shows the locations where the fibers were first stimulated for a gradient waveform with sine-shaped ramps. The stimulation loci of the 50 most sensitive

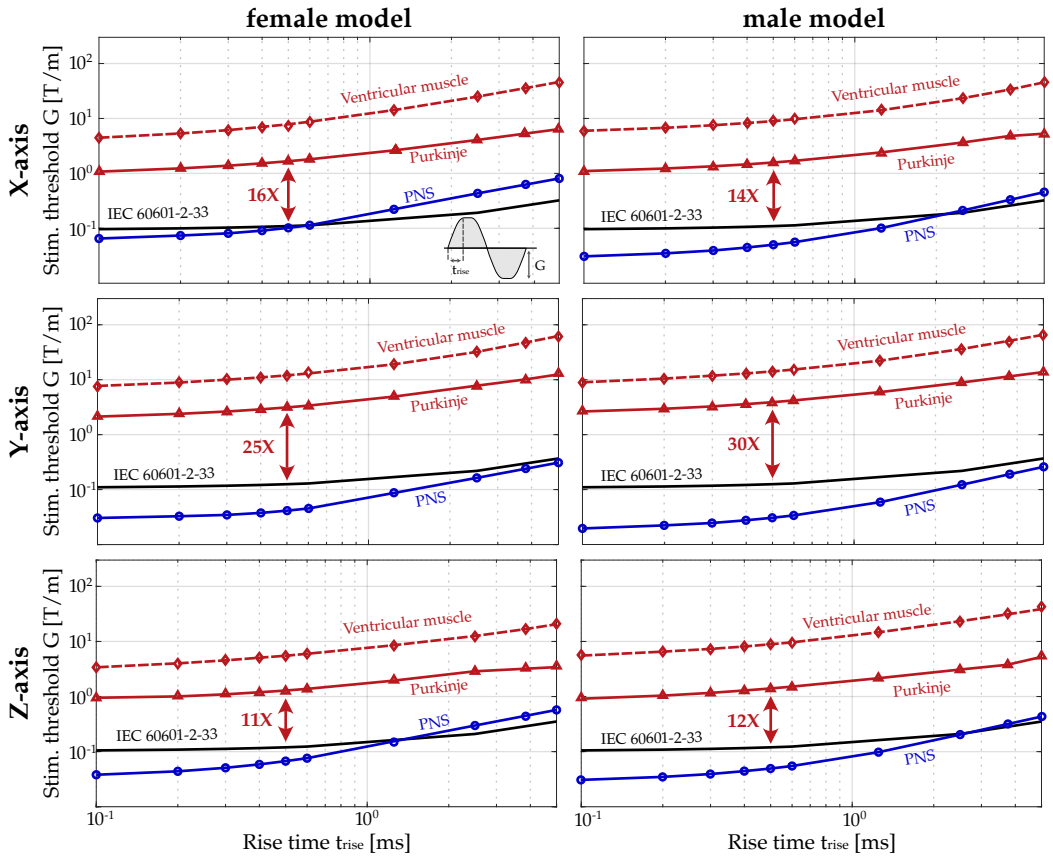

Figure 4.3: Stimulation thresholds of the Sonata gradient in terms of gradient amplitude G as a function of the rise time t_{rise} for a gradient waveform with sine-shaped ramps. Thresholds are plotted for all gradient axes (rows) and both human body models (columns). The CS thresholds are plotted in red (Purkinje fibers as solid lines, ventricular muscle fibers as dashed lines), simulated PNS thresholds are plotted in blue, IEC 60601-2-33 cardiac safety limits in black. The red arrows show the ratio between the IEC safety limit and the predicted Purkinje fiber stimulation thresholds at $t_{rise} = 0.5$ ms.

Purkinje fibers are shown by spheres, with larger diameters and brighter colors corresponding to lower thresholds. Stimulation approximately occurred in areas with high E-field magnitude along the fibers, whereas no stimulation occurred in areas with low E-field magnitudes. However, the stimulation location did not necessarily coincide with the highest E-field hotspot, as shown by the arrows. Figure 4.7 shows that instead, the simulated stimulation thresholds correlated significantly ($p < 0.05$) with the inverse of the maximum absolute value of the second spatial derivative of the electric potential d^2V/dr^2 along the Purkinje fiber paths (correlation coefficient ≈ 0.856). The inverse second spatial derivative of the electric potential along an excitable fiber is often referred to as the "activation function", and has previously been shown to correlate with stimulation thresholds of peripheral nerves (Rattay, 1986).

The impact of the Purkinje fiber paths on their stimulation threshold was assessed by generating four additional semi-random Purkinje networks for the female model using the rule-based modeling algorithm proposed by (Ijiri et al., 2008). The geom-

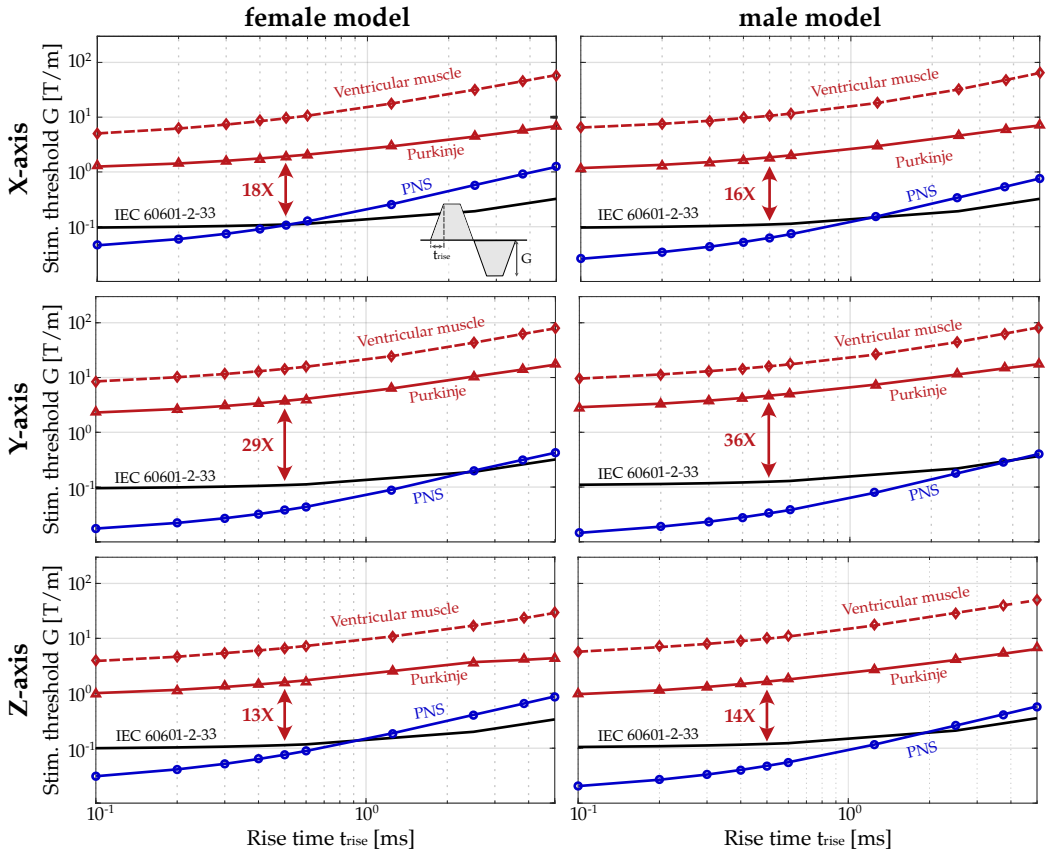

Figure 4.4: Stimulation thresholds of the Sonata gradient in terms of gradient amplitude G as a function of the rise time t_{rise} for a gradient waveform with linear ramps (trapezoidal waveform). The thresholds are plotted as in Figure 4.3. The trapezoidal gradient waveform led to overall higher stimulation thresholds than the sinusoidal waveform.

etry of the different networks, and hence the E-field projection onto the fiber paths, varied because the order in which the Purkinje fiber segments were iteratively grown as well as the distribution of angles between fiber segments was randomized, as described in Section 3.1.2. The largest threshold variation relative to the average CS threshold of all five Purkinje networks ranged between 15% at short rise times ($t_{rise} \leqslant 2.5$ ms) and 30% at $t_{rise} = 5.0$ ms (Figure 4.8). For all other simulations in the female model reported in this chapter, the Purkinje fiber network with the lowest thresholds (for $t_{rise} \leqslant 4.0$ ms) was chosen to obtain a conservative threshold estimate.

In addition to the stimulation threshold dependence on spatial E-field changes, the dependence on temporal characteristics of the stimulus waveform, and thus the induced E-field, was investigated. Figure 4.9 shows the relationship between the stimulation thresholds simulated in a Purkinje fiber and the plateau duration t_{plat}, or the number of bipolar pulses, respectively, of gradient waveforms with constant rise time $t_{rise} = 0.5$ ms. The total length of each simulated waveform varied depending on the plateau duration and on the number of pulses. Each waveform was thus applied at different times during the Purkinje pacemaking cycle (see Figure 3.5) to

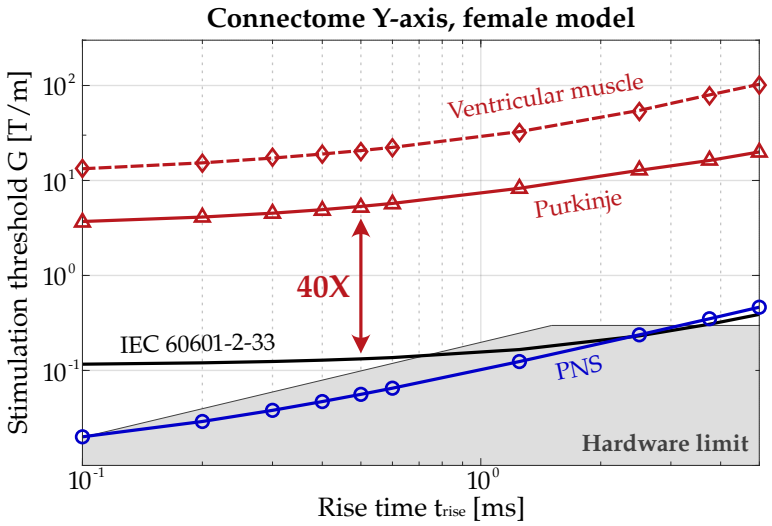

Figure 4.5: Stimulation thresholds of the Siemens Connectome Y-axis gradient coil in terms of gradient amplitude G as a function of the rise time t_{rise}. The CS thresholds (red) were simulated in the female body model with the head at isocenter for the same gradient waveform as in Figure 4.3. The PNS thresholds (blue) were previously measured in an experimental study in healthy volunteers for rise times between 0.1 ms and 0.8 ms (Setsompop et al., 2013), and were extrapolated linearly for higher rise times. The gray-shaded area indicates the hardware limit of the gradient system.

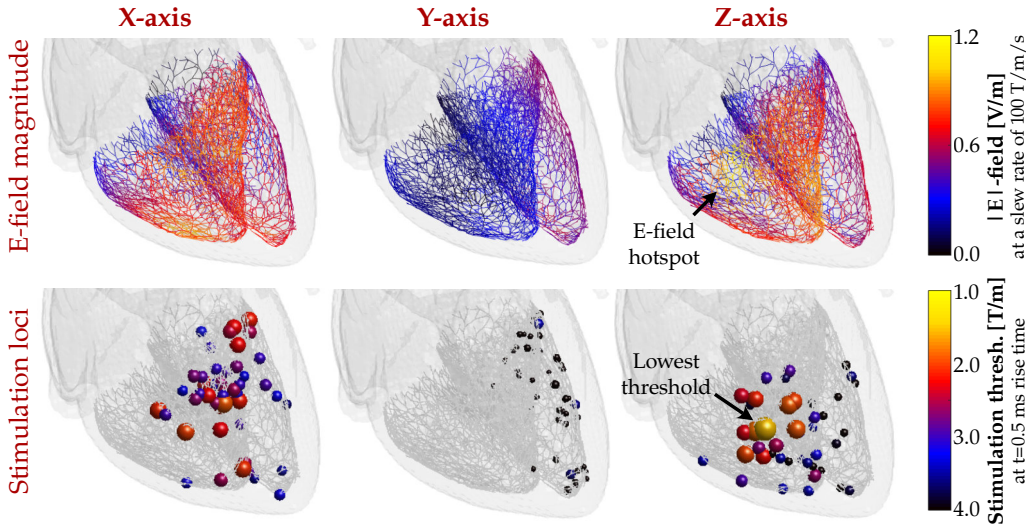

Figure 4.6: Top row: Electric field (E-field) magnitude sampled along the Purkinje fibers of the female body model for the three axes of the Sonata gradient. The E-field was scaled to an equivalent slew rate of 100 T/m/s. Bottom row: Stimulation loci of the Purkinje fibers. For better visibility, only the 50 most sensitive fibers in the Purkinje network are shown.

ensure the duration between the end of each waveform and the next pacemaking AP was constant for all waveforms. This was done to reduce the impact of the waveform length on the simulated CS threshold, since the Purkinje fiber model gets more

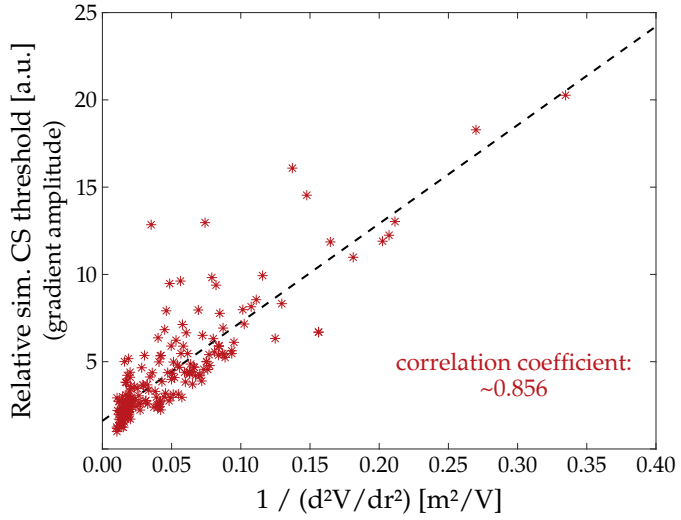

Figure 4.7: Stimulation thresholds of the Purkinje fibers as a function of the inverse second spatial derivative of the electric potential along the respective fiber path. The thresholds were simulated in the female body model placed in the Sonata Z-axis gradient coil for a gradient waveform with sine-shaped ramps and 0.5 ms rise time.

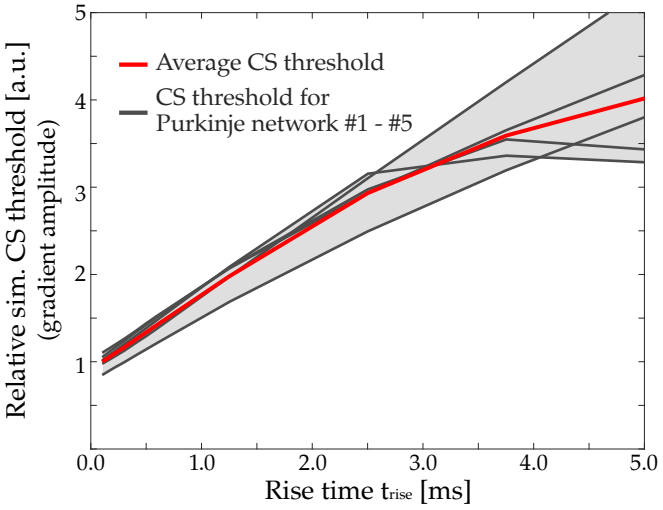

Figure 4.8: Relative CS gradient amplitude thresholds (female body model, Sonata gradient Z-axis coil) predicted for five different Purkinje fiber networks generated with the semi-random Purkinje modeling algorithm (Ijiri et al., 2008). Stimulation thresholds were predicted for a gradient waveform with sine-shaped ramps, two bipolar lobes, 500 µs plateau duration, and rise times between 0.1 ms and 5.0 ms.

sensitive to stimulation the closer the stimulus is applied before a pacemaking AP, as explained in Section 3.1.4. For $t_{plat} \leqslant 3.0$ ms, the simulated threshold decreased with increasing plateau duration, reaching a minimum of approximately 77% of the threshold simulated for a triangular gradient waveform with $t_{plat} = 0$ ms. For $t_{plat} > 3.0$ ms, the threshold increased slightly and reached an asymptotic value of approximately 80% relative to the threshold for a triangular waveform. At constant

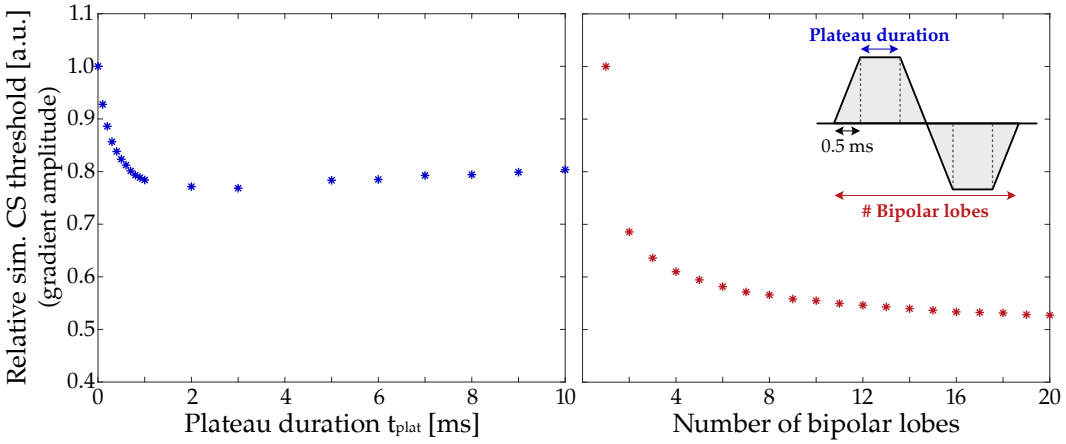

Figure 4.9: Impact of the plateau duration (left) and the number of bipolar pulses (right) of a gradient waveform with linear ramps and a 0.5-ms rise time on the stimulation threshold predicted for the Purkinje fiber network.

plateau duration, the simulated CS threshold decreased monotonically with increasing number of bipolar lobes in the gradient waveform. For around 20 bipolar lobes, the threshold reached an asymptotic value of around 50% relative to the threshold simulated for a single bipolar gradient field lobe.

4.1.3 *Predicted electric field strength-duration curves*

As explained in Section 2.3.3, stimulation properties of excitable tissues are often expressed in the form of E-field strength-duration curves. Figure 4.10a shows strength-duration fit curves for the maximum E-field amplitude simulated along the most sensitive cardiac fibers in the male and female body models. The E-fields were evaluated for the Sonata gradient's X-, Y-, and Z-axis coils for varying durations of a rectangular E-field pulse and scaled to the respective stimulation thresholds, as described in Section 3.1.6. The hyperbolic strength-duration expression (Lapicque, 1909) described the simulated threshold E-field amplitudes better (RMSE $= 0.9 \pm 1.1$ V/m) than the exponential expression (Blair, 1932) (RMSE $= 2.9 \pm 1.2$ V/m).

Figure 4.10b shows the exponential and hyperbolic strength-duration fit parameters as mean $\pm$ standard deviation for all axes of the Sonata gradient and the male and female body models. The average rheobase was $E_{rheo,exp} = 24.3 \pm 1.6$ V/m for the exponential fit and $E_{rheo,hyp} = 18.7 \pm 1.4$ V/m for the hyperbolic fit. The average exponential time constant was $t_c = 1.1 \pm 0.2$ ms, and the hyperbolic time constant, i. e., the chronaxie, was $t_{chron} = 1.4 \pm 0.3$ ms.

4.1.4 *Preliminary validation in canine models*

The simulated B-field efficiency of the solenoid coil (SOL) used in one of the previous canine studies (Nyenhuis et al., 1992) was $\epsilon_B \approx 100$ µT/A at the center of the coil, which is in agreement with previous simulations of this experimental setup (Mouchawar et al., 1993). In this study, a capacitor was discharged into the coil

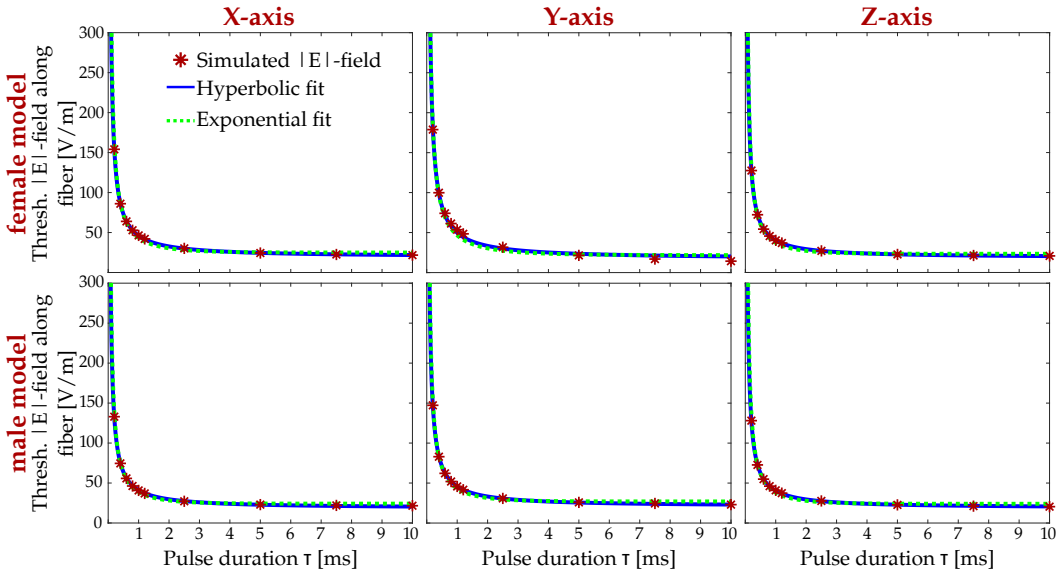

(a) Simulated threshold electric field magnitude |E| sampled along the most sensitive cardiac Purkinje fiber as a function of the pulse duration τ. Simulations were done for the male and female body models (rows) and the three axes of the Sonata gradient (columns). The simulated data points were fitted with the hyperbolic (Lapicque, 1909) (solid blue curve) and the exponential strength-duration curve (Blair, 1932) (dashed green curve).

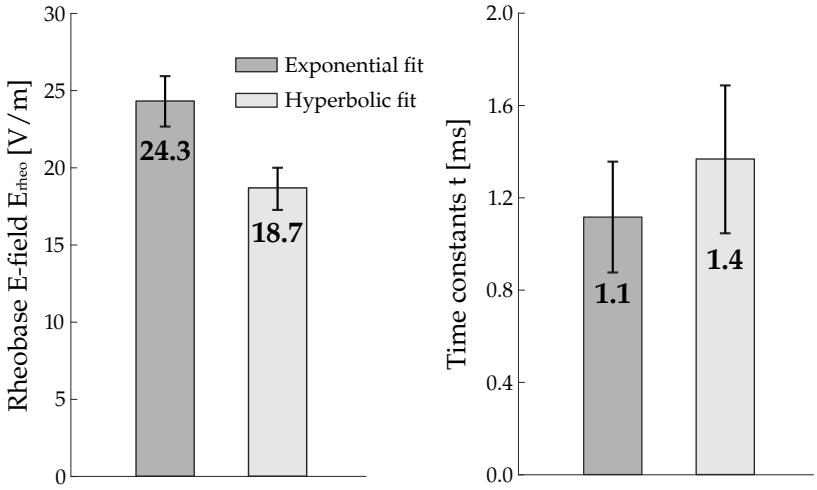

(b) Electric field rheobase (left graph) and time constants (right graph) obtained from the exponential and hyperbolic strength-duration fit curves shown in (a). The fit results are given in terms of mean ± standard deviation of all six simulations.

Figure 4.10: Simulated electric field strength duration curves and mean rheobase and time constant fit parameters. The simulations were done for the male and female body models placed with the head at isocenter in the three axes of the Sonata gradient.

(C = 820 µF, R = 199 mΩ, L = 187 µH (Nyenhuis et al., 1992)) to create EMPs to measure cardiac magnetostimulation in the canines. The maximum B-field amplitude at coil center for this RLC circuit was ca. 1.5 T, and the maximum dB/dt was ca. 5.2 kT/s (Bourland et al., 1991). The simulated efficiency of the pair of coplanar spiral coils (COP) used in another experimental study in canines (Mouchawar et al., 1992) was $\epsilon_B \approx 345$ µT/A at the center of each coil, which is also in agreement with previous simulations (Mouchawar et al., 1993). This study also used an RLC circuit for cardiac excitation (C = 680 µF, R = 120 mΩ, L = 220 µH (Mouchawar et al., 1992)), resulting in a maximum B-field amplitude of 5.9 T, and a maximum dB/dt of ca. 17.5 kT/s.

Figure 4.11a shows the E-field simulated in the computational model of a 17-kg canine for the two coil configurations COP and SOL from the previous experiments (Mouchawar et al., 1992; Nyenhuis et al., 1992). At dB/dt = 1.0 kT/s at coil center, the average 95th percentile E-field amplitude in the canine myocardium was 6.5 ± 0.6 V/m for COP, and 20.3 ± 1.5 V/m for SOL (mean ± standard deviation for the respective canine models with different sizes and weights). Figure 4.11b shows the simulated and experimental canine CS thresholds in terms of dB/dt for the damped sinusoidal B-field waveform used in the respective experiment. The Purkinje fibers of the canine models were ca. six-fold more sensitive to stimulation than the ventricular fibers, and hence set the effective threshold. For COP, the average simulated threshold matched the experimental threshold within 2%. For SOL, the average simulated threshold was ca. 28% higher than the experimental threshold. Furthermore, the simulated thresholds for SOL had a larger variation than for COP, with higher thresholds for smaller canine body model weights.

4.2 MEASUREMENT OF PORCINE CARDIAC MAGNETOSTIMULATION

4.2.1 *Selection of a coil-amplifier combination*

Figure 4.12 shows E-fields induced by the TMS coil, the pair of coplanar coils, the solenoid coil, and the curved and flat spiral coils in the IT'IS porcine body model. The simulations shown here were done for the candidate coil designs shown in Figure 3.8. All E-fields were scaled to match a discharge of a 680-µF capacitor at a charging voltage of U = 10.0 kV. The capacitance and charging voltage were prescribed to match the values of a canine experimental study (Mouchawar et al., 1992).

Table 4.1 compares the 95th percentile E-field (E_{95}) induced in the heart of the IT'IS porcine model by the subset of investigated coil designs shown in Figure 4.12. The E-field was scaled according to Equation 3.15 to match the maximum charging voltage of a TMS amplifier, a gradient power amplifier (GPA), and a 680-µF capacitor. Details of these amplifier systems can be found in Section 3.2.1. The TMS amplifier is only compatible with coil inductances $\leqslant$ 18 µH, and was thus only simulated in combination with the TMS coil. The GPA had a five-fold lower U_{max} than the capacitor, and correspondingly induced five-fold lower E-field amplitudes in the porcine heart.

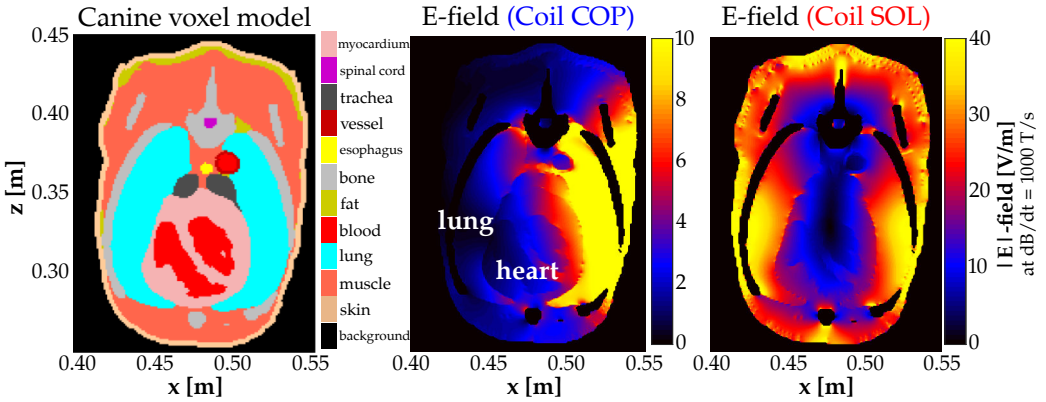

(a) Axial slices of the voxel model of a 17-kg canine and the simulated electric field (E-field) induced by the coplanar coils (COP) and the solenoid coil (SOL) at a peak magnetic field switching rate of $dB/dt = 1000$ T/s at the coil center. The E-field in the bones was set to zero for better visibility. Note the different scaling of the color bar for the E-field maps. The figure is taken from (Klein et al., 2021).

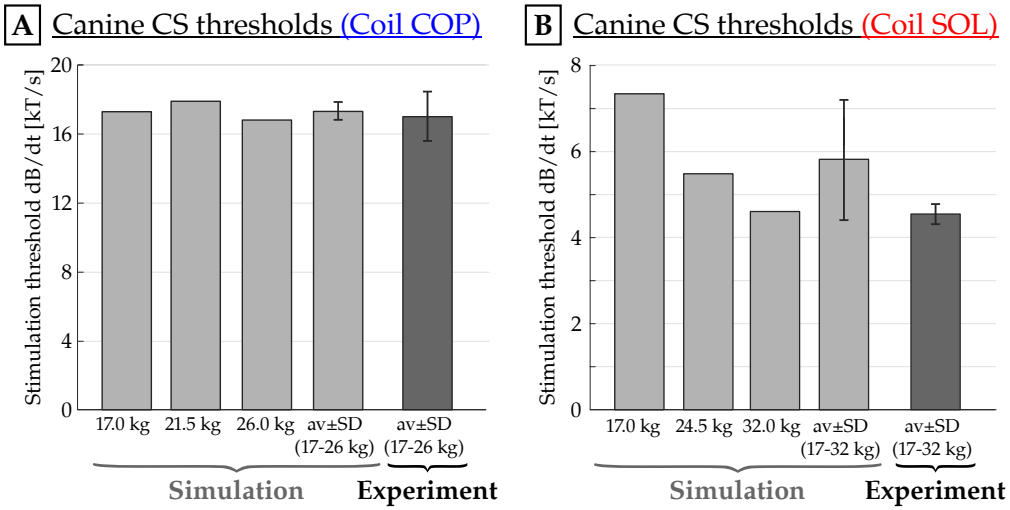

(b) Simulated and experimental (Mouchawar et al., 1992; Nyenhuis et al., 1992) CS thresholds of the canines for the pair of coplanar coils (COP) and the solenoid coil (SOL) in terms of peak dB/dt amplitude at the coil center. All thresholds are given for a damped sinusoidal B-field waveform. The simulated thresholds correspond to the Purkinje fiber thresholds, which were ca. six-fold lower than the ventricular muscle fiber thresholds.

Figure 4.11: Electric fields and cardiac stimulation (CS) thresholds simulated in canine body models of varying sizes and weights for two coils used in previous experimental studies (Mouchawar et al., 1992; Nyenhuis et al., 1992).

The combination of the TMS coil and the 680-µF capacitor led to the highest cardiac E-field. However, the resonance frequency f_{res} of the capacitor-coil system is inductance-dependent:

$$f_{res} = \frac{1}{2\pi\sqrt{LC}}, \tag{4.1}$$

where C is the capacitance and L is the inductance. For the low-inductance TMS coil, the resonance frequency is $f_{res} \approx 1840$ Hz, and thus substantially higher than for the other coil designs ($f_{res} \leqslant 450$ Hz). According to the strengh-duration curve

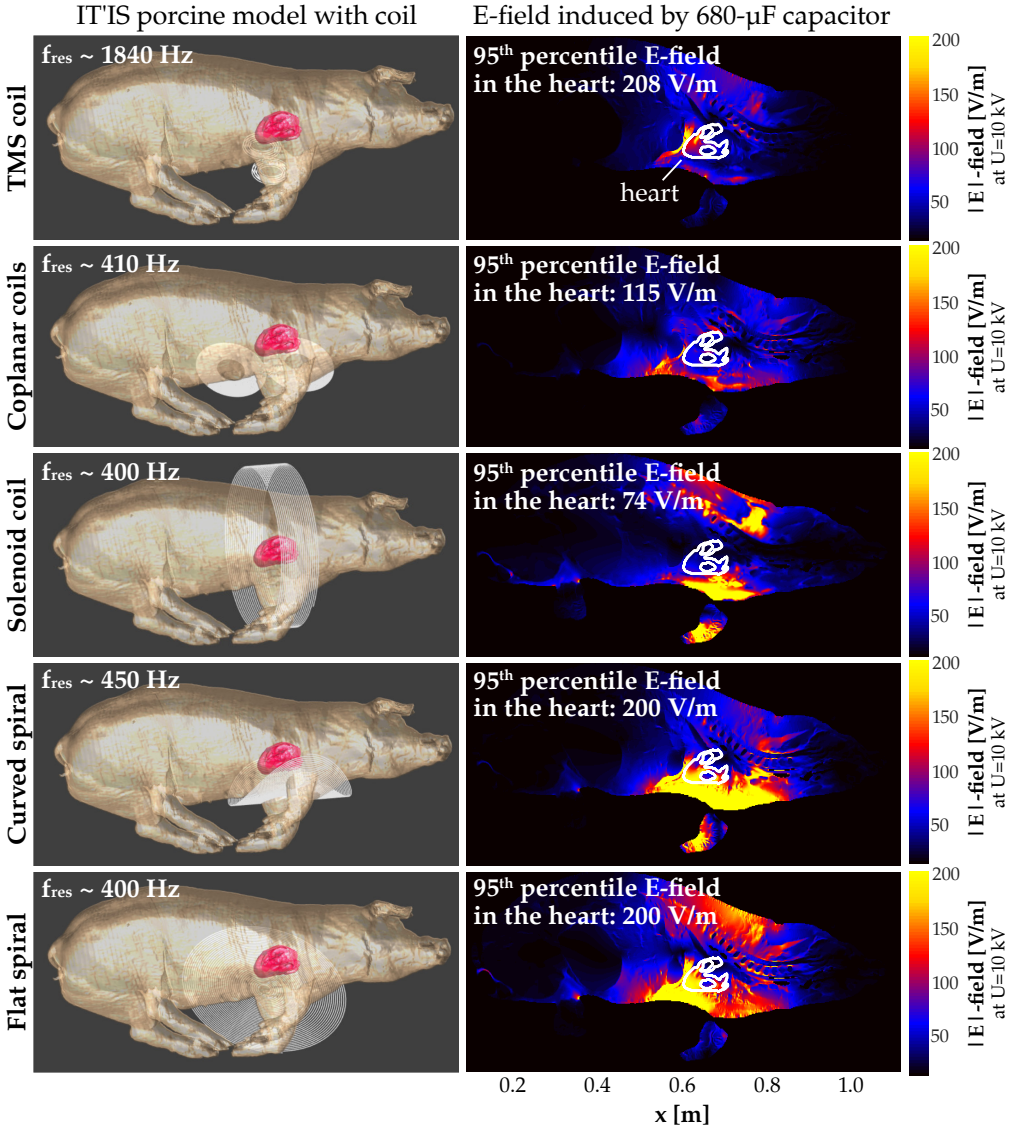

Figure 4.12: Sagittal slices of the simulated electric fields induced in the IT'IS porcine body model by five candidate coil designs for discharges of a 680-µF capacitor at a charging voltage of $U = 10.0$ kV. The resonance frequency f_{res} of the RLC circuits formed by the capacitor-coil systems varied depending on the respective coil inductance.

Table 4.1: Simulated electric fields induced in the heart of the IT'IS porcine body model by the candidate coil designs shown in Figure 4.12. The electric field of each coil was scaled to the maximum charging voltage U_{max} of three amplifiers described in Section 3.2.1.

	95^{th} percentile E-field in the heart [V/m]		
Coil design and inductance	TMS amplifier ($U_{max} = 1.8$ kV)	GPA ($U_{max} = 2.0$ kV)	680-µF capacitor ($U_{max} = 10.0$ kV)
TMS (11 µH)	37	42	208
Coplanar coil pair (220 µH)	–	23	115
Solenoid (230 µH)	–	15	74
Curved spiral (180 µH)	–	40	200
Flat spiral (230 µH)	–	40	200

formalism (Equation 3.10 and Equation 3.11), the E-field required for cardiac stimulation is greater at higher frequencies than at lower frequencies (the frequency is inversely proportional to the pulse duration). The E-fields induced by the spiral coils thus have a higher possibility of reaching the CS threshold than the TMS coil system, considering their lower resonance frequency.

Simple EM modeling of the canine study conducted using the coplanar coil pair estimated that an E-field amplitude of ca. 90-100 V/m was needed to cause an ectopic beat in the canine heart (Mouchawar et al., 1992; Ragan et al., 1995). This study was conducted at $f_{res} \approx 450$ Hz. The E-fields simulated for the spiral coils in the IT'IS model's heart were thus well above the CS threshold measured in canines. The flat spiral coil design ($D_{out} = 40$ cm, $D_{in} = 2.5$ cm, 38 turns) is easier to build and handle than the curved coil design, which requires fitting the animal's leg into the inner coil opening. The flat spiral coil design in combination with a large capacitor was thus chosen for the experimental study of magnetostimulation in the porcine heart.

4.2.2 *Design and construction of a magnetic stimulator*

Based on the preliminary E-field calculations in the IT'IS porcine model described in the previous section, a magnetic stimulator was constructed that consisted of a capacitor bank and a flat spiral coil. Figure 4.13 shows photographs of the device. At a basic level, the stimulator can be described by an RLC circuit similar to the ones that have previously been used in the canine experimental studies (Mouchawar et al., 1992; Yamaguchi et al., 1991). Four 55-µF capacitors (High Voltage Products, Martinsried, Munich, Germany) were connected in parallel to reach a theoretical total capacitance of C=220 µF. The measured total capacitance was 210 µF. The capacitors were rated for a maximum charging voltage of $U_{max} = 18.0$ kV and charged through a diode by a high-voltage DC power supply (TDK-Lambda, Tokyo, Japan). The duration of the charging process depended on the charging voltage, and took up to two minutes at U_{max}. A high-voltage relay (Ross Engineering, Campbell, CA USA) was used to close the circuit, upon which the charge dispersed into the coil.

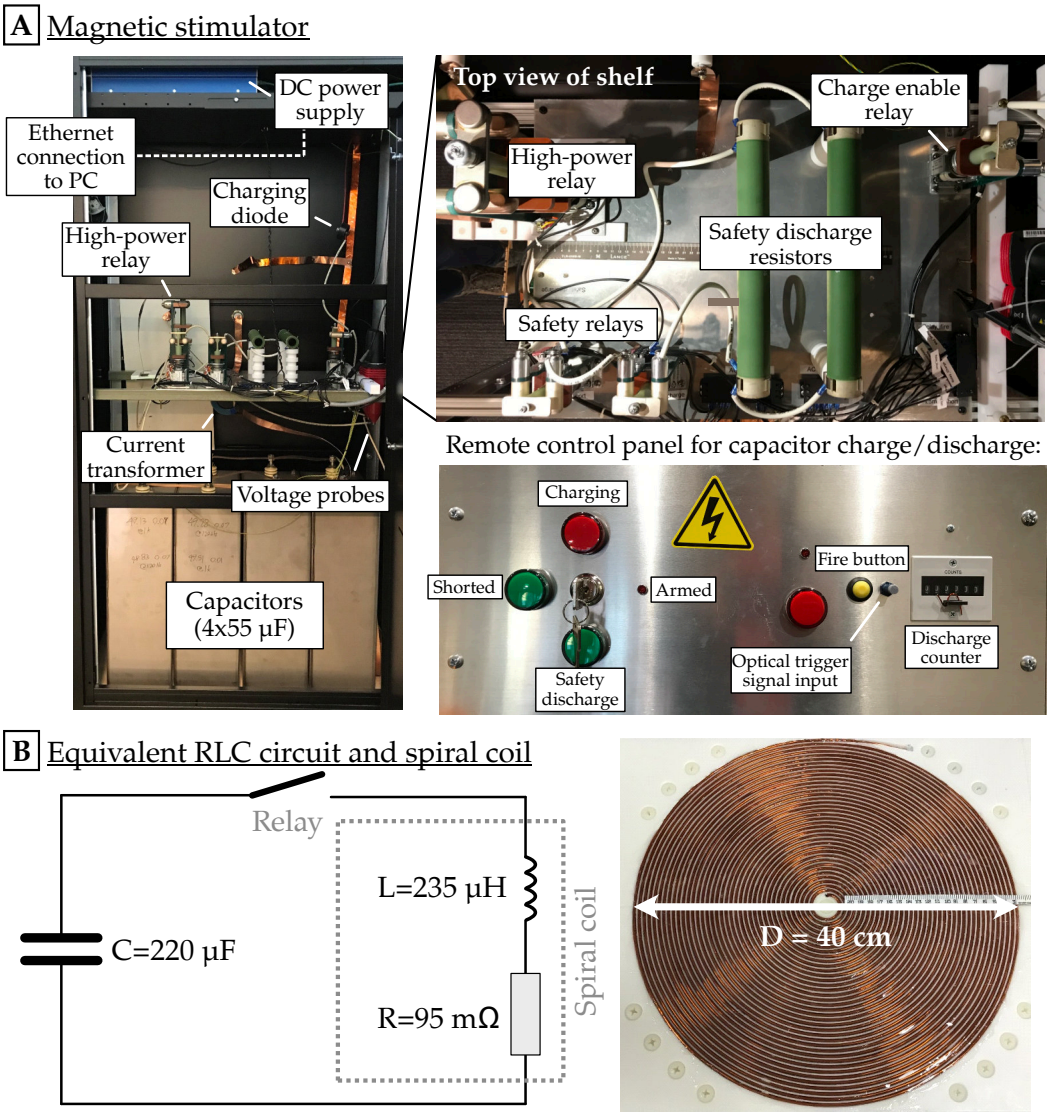

Figure 4.13: (A) Magnetic stimulator: Four capacitors were connected in parallel and charged by a DC power supply up to a maximum charging voltage of $U_{max} = 18$ kV via a diode. Upon the closing of a relay, the capacitors were discharged into a coil. Current and voltage were measured and recorded with an oscilloscope for each discharge. Additional safety circuits and a remote control panel assured safe handling of the stimulator. (B) The stimulator can be represented as a simple RLC circuit containing the capacitors, the relay as a switch, and the coil. The coil is a flat spiral design with 38 turns of copper wire, an outer diameter of 40 cm and an inner diameter of 2.5 cm. The figure is taken from (Klein et al., 2022).

Closing of the relay was triggered by the simultaneous occurrence of two events: 1) a manual button press that armed the system, and 2) an optical signal triggered off the R-wave on the ECG trace with a programmable delay. The current waveform in the coil was a damped sinusoid, as described by Equation 3.12. At the maximum charging voltage U_{max}, the system reached a maximum current amplitude of $I_{max} = 15.9$ kA with a resonance frequency of $f_{res} \approx 715$ Hz. The effective stimulus duration of this waveform according to the IEC 60601-2-33 definition (IEC, 2010) is $t_{s,eff} \approx 0.45$ ms. For each discharge, the serial current and voltage across the capacitors was captured with an oscilloscope (Tektronix, Beaverton, OR, USA) connected to a voltage probe and a current transformer. Because of the large energy stored in the capacitors, safety circuits consisting of additional relays and high-energy resistors were included in the stimulator. The safety circuits allowed disconnecting the power supply, safely discharging the capacitors in case of an aborted stimulation attempt, and shorting the capacitors to prevent self-charging through dielectric absorption. As an additional precaution, the capacitor and discharge system were housed in a grounded conductive cabinet, and the distance between this system and the control computer and operator station was kept around 10 m.

The capacitors were discharged into a flat spiral coil with an outer diameter of 40 cm, and an inner diameter of 2.5 cm (Figure 4.13). The coil consisted of 38 turns of 2.3-mm (11 AWG) copper magnet wire, i. e., a wire coated with a thin insulation. The wire was wound in two layers connected in parallel to decrease resistance and thus mitigate heating by the high-amplitude current pulses. The wire was hammered into grooves machined into a 0.5-inch ABS sheet reinforced with a 0.5-inch fiberglass sheet on the back for added strength. The coil was covered with fiberglass cloth and epoxy resin. It was connected to the pulse generator system with two 40 kV-rated 8-AWG cables, and a set of SB135/HB135 connectors (GES High Voltage GmbH, Hallbergmoos, Germany). During the stimulation experiments, the coil was attached below the fiberglass table on which the animals were placed, and visually centered below the heart.

4.2.3 *Magnetic field measurements of the experimental setup*

Figure 4.14a shows B-field profiles of the spiral coil. The B-field was measured with a THM-1176 Hall sensor (Metrolab Technology SA, Geneva, Switzerland) at a DC coil current of 10 A, shown in red. Superimposed in blue are the B-field profiles of the coil calculated using Bio-Savart's law. These calculations were done for a total inductance and AC resistance of $L = 235$ µH and $R = 95$ mΩ, i. e., combined series resistance and inductance of the coil, connecting cables, and pulse generator. These values were chosen to achieve the best fit between the calculated and measured B-fields. The B-field efficiency at the coil center was $B_{eff} = 350$ µT/A, equivalent to a maximum B-field of $B_{max} = 5.6$ T for a maximum current $I_{max} = 15.9$ kA.

Figure 4.14b shows dB/dt waveforms resulting from capacitor discharges, which were measured with a pick-up coil consisting of 3 turns of copper wire with 15 mm diameter. The pick-up coil was placed 17 cm above the center of the spiral coil and connected to an oscilloscope. The experimental setup, i. e., the capacitor and spiral coil, generated a maximum B-field switching rate $dB/dt_{max} = 26.7$ kT/s at the coil

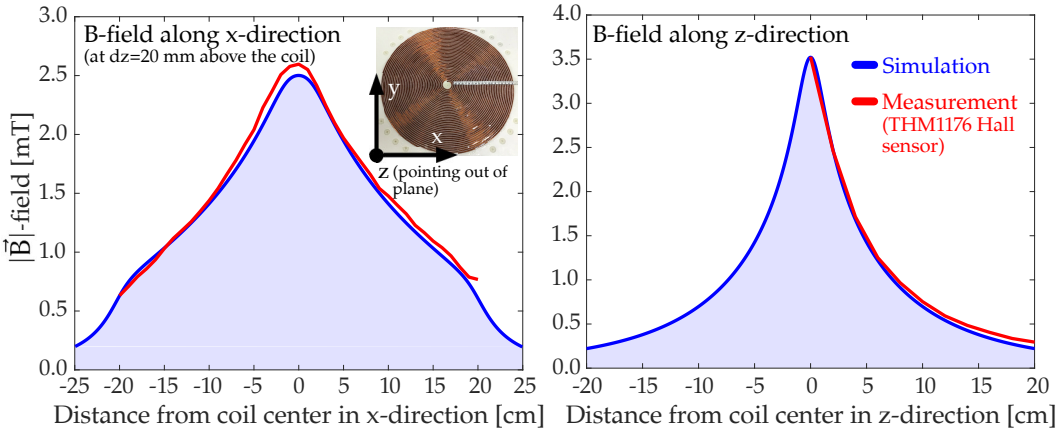

(a) Magnetic field amplitudes created by the spiral coil at a DC current of I = 10 A. The magnetic field was measured and simulated as a function of position across the coil surface (at 20 mm distance from the coil, left), and as a function of the vertical distance from the coil center (right).

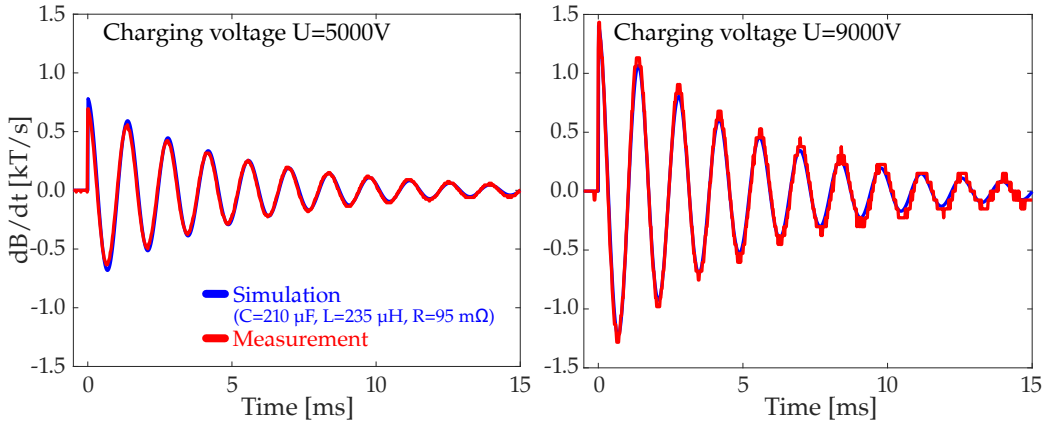

(b) Magnetic field rate (dB/dt) waveforms resulting from capacitor discharges at charging voltages of U = 5.0 kV and U = 9.0 kV. Measurements and simulations were done at 17 cm above the coil center.

Figure 4.14: Magnetic field (a) and dB/dt (b) measurements (red curves) and simulations (blue curves) for the flat spiral coil constructed for the porcine experimental study. Both figures are taken from (Klein et al., 2022).

center. The maximum B-field rate was ca. 4.6 kT/s at a vertical distance of 11 cm above the coil center, which was the approximate depth of the heart in the pigs.

4.2.4 *Effects of electromagnetic pulses on the porcine heart*

A total of 219 measurements were obtained with different charging voltages and at different cardiac phases. One of the pigs (#8) moved excessively during four of the measurements due to insufficient muscle paralysis, which caused artifacts on the ECG and hemodynamic traces. These measurements were flagged as "non-evaluable" and excluded from further analysis, i. e., data points obtained in these measurements were not included in the sigmoid fits that were done to determine the porcine CS threshold. In 72 of the remaining measurements, only blood pres-

sure and oximetry traces, i. e., no ECG, were recorded, either because no ECG leads were connected during the capacitor discharges in the first three pigs, or because the ECG measurement was corrupted by the high voltages induced in the leads during discharge. These 72 measurements without ECG traces were divided into three groups: 1) Clear CS visible on both the blood pressure and oximetry trace, 2) clear lack of CS on both traces, and 3) indeterminate result due to conflicting or artifact-dominated data in the traces. The last category comprised 35 measurements that were excluded from further analysis. This resulted in a total of 180 measurements that were analyzed for effects that the EMP had on the porcine heart, with a median of 17 measurements per pig (minimum: 6, maximum: 31).

The effects observed in these 180 measurements can be categorized into four groups:

i. No stimulation
ii. Cardiac capture followed by a compensatory pause
iii. Cardiac capture without a compensatory pause
iv. Cardiac capture followed by a premature ventricular contraction (PVC)

Cardiac capture means that the EMP depolarized the myocardium producing a waveform on the ECG and/or hemodynamic effects consistent with contraction, comparable to a heartbeat induced by an extrinsic cardiac pacemaker. In a PVC, the ventricles are stimulated prematurely at an ectopic intrinsic pacing site, depolarizing them before the atria. Examples for each stimulation effect are shown in Figure 4.15, Figure 4.16, and Figure 4.17.

Figure 4.15 shows ECG, blood pressure and oximetry recordings in pig #6 (male, 30 kg) for capacitor charging voltages of 5.0 kV (A) and 5.25 kV (B). The EMP was applied right after the T-wave ($t = 0$ s, early diastole). All traces show some artifacts during and after application of the pulse, indicated by gray-shaded boxes. These artifacts were likely caused by EM interference of the strong time-varying B-field with the physiological recording equipment, and by residual muscle contractions due to incomplete vecuronium-induced skeletal muscle paralysis. The effects of skeletal muscle contractions were especially visible in the blood pressure signal due to the sensitivity of the piezo-electric transducer to motion. The severity of the artifacts depended on the charging voltage and on the time passed since the last vecuronium injection. In Figure 4.15 (A), the first heartbeat after the EMP looked normal on all traces. The RR interval before and after the pulse remained constant at 546 ± 5 ms (averaged over five intervals), indicating that, in this case, the 5.0-kV pulse was sub-threshold. Figure 4.15 (B) shows recordings in the same pig at a charging voltage of 5.25 kV. In this case, the ECG showed a premature T-wave after the EMP, followed by the absence of an anterograde QRS complex at the native RR interval. The RR interval between the QRS complexes before and after stimulation was 1157 ms, compared to an average interval of 569 ± 5 ms before stimulation. This long cycle length caused an increased blood pressure peak after the EMP. In this case, the 5.25-kV pulse caused cardiac capture followed by a compensatory pause.

Figure 4.16 shows measurements in pig #5 (male, 21 kg) for charging voltages of 5.0 kV (A, sub-threshold) and 6.0 kV (B, supra-threshold). In this measurement,

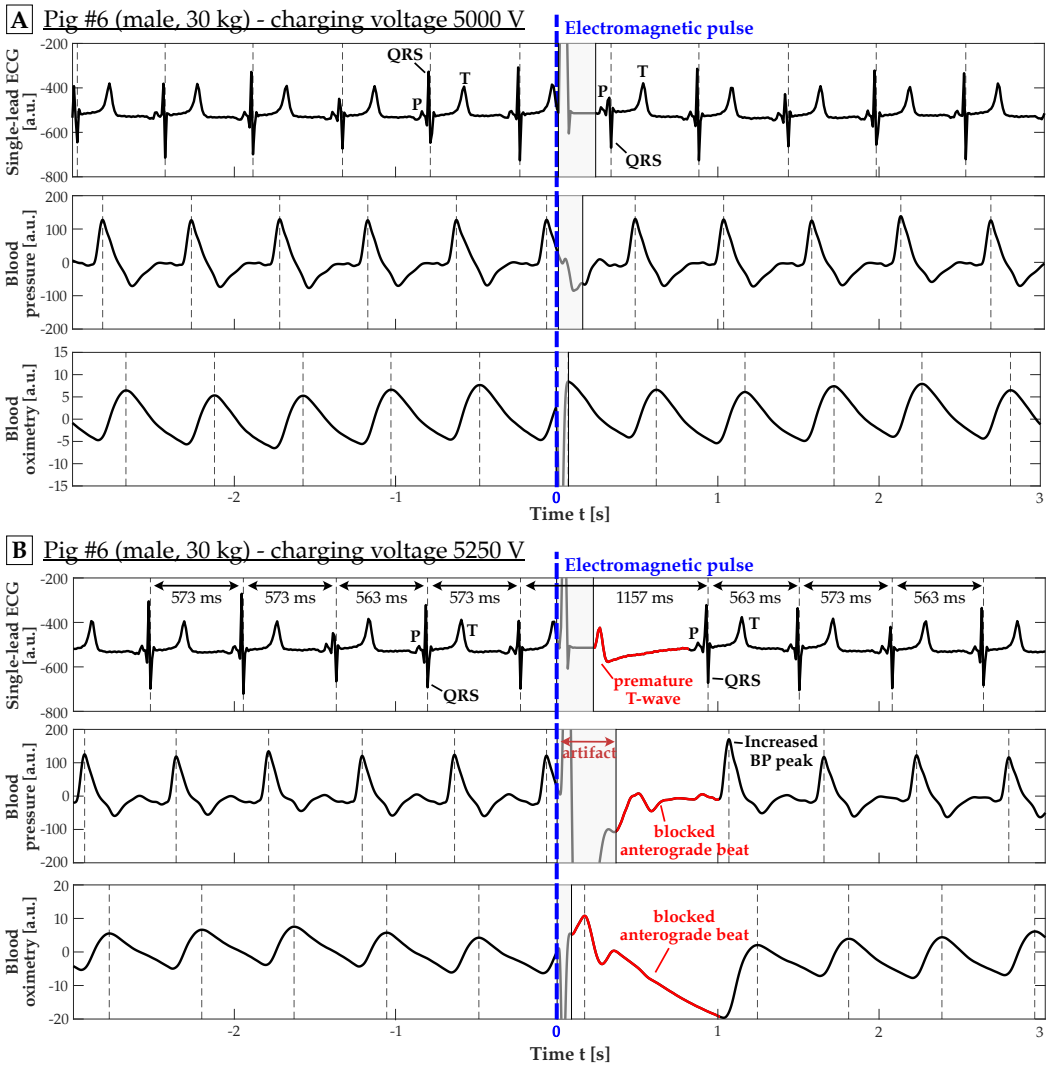

Figure 4.15: Single-lead ECG, blood pressure, and blood oximetry traces for pig #6 measured before, during and after capacitor discharges at charging voltages of (A) 5.0 kV (sub-threshold) and (B) 5.25 kV (supra-threshold), respectively. The electromagnetic pulse (EMP) was applied on the downslope of the T-wave during early diastole (dashed blue line, $t = 0$ s). The gray-shaded area after the pulse shows the duration during which the signals suffered from artifacts caused by electromagnetic interference with the measurement device and by skeletal muscle contractions. (A) The heartbeats after the EMP had a normal morphology and timing, indicating that cardiac stimulation was not achieved. (B) Anomalies in the physiological traces following the EMP are shown in red. The 5.25-kV pulse caused cardiac capture, as indicated by the premature T-wave on the ECG, the absence of an anterograde QRS complex at the native RR interval, and a long cycle length (compensatory pause) following the pulse. Normal anterograde conduction resumed in the beat following capture. The longer cycle length of the captured beat resulted in an increase in blood pressure in the subsequent beat. The figure is taken from (Klein et al., 2022).

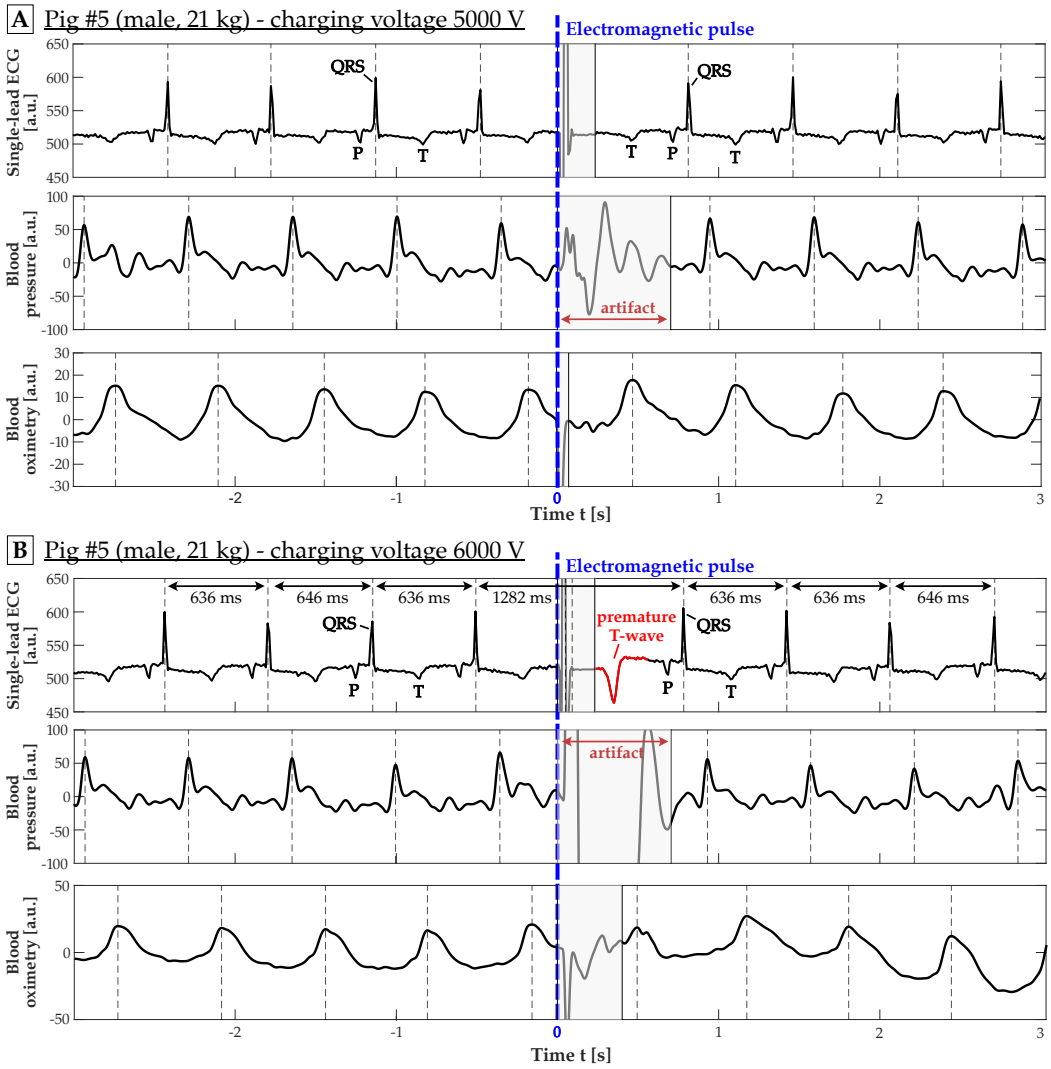

Figure 4.16: Single-lead ECG, non-invasive blood pressure, and blood oximetry traces measured in pig #5 before, during and after capacitor discharges at charging voltages of (A) 5.0 kV (sub-threshold) and (B) 6.0 kV (supra-threshold), respectively. The electromagnetic pulse (EMP) was applied right before the P-wave (late diastole). The native QRS complex in panel (A) is hidden by the artifact generated by the EMP (gray box) but occurs close to the native RR interval. The T-wave morphology and TT interval are unchanged, consistent with a lack of capture. The ECG signal in (B) shows a premature T-wave with altered morphology after the EMP, after which normal anterograde conduction was resumed. In this case, the EMP caused cardiac capture without a significant compensatory pause. The figure is taken from (Klein et al., 2022).

the EMP was applied during late ventricular diastole, right before the P-wave. The supra-threshold pulse caused a premature high-amplitude T-wave (B), indicating cardiac capture. In this case, there was no significant compensatory pause before normal anterograde conduction resumed. The inverted (negative) T- and P-waves in the ECG measurements in Figure 4.16 were caused by an inverted attachment of the ECG leads to the porcine torso, and are not indicative of an underlying pathology.

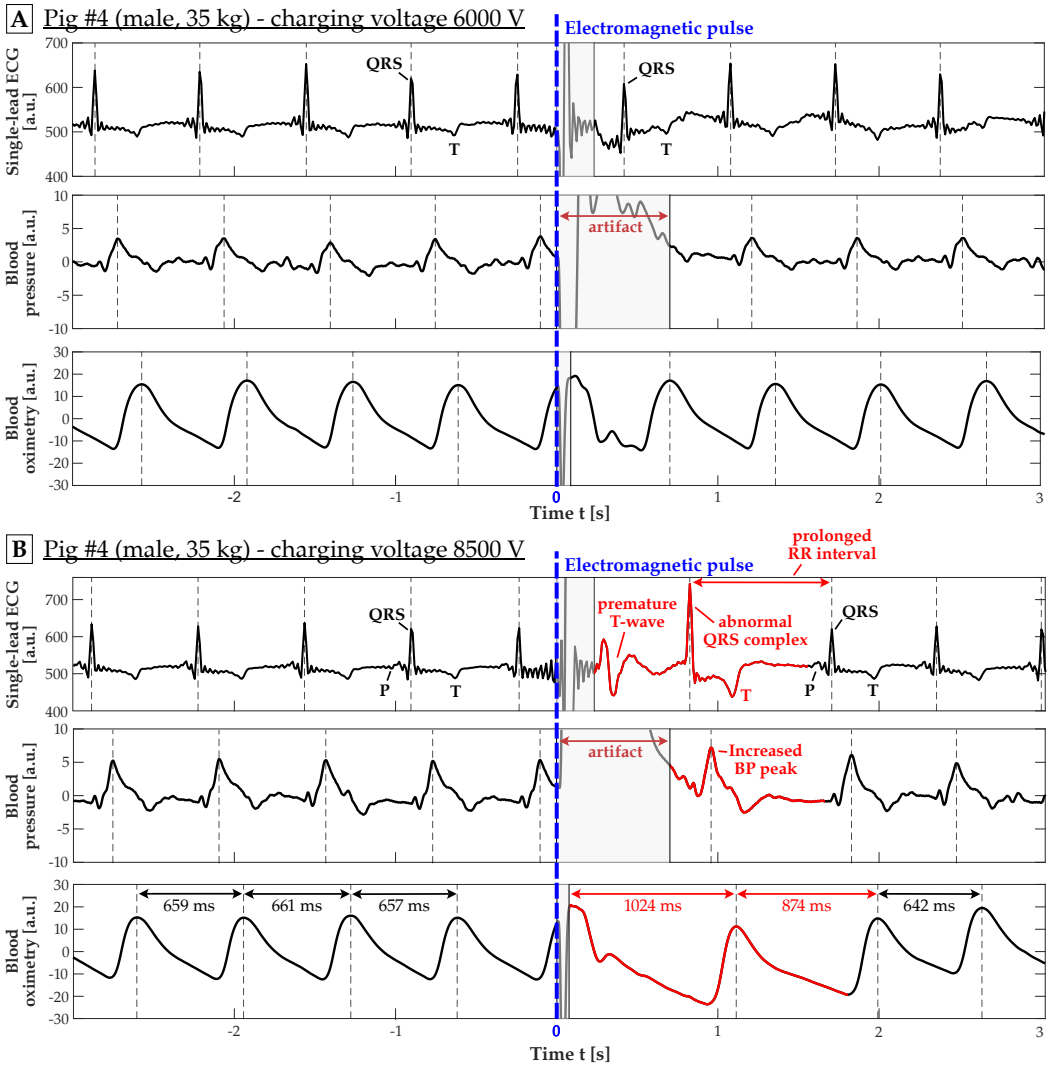

Figure 4.17: Single-lead ECG, non-invasive blood pressure, and blood oximetry traces for pig #4 measured before, during and after capacitor discharges at charging voltages of 6.0 kV (sub-threshold) (A) and 8.5 kV (supra-threshold) (B), respectively. The electromagnetic pulse (EMP) was applied on the T-wave (early diastole). The ECG trace in (B) shows a premature T-wave with altered morphology after the EMP, followed by a compensatory pause before the next QRS complex, which exhibited an abnormal morphology. This QRS complex was followed by a second, slightly shorter compensatory pause before normal anterograde conduction was resumed. In this case, the EMP caused cardiac capture followed by a single premature ventricular contraction. The figure is taken from (Klein et al., 2022).

Figure 4.17 shows measurements in pig #4 (male, 35 kg) for charging voltages of 6.0 kV (A, sub-threshold) and 8.5 kV (B, supra-threshold). The ECG signal was noisy in this measurement, most likely due to poor contact between the electrode and the pig's skin. The signal was thus filtered with a 750-Hz low-pass filter to make the T-wave visible. The EMP in Figure 4.17 (B) caused cardiac capture, as indicated by the premature T-wave after the pulse. This T-wave was followed by a compensatory

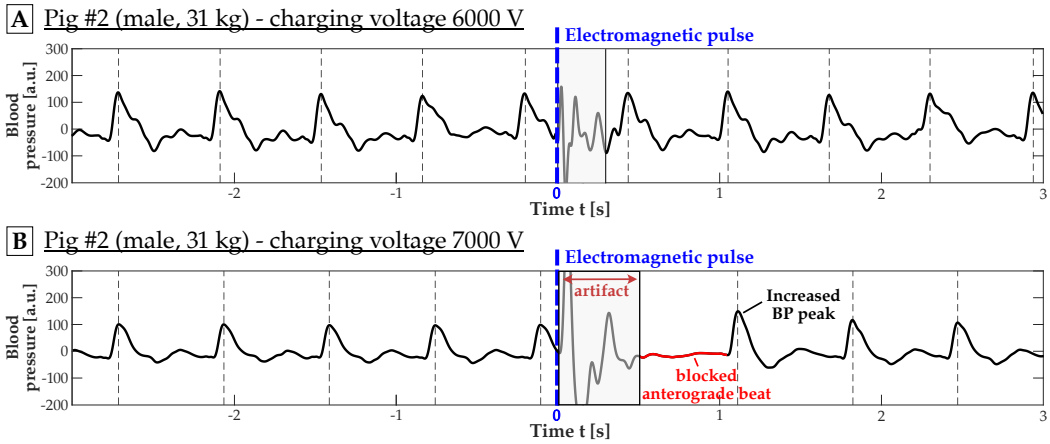

Figure 4.18: Non-invasive blood pressure traces measured in pig #2 before, during and after capacitor discharge at a charging voltage of (A) 6.0 kV (sub-threshold) and (B) 7.0 kV (supra-threshold), respectively. The electromagnetic pulse (EMP) was applied ca. 200 ms after the blood pressure peak, which in this case corresponded to the early ventricular diastolic phase. The signal in (B) shows a blocked anterograde heartbeat after the EMP and an elevated pressure peak in the first heartbeat following stimulation. This is suggestive of capture with a compensatory pause. The figure is taken from (Klein et al., 2022).

pause of 1024 ms before the next QRS complex, which was characterized by elevated R-wave and T-wave amplitudes compared to the previous heartbeats. This abnormal QRS complex was followed by a second compensatory pause (874 ms) before normal anterograde conduction resumed with an average 659 ± 4 ms RR interval. This recording is consistent with cardiac capture followed by a PVC.

For the measurements during which no ECG recordings were obtained, it was not possible to clearly distinguish between the stimulation effects ii, iii, and iv. However, hemodynamic traces that were not corrupted by artifacts still allowed to detect events with (ii, iii, or iv) and without (i) cardiac capture. Figure 4.18 shows one of these measurements in pig #2. At a charging voltage of 7.0 kV (B), cardiac capture was clearly visible on the blood pressure trace as a blocked anterograde beat, and an increase in pressure in the first beat after stimulation.

4.2.5 *Measured cardiac magnetostimulation thresholds*

Cardiac magnetostimulation thresholds were determined by fitting sigmoid functions (Equation 3.16) to the binary cardiac response, i. e., capture or no capture, to the EM pulses. Figure 4.19a shows single and average sigmoid fits for stimulation during early ventricular diastole (right after the T-wave), while Figure 4.19b shows the same results for stimulation during late diastole (right before the P-wave). Table 4.2 reports the experimental thresholds for cardiac magnetostimulation in all pigs in terms of charging voltage for stimulation during early and late ventricular diastole. The average stimulation threshold measured during early diastole was 6.27 ± 1.33 kV, and 6.35 ± 1.82 kV during late diastole. The difference between the

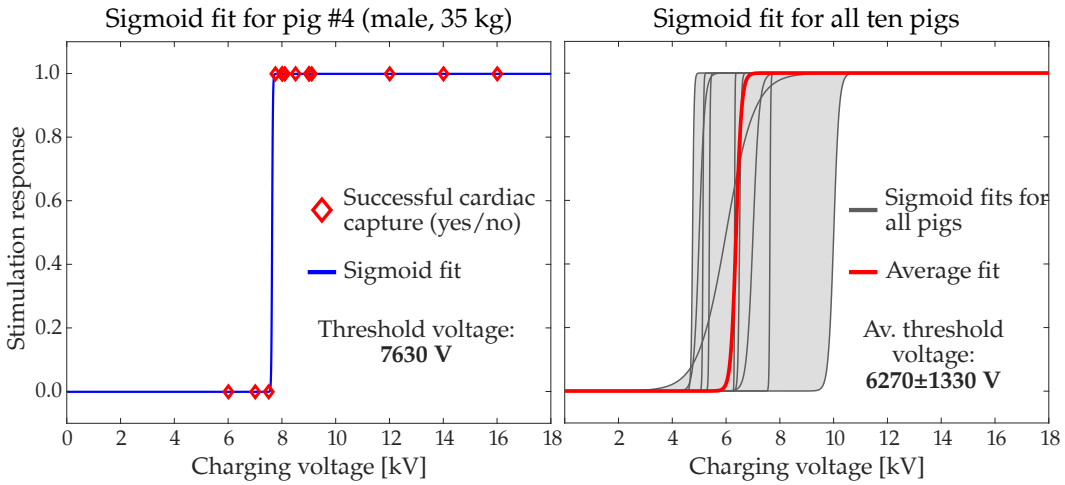

(a) Measured stimulation response versus charging voltage distribution with fitted sigmoid function for stimulation during early ventricular diastole (pig #4, left). The fitted threshold voltage was 7.63 kV in this case. The right plot shows sigmoid fits for all ten pigs. The average threshold voltage for all pigs was 6.27 ± 1.33 kV.

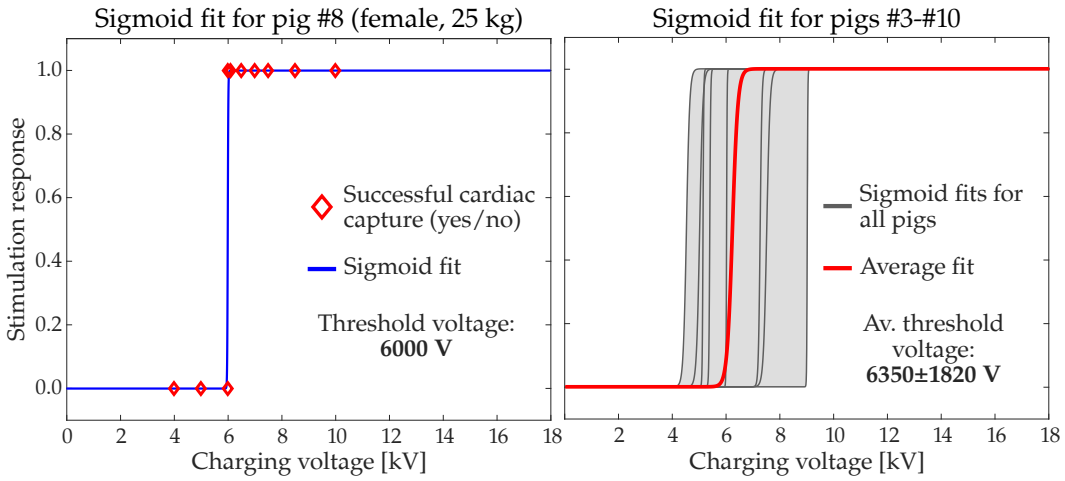

(b) Measured stimulation response versus charging voltage distribution with fitted sigmoid function for stimulation during late ventricular diastole (pig #8, left). The fitted threshold voltage was 6.0 kV in this case. The right plot shows sigmoid fits for the eight pigs for which measurements during late diastole could be evaluated. The average threshold voltage for these pigs was 6.35 ± 1.82 kV.

Figure 4.19: Sigmoid fits of the binary stimulation response of the porcine heart, i. e., cardiac capture (1) or no capture (0), to electromagnetic pulses generated by capacitor discharges at different charging voltages during early (a) and late (b) diastole. Both figures are taken from (Klein et al., 2022).

thresholds measured during early and late diastole was not statistically significant ($p > 0.88$, two-sided Wilcoxon rank sum test).

In one of the pigs (#5, male, 21 kg), CS thresholds were measured at five different time points during the cardiac cycle. Figure 4.20 shows those threshold values as a function of the time delay between the R-wave and the EMP. The stimulation

Table 4.2: Cardiac magnetostimulation thresholds in terms of charging voltage measured during ventricular diastole in ten healthy, anesthetized pigs. For pigs #1 and #2, the traces measured during late diastole were inconclusive, and were thus excluded from the threshold analysis. The table is taken from (Klein et al., 2022).

Pig	Sex	Weight [kg]	Threshold charging voltage [V] *(early diastole)*	Threshold charging voltage [V] *(late diastole)*
1	male	32	5000	–
2	male	31	7000	–
3	male	30	9000	10000
4	male	35	7630	7250
5	male	21	6500	5130
6	male	20	5130	7500
7	female	29	6310	5000
8	female	25	6000	6000
9	female	20	4750	4500
10	male	26	5380	5380
Mean ± SD		27 ± 5	6270 ± 1330	6350 ± 1820

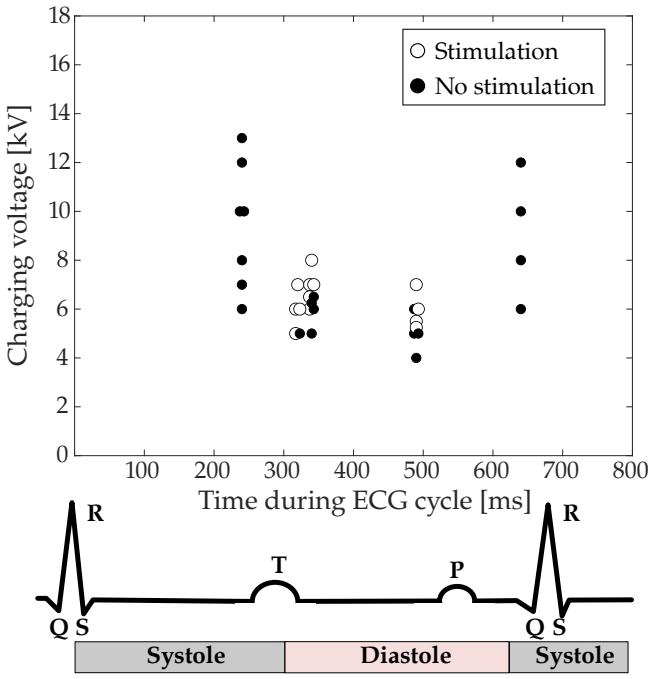

Figure 4.20: Cardiac threshold measurements (pig #5) in terms of charging voltage as a function of the delay after the R-wave at which the electromagnetic pulse was applied. White dots show supra-threshold events (successful cardiac capture), black dots show sub-threshold events (no cardiac capture). The figure is taken from (Klein et al., 2022).

threshold was lowest at the peak of the T-wave (5.0 kV), and stimulation during ventricular systole could not be achieved with charging voltages of up to 13.0 kV.

4.2.6 *EM field simulations in the porcine and in the human heart*

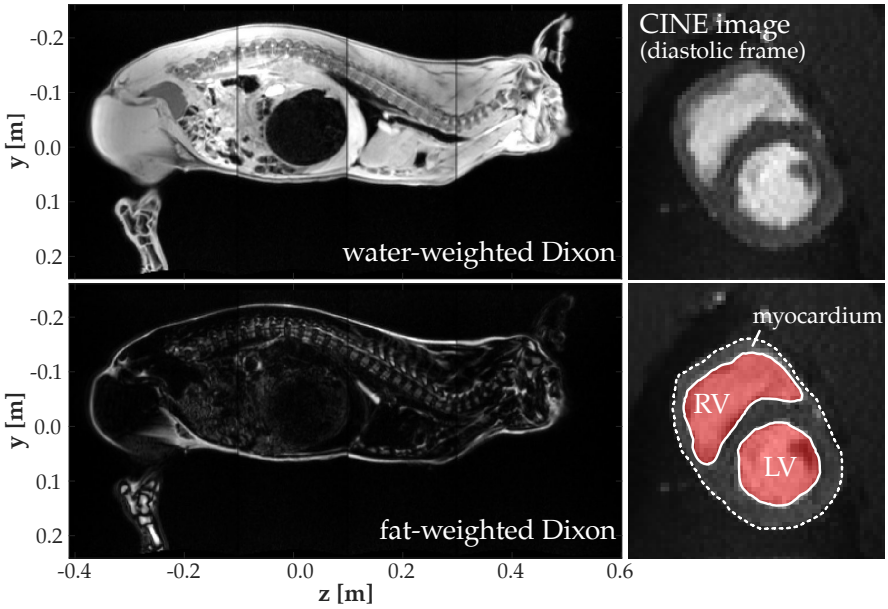

(a) Sagittal slices of the fat- and water-weighted Dixon image volumes and short-axis view of the CINE image volume. The CINE images were obtained at 23 different time points during the cardiac cycle. Shown here is the time frame corresponding to ventricular diastole, during which the ventricles are most relaxed (maximum volumes of the left (LV) and right ventricles (RV)).

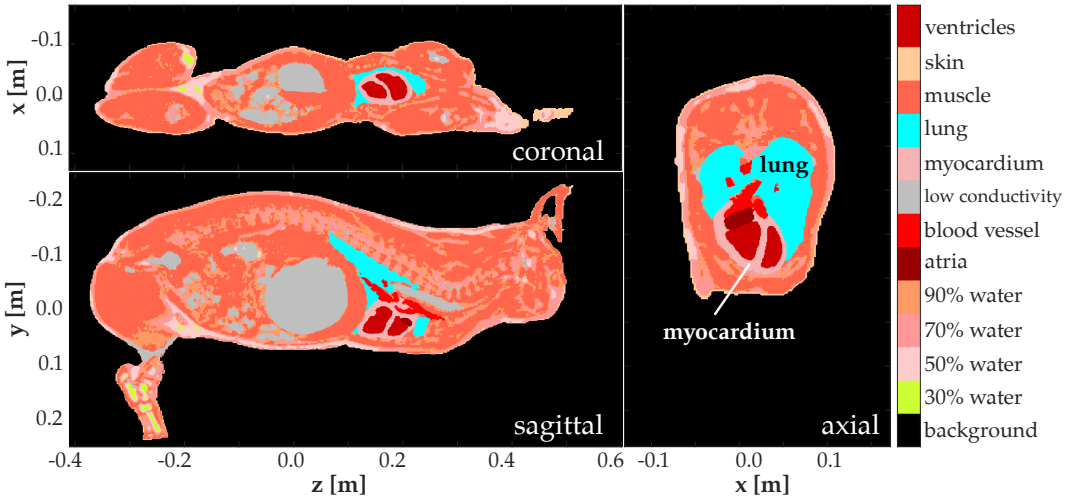

(b) Porcine body model obtained from semi-automatic segmentations of the Dixon and CINE images. The voxel model consists of twelve different tissue classes with a spatial resolution of 1x1x1 mm^3.

Figure 4.21: MR Dixon and CINE images of pig #7 (a) and the corresponding voxel model (b) obtained from semi-automatic segmentations of these images. Both figures are taken from (Klein et al., 2022).

Figure 4.21a shows sagittal slices of the whole-body water- and fat-weighted Dixon volumes as well as a short-axis view of the CINE volume (diastolic time-frame) acquired in pig #7 immediately after the cardiac stimulation experiment. Figure 4.21b shows the corresponding voxel model obtained by segmenting the Dixon and CINE volumes, as described in Section 3.2.5.

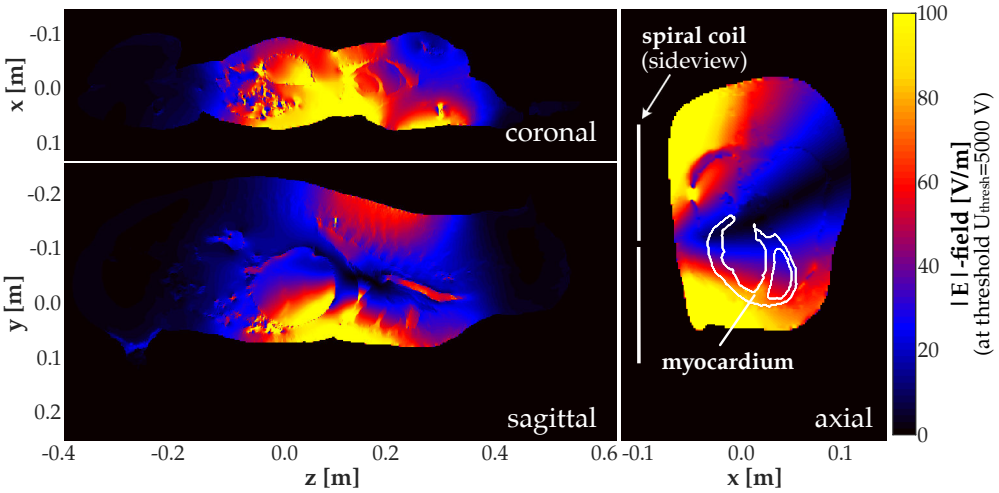

Figure 4.22: Coronal, sagittal, and axial slices of the simulated electric field induced in the porcine body model of pig #7 by the spiral coil, whose position is indicated in the axial slice. The electric field was scaled to match the experimental damped sinusoidal coil current waveform at the measured cardiac stimulation threshold ($U_{thresh} = 5.0$ kV). The figure is taken from (Klein et al., 2022).

Figure 4.22 shows the E-field induced in the body model of pig #7 at the experimental CS threshold measured during late diastole ($U_{thresh} = 5.0$ kV). The E-field distribution is very heterogeneous and has relatively high amplitudes in large parts of the torso, even outside of the myocardium.

Table 4.3 summarizes the B-field, B-field rate (dB/dt), and the 95th percentile E-field (E_{95}) simulated in the heart of the porcine body models. All values reported here were scaled to match the measured threshold voltage for stimulation during early diastole, the corresponding values for stimulation during late diastole can be found in Table A.1.

Table 4.4 reports dB/dt and E-field values generated by three commercial MRI gradient systems in the heart of a human male body model (head at isocenter) and within a 0.2-m radius cylinder. All values were evaluated at the maximum hardware limits of the respective gradient systems at an effective stimulus duration $t_{s,eff} = 0.45$ ms, as explained in Section 3.2.6. In this regime, the Sonata gradient is slew-rate-limited, i. e., it can only achieve a slew rate of 177 T/m/s, which is below its maximum slew rate $S_{max} = 200$ T/m/s. The Quantum and Connectome gradients, on the other hand, are amplitude-limited for $t_{s,eff} = 0.45$ ms. At $S_{max} = 140$ T/m/s, the Quantum gradient only reaches a gradient field amplitude of 31.5 mT/m instead of $G_{max} = 40$ mT/m, and the Connectome can only achieve an amplitude of 45 mT/m instead of $G_{max} = 300$ mT/m with $S_{max} = 200$ T/m/s. Corresponding values simulated for the heart-at-isocenter scan position can be found in Table A.2.

Table 4.3: Magnetic field amplitude and rate (B-field and dB/dt) and 95th percentile electric field values (E_{95}) simulated in the heart of the porcine body models. All values were scaled to match the experimental voltage threshold measured during early diastole (Table 4.2). The corresponding values for stimulation during late diastole can be found in Table A.1. For pigs #5 and #6, no MR images were acquired and thus no body models could be created. For these animals, the magnetic field was instead evaluated at a single point 11 cm above the coil center, which was the average coil-heart distance in the other pigs.

Pig	|B|-field [T] *at heart center*	dB/dt [T/s] *at heart center*	dB/dt [T/s] *mean in the heart*	dB/dt [T/s] *min. in the heart*	dB/dt [T/s] *max. in the heart*	dB/dt [T/s] *max. in the body*	E_{95} [V/m] *in the heart*
1	0.29	1380	1410	830	2440	5160	72.4
2	0.30	1450	1460	840	2550	6890	77.3
3	0.42	2010	2020	1240	3180	6530	96.0
4	0.39	1860	1940	1090	3380	6660	107.8
5	0.34	1630	No MRI	No MRI	No MRI	No MRI	No MRI
6	0.27	1290	No MRI	No MRI	No MRI	No MRI	No MRI
7	0.34	1660	1700	980	4000	5510	110.4
8	0.34	1620	1620	920	3040	5320	96.3
9	0.35	1680	1700	980	3090	5140	96.9
10	0.30	1460	1460	850	2680	4880	86.0
Mean $\pm$ SD	0.33 ± 0.05	1600 ± 220	1660 ± 230	970 ± 140	3050 ± 510	5760 ± 800	92.9 ± 13.5

Table 4.4: Maximum dB/dt and E-field values induced by three commercial gradient systems in a male human body model within the respective gradient hardware limits corresponding to an effective stimulus duration of $t_{s,eff} = 0.45$ ms. The dB/dt values were evaluated within a cylinder with 0.2-m radius along the *z*-direction (IEC definition of the gradient coil's "compliance volume" (IEC, 2010)), and in the myocardium of the body model placed with its head at isocenter. Corresponding values simulated for a heart-at-isocenter scan position can be found in Table A.2.

Gradient system	Coil axis	Max. dB/dt [T/s] *in a 0.2-m radius cylinder*	dB/dt [T/s] *at heart center*	dB/dt [T/s] *mean in the heart*	dB/dt [T/s] *min. in the heart*	dB/dt [T/s] *max. in the heart*	E_{95} [V/m] *in the heart*
Sonata	X-axis	55.7	34.6	35.2	32.9	37.9	1.7
	Y-axis	54.5	36.5	37.5	35.0	40.3	1.0
	Z-axis	51.7	40.7	41.2	40.1	42.4	2.0
Quantum	X-axis	57.6	37.5	38.0	37.0	39.9	1.8
	Y-axis	57.3	38.9	39.7	38.5	41.7	1.1
	Z-axis	50.6	39.1	39.6	38.4	41.0	1.9
Connectome	X-axis	53.8	25.1	26.3	21.6	31.5	1.2
	Y-axis	53.5	22.2	24.0	19.0	29.4	0.6
	Z-axis	58.2	52.0	52.1	50.3	53.8	2.5

For all gradient axes, the dB/dt values evaluated within the 0.2-m cylinder were higher than the dB/dt evaluated in the heart of the body model. This could be expected, as the B-field created by the coils generally increases with increasing radial distance from the central *z*-axis, reaching the highest values close to the coil wire. This can for example be seen in the B-field created by the Sonata Y-axis coil shown in Figure 3.10. Both the lowest and the highest dB/dt and E-field values in the heart were generated by the Connectome gradient system. For all investigated gradient systems, the Y-axis coil induced the lowest, and the Z-axis coil induced the highest E-field in the heart. This trend was previously demonstrated for the Sonata gradient (Figure 4.2), and was also reflected in higher simulated CS thresholds for the Y-axis compared to the other axes (Figure 4.3 and Figure 4.4).

In most cases, both dB/dt and the induced E-field in the body model's heart decreased when the body model was placed with the heart at the isocenter of the gradient coils (Table A.2). This is because the B-field magnitude created by the investigated coils, and consequently also dB/dt and the induced E-field, was lowest at the isocenter, as can be seen in Figure 3.10. Conversely, placing the body with the head at the isocenter exposed the heart to the maximum B-field created by the coils in the volume that is accessible to the patient.

The 95th percentile cardiac E-field created by the worst-case axis of the three MRI gradient systems and the two body positions was 37 times lower than the average threshold E-field in the pigs' heart. The average dB/dt created by the worst-case gradient coil axis in the human heart was 31 times lower than the cardiac dB/dt at threshold averaged across the pigs.

4.3 PREDICTION OF CARDIAC STIMULATION IN PORCINE MODELS

4.3.1 *Threshold simulation in porcine body models*

Figure 4.23 shows a vector plot of the E-field simulated in the myocardium of the MR-image-based body model of pig #7 and the E-field sampled along the subendocardial Purkinje fiber network modeled in this porcine model. The highest E-field amplitudes were induced in the apex.

Table 4.5 lists measured and simulated cardiac magnetostimulation thresholds in all pigs. All simulated thresholds are reported as an average ($\pm$ SD) of simulations in five different semi-random subendocardial Purkinje fiber networks. The predicted variability for thresholds simulated in different Purkinje fiber networks was between 2% and 10% (ratio of SD over mean). Similarly as in the previous simulations, the Purkinje fibers set the effective CS threshold, and the thresholds predicted for the ventricular muscle fibers were approximately five-fold higher. The average simulated CS thresholds in pigs #3 - #10 were in good agreement with the experimental thresholds. Specifically, the average simulated thresholds deviated between 3% and 10% from the experimental threshold measured during early diastole, and between 4% and 18% for measurements during late diastole. The CS thresholds simulated for pigs #1 and #2 were substantially higher (by 50%) than the experimental threshold. Nonetheless, the absolute maximum simulation error averaged across all porcine

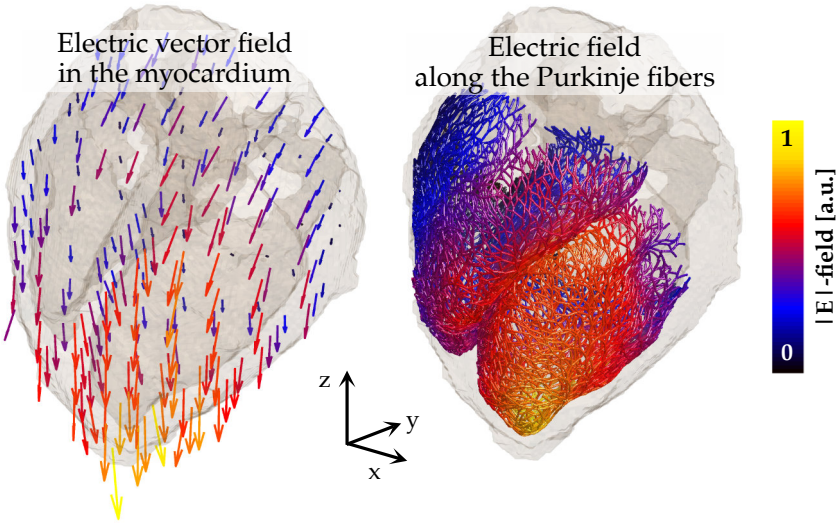

Figure 4.23: Vector plot of the electric field amplitude simulated in the myocardium of pig #7 (left) and electric field sampled along the subendocardial Purkinje fiber paths (right), which were added to the myocardial mesh using a rule-based modeling algorithm (Ijiri et al., 2008). The electric field is highest in the left ventricle, close to the apex.

models was 18% for measurements during early diastole, and 10% for measurements during late diastole.

4.3.2 *Sensitivity analysis of simulated cardiac stimulation thresholds*

A preliminary sensitivity analysis of the simulated CS thresholds was performed in the porcine body model of pig #7. Table 4.6 shows CS thresholds simulated in the most sensitive Purkinje fiber network modeled for pig #7 for varying electrical conductivity values assigned to the myocardium, muscle, blood, and lung tissues. The largest threshold changes were induced by variations of the heart muscle conductivity. In particular, reducing the myocardial conductivity by 50% decreased the simulated threshold by 22%.

Figure 4.24 shows E-fields and CS thresholds simulated in the porcine model of pig #7 for shifts of the spiral coil from its default position by ±10 mm in the x-, y-, and z-direction (Figure 4.21 shows the definition of the spatial axes). The largest changes in E_{95} in the heart and the predicted CS threshold occurred for coil shifts in the x-direction, which changed the vertical distance between the coil and the pig's torso. This emphasizes the importance of carefully recording this parameter in the experiments to accurately reproduce the coil setup in the model. On the other hand, coil shifts along the y- and z-directions had negligible effects on the threshold of less than ±2%.

Figure 4.25 shows CS thresholds simulated in the porcine model of pig #7 for ±50% variations of important electrophysiological parameters of the Purkinje fiber model. The largest increase of the predicted CS threshold (+35%) was observed for

Table 4.5: Comparison of measured and simulated cardiac magnetostimulation thresholds in ten pigs. The cardiac stimulation thresholds predicted for each porcine model are given as mean and standard deviation (SD) of thresholds simulated in five subendocardial Purkinje fiber networks. For pigs #5 and #6, no MR images were acquired, thus it was not possible to create porcine body models and simulate thresholds for these pigs.

	Experiments		Simulations		
Pig	Threshold voltage [V] *(early diastole)*	Threshold voltage [V] *(late diastole)*	Threshold voltage [V]	Simulation error [%] *(early diastole)*	Simulation error [%] *(late diastole)*
1	5000	–	7500 ± 580	+50	–
2	7000	–	10410 ± 200	+49	–
3	9000	10000	9300 ± 500	+3	−7
4	7630	7250	6860 ± 230	−10	−5
5	6500	5130	No MRI	No MRI	No MRI
6	5130	7500	No MRI	No MRI	No MRI
7	6310	5000	5890 ± 270	−7	+18
8	6000	6000	5770 ± 370	−4	−4
9	4750	4500	5110 ± 440	+8	+14
10	5380	5380	4830 ± 480	−10	−10

Table 4.6: Impact of electrical conductivity variations of single tissues on the electric field (E_{95}) in the heart and on the CS threshold simulated in the porcine body model of pig #7. Percent changes are given relative to the baseline simulation (first row), in which all tissue conductivity values were set based on the IT'IS low-frequency (LF) material database (Hasgall et al., 2018).

Tissue	Electrical conductivity [S/m]	Cardiac E_{95} [mV/m] *(at 1 A, 1 kHz)*	Sim. threshold [V] *(charging voltage)*
Baseline	IT'IS LF database	26.2	5460
Heart −50%	0.191	37.0 (+41%)	4260 (−22%)
Heart +50%	0.572	22.7 (−13%)	5810 (+6%)
Muscle −50%	0.178	22.1 (−16%)	6200 (+14%)
Muscle +50%	0.533	29.2 (+11%)	5100 (−7%)
Blood −50%	0.330	26.2 (+0%)	5040 (−8%)
Blood +50%	0.990	27.5 (+5%)	5810 (+8%)
Lung −50%	0.053	26.2 (+0%)	5520 (+1%)
Lung +50%	0.158	26.3 (+0.4%)	5420 (−1%)
Lung deflated	0.529	26.8 (+2%)	5360 (−2%)

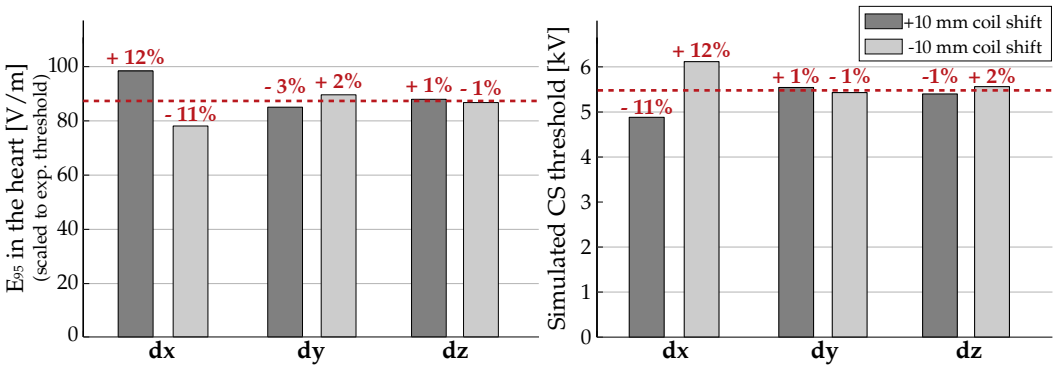

Figure 4.24: Effect of coil shifts of ±10 mm in the x-, y-, and z-direction on the 95th percentile electric field E_{95} in the heart (left) and on the cardiac stimulation threshold (right) simulated in the porcine body model of pig #7. The electric field was scaled to match the experimental voltage threshold of U_{thresh} = 5.0 kV. Percent changes are given with respect to the E_{95} and CS threshold values simulated for the default coil position (E_{95} = 87.5 V/m (Table A.1) and $U_{thresh,sim}$ = 5.46 kV, respectively).

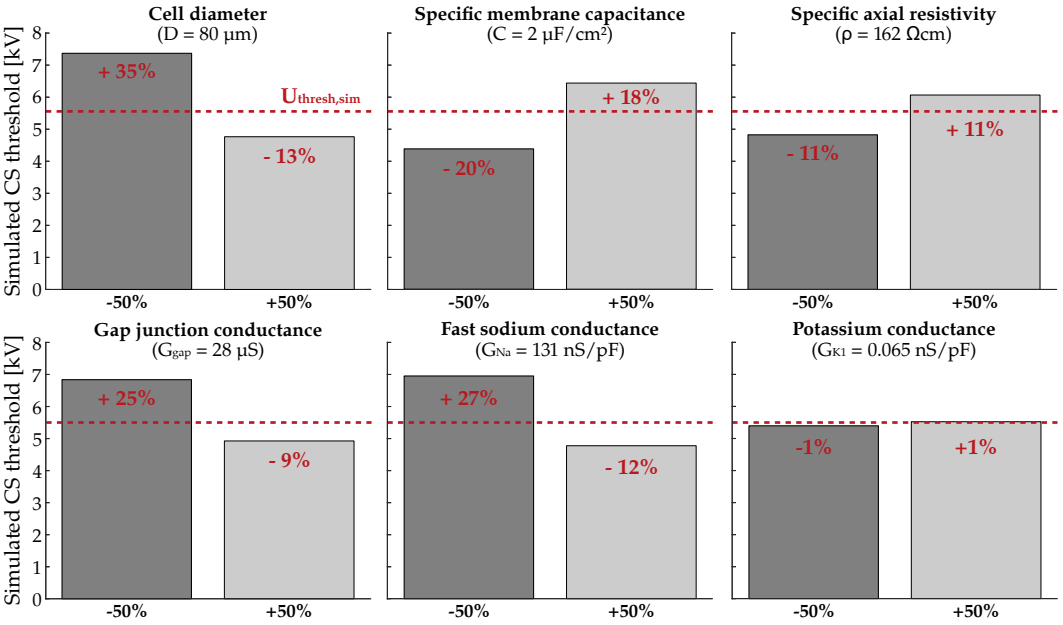

Figure 4.25: Cardiac stimulation thresholds simulated in the porcine body model of pig #7 for ±50% variations of electrophysiological parameter values of the Purkinje fiber model. All thresholds were simulated in the Purkinje fiber network that yielded the lowest threshold ($U_{thresh,sim}$ = 5.46 kV) for the default parameter values.

a 50% reduced cell diameter, while the largest decrease of the threshold (−20%) was caused by a 50% decreased specific membrane capacitance.

5 DISCUSSION

This chapter discusses the findings of the three main parts of this thesis: first, the development of a modeling framework for the prediction of cardiac magnetostimulation in human and animal body models; second, the measurement of magnetostimulation thresholds in the porcine heart; and third, the prediction of cardiac stimulation thresholds in anatomical models of the specific animals under study in the experiments. The first part has been partially published in (Klein et al., 2021)[1], and the second part has been submitted as (Klein et al., 2022). Parts of the corresponding descriptions are replicated from the named publications.

5.1 MODELING FRAMEWORK FOR CARDIAC MAGNETOSTIMULATION

In the first part of this thesis, a numerical modeling framework was developed for the prediction of cardiac stimulation (CS) by time-varying magnetic fields (magnetostimulation). The framework combines EM field simulations in anatomical models of humans and animals with realistic geometrical and electrophysiological descriptions of electrically excitable cardiac tissue, more specifically the Purkinje and ventricular muscle fibers. The model can predict the threshold at which an E-field distribution and amplitude induced by a given coil geometry and magnetic field waveform stimulates the cardiac fibers. In this work, the CS threshold is defined as the smallest coil current amplitude, or, equivalently, the smallest gradient field amplitude, that initiates an AP in any of the fibers. This is a reasonable assumption in that an AP created in a single cardiac cell or a small group of cells can propagate and lead to excitation of the entire myocardium (Tacker and Geddes, 1996).

Preliminary validation in canine models

Unlike PNS thresholds, which are routinely measured in healthy human volunteers (Budinger et al., 1991; Feldman et al., 2009; Schaefer et al., 2000), it is not feasible to measure magnetostimulation thresholds of the heart in human subjects. While onset PNS is mild and harmless for the subject (Bourland et al., 1999; Schaefer et al., 2000), CS can result in life-threatening arrhythmias, possibly even in the event of a single stimulated heartbeat that occurs during the vulnerable phase of the cardiac cycle (Antoni, 1998; Reilly, 1992b). To date, CS thresholds in humans have only been measured with electrodes (electrostimulation), mainly in patients with pacemakers (Bowman and Hughes, 1984; Brandt et al., 1990; Coates and Thwaites, 2000; Dhar et al., 2009; Kleinert et al., 1983; Scally et al., 2007). Electrodes induce E-fields through electrostatics, yielding field distributions that differ from those induced by time-varying magnetic fields. E-fields created by electrodes are more focal, thus

1

only stimulating a small patch of tissue around the electrode tip, while magnetically induced E-fields are usually more distributed. It is therefore not straightforward to extrapolate electrostimulation measurements in humans to magnetostimulation thresholds.

Given the lack of experimental data on human cardiac magnetostimulation, it is challenging to validate the modeling framework developed in this work. A preliminary validation was based on a comparison with two experimental studies performed in canines in 1992 (Mouchawar et al., 1992; Nyenhuis et al., 1992). Similarly to the present work, the authors were interested in the cardiac safety of MRI gradient fields. The study conducted by Mouchawar et al. measured cardiac magnetostimulation thresholds in eleven anesthetized canines using a pair of coplanar spiral coils (COP) (Mouchawar et al., 1992), while Nyenhuis et al. used a solenoid coil (SOL) to measure CS in a cohort of twelve canines (Nyenhuis et al., 1992). Another experimental study by the same authors used a small-scale MRI gradient coil (26 cm diameter, 55 cm length) driven by a capacitor (Nyenhuis et al., 1992). However, CS could not be achieved in the canines using this small gradient coil (Nyenhuis et al., 1992).

The experimental setup of the canine studies were replicated as closely as possible in the simulations based on the reported experimental details. The publications reported the weight range of the canines but not the relationship between the weight and the stimulation threshold measured in each individual canine. No details were given on the exact anatomy of the animals, other than the species that was used (Mongrel dogs (Mouchawar et al., 1992; Nyenhuis et al., 1992)). The simulations conducted in this work used the HML canine model of a Doberman (Kramer et al., 2012), which was scaled in size to match the weight range of the canines from the experiments.

Despite these simplifications, the average simulated and measured thresholds showed a good agreement with only 2% error for the COP coil. The standard deviation of the thresholds predicted for different canine weights was 3%, which is smaller than the 8% standard deviation observed in the experiments (Mouchawar et al., 1992). For SOL, the average simulated CS threshold was 28% higher than the average experimental threshold. The largest deviation between predicted and measured thresholds was observed for the 17-kg canine body model, while the threshold simulated in the 32-kg model exactly matched the measured threshold. In the experiments, the observed standard deviation was only 5% (Nyenhuis et al., 1992), compared to 24% in the simulations. One possible reason for this discrepancy in predicted and experimental standard deviations might be that in the SOL study, CS was only achieved in five out of twelve canines (Nyenhuis et al., 1992). Unfortunately, the individual sizes and weights of the successfully stimulated canines were not reported.

The lack of detailed information on the anatomy of individual canines under study required the use of a generic body model in the simulations. This simplification inevitably leads to a reduced CS threshold prediction accuracy, as the anatomy greatly impacts the induced E-field and thus the CS threshold. Furthermore, the HML canine model only possesses a crude representation of the heart that lacks a description of the atrial and ventricular volumes. The internal heart geometry of the female human Zygote model was thus inserted into the HML model. While the initial sim-

ulations in the generic canine model yielded important insights, the aforementioned uncertainties stress the importance of using individualized models of the animal's anatomy in any further validation of the CS modeling framework, as done in the third part of this thesis. Another important parameter that affects the predicted E-fields and CS thresholds is the electrical tissue conductivity of the myocardium and surrounding tissues. This parameter was not directly measured in the canine experiments and was instead taken from the IT'IS database of average low-frequency tissue conductivity values (Hasgall et al., 2018). Finally, the simulations used electrophysiological models of Purkinje cells and ventricular myocytes of the human heart (O'Hara et al., 2011; Stewart et al., 2009). The ion dynamics in canine cardiac cell membranes may differ from those in humans. This uncertainty could be tackled in future work by simulating and comparing stimulation thresholds using a dedicated membrane model for the canine ventricular cardiomyocyte (Hund and Rudy, 2004).

Comparison of simulated CS thresholds and the IEC 60601-2-33 regulatory limit

The IEC 60601-2-33 regulatory standard limits MRI gradient system's dB/dt and induced E-field to prevent CS (IEC, 2010). The IEC limit is based on the exponential strength-duration curve that quantifies the threshold for tissue stimulation as a function of the E-field or dB/dt pulse duration (Equation 2.71). The parameter values underlying the IEC strength-duration curve were chosen 30 years ago, and based mainly on electrostimulation experiments and simple analytical E-field calculations in a homogeneous model of the male human torso (Reilly, 1991, 1992b). The uncertainties associated with these simplifications and the lack of human cardiac magnetostimulation thresholds have likely required a conservative approach in the definition of the IEC limit, which is now starting to impact gradient performance.

Simulations of the Siemens Sonata gradient system indicated that for the investigated gradient waveforms and rise times ($t_{rise} \leqslant 5.0$ ms), the predicted CS thresholds were at least 10-fold higher than the IEC cardiac limit (Figure 4.3). In addition, the predicted CS thresholds were between 6-fold ($t_{rise} > 2.5$ ms) and 25-fold ($t_{rise} < 0.5$ ms) higher than the PNS thresholds for all axes of the Sonata gradient system. This prediction is in alignment with previous work that estimated that the heart should have an up to 200-fold higher magnetostimulation threshold than peripheral nerves at short rise times (Irnich, 1994). There are several possible reasons for the large difference between PNS and CS thresholds. First, the heart is located deeper in the body than peripheral nerves, and thus mostly experiences lower E-fields. Second, the myocardium is known to have a longer strength-duration time constant of approximately 2-3 ms (Irnich, 1994; Reilly, 1992b) than peripheral nerves, which have time constants on the order of hundreds of microseconds (Irnich and Schmitt, 1995; Reilly, 1992a). This means that the CS threshold decreases more slowly for increasing durations of the applied dB/dt or E-field pulse.

The IEC cardiac limit refers to the maximum dB/dt value achieved during the slew period of a linear or sine-shaped gradient ramp (IEC, 2010), and is independent of other waveform parameters such as the plateau duration or the number of gradient lobes. This assumption ignores the fact that gradient waveforms with different numbers of bipolar lobes or with varying plateau durations can have different

stimulation thresholds. For example, previous measurements found an inverse correlation between the cardiac fibrillation threshold and the number of stimulating pulses (Roy et al., 1977; Sugimoto et al., 1967), which is in alignment with the CS simulations performed in this work (Figure 4.9). Another experimental study that measured PNS in healthy volunteers found minimal PNS thresholds for plateau durations around 1 ms, and higher thresholds for shorter and longer plateau durations (Abart et al., 1997). Such a non-linear threshold dependence on the plateau duration was also predicted by the CS model. However, the PNS threshold changes that the authors found in their experiments were less pronounced (less than a few percent (Abart et al., 1997)) than the predicted CS threshold changes.

For most MRI gradient systems and waveforms, the PNS thresholds are more limiting than the IEC cardiac limit. For some high-amplitude gradient systems, however, the IEC limit is met first for gradient pulses with long rise times. This is, e. g., the case for simultaneous slewing of all three axes of the Siemens Connectome gradient with rise times $t_{rise} \geqslant 1.5$ ms, for which the IEC limit becomes lower than the experimental PNS threshold (Figure 2.6). Such long rise times are especially important for diffusion imaging, which requires long and high-amplitude gradient pulses to encode the diffusion of spins in the MR signal. In contrast to the IEC limit, the predicted CS thresholds for the Y-axis coil of the Connectome gradient were between 32 and 56 times higher than the IEC limit, and >45-fold higher than the experimental PNS thresholds for the investigated rise times (0.1 ms to 5.0 ms).

A comparison of the predicted CS thresholds for the Y-axis coils of the Sonata (Figure 4.3) and the Connectome gradient (Figure 4.5) indicates that whole-body gradient coils with similar winding topologies can have widely different CS thresholds. Both gradient coils are actively shielded, symmetric, and use cylindrical coil former shapes, i. e., they do not have funnels, flanges, or folds. The coils differ in diameter (70 cm for the Sonata, and 63 cm for the Connectome), in the size of the linear volume (FOV) and the gradient linearity within these volumes (40 cm and 10.5% for the Sonata, respectively, and 20 cm and 6% for the Connectome). These differences seem sufficient to generate fundamentally higher CS thresholds in the Connectome compared to the Sonata Y-axis coil. In particular, the predicted Purkinje fiber threshold for the Connectome is between 60% and 70% higher than that of the Sonata. This difference in CS thresholds may reflect the fact that the Sonata gradient coil places the peak B-fields, and thus the peak E-fields, in the cardiac region of the body models when their head is at isocenter. The Connectome gradient coil, on the other hand, places the peak B-fields slightly higher in the chest and thus induces lower E-fields in the heart.

Simulated electric field strength-duration curves

E-field strength-duration curves are widely used to describe the excitability of nerves, muscle, and the myocardium as a function of the stimulation pulse duration (Geddes and Bourland, 1985a,b; Mouchawar et al., 1989; Tacker and Geddes, 1996). While the strength-duration curve formulation may describe single measurements well, there are indications that the curve parameters, i. e., rheobase and chronaxie or time constant, are not universal. For example, a literature review of 17 electros-

timulation experiments in animals and humans conducted by Irnich found that the E-field rheobase for the hyperbolic formulation of the strength-duration curve (Equation 3.10) varied between 20 V/m and 147 V/m (Irnich, 1994). Another review conducted by Reilly compiled a set of 21 experiments in different animal species (canines, sheep, rabbits, guinea pigs, etc.) using varying electrode configurations, stimulation loci, etc. The author analyzed the data using the exponential strength-duration formulation (Equation 3.11), and reported time constant values between 0.2 and 7.7 ms (Reilly, 1992b).

In other words, neither the E-field rheobase nor the time constant seem to be constant across species, experimental setups and stimulation locations. There are at least two reasons for this: First, the determination of the E-field created in the experiments is complicated. Most often, the E-field cannot be measured directly and is instead calculated based on a simplified representation of the experimental setup. For example, the tissues are modeled with simple geometrical shapes and assigned with homogeneous conductivity values (Mouchawar et al., 1992). Second, the time constants are known to depend strongly on body temperature (Geddes and Bourland, 1985b), fitting method (Mouchawar et al., 1989), and electrode size (Reilly, 1992b). A large time constant variability has also been observed in the case of magnetostimulation of peripheral nerves, as the chronaxie of different MRI gradient systems varies widely between 365 and 1030 µs for body gradients, and 294 and 1100 µs for head gradients (Chronik and Rutt, 2001).

In this work, E-field strength-duration curves were simulated for the male and female human body models placed in the three axes of the Sonata gradient system to compare the CS modeling framework with previous CS threshold estimations. The average E-field rheobase predicted using the hyperbolic fit function ($E_{rheo,hyp} = 18.7 \pm 1.4$ V/m) is on the lower end of the range of rheobase values estimated for electrostimulation experiments (20 V/m to 147 V/m (Irnich, 1994)), and the simulated (hyperbolic) chronaxie (1.4 ± 0.3 ms) is smaller than the average experimental value (2.0 ms (Irnich, 1994)). The average E-field rheobase predicted with the exponential fit function ($E_{rheo,exp} = 24.3 \pm 1.6$ V/m) is twice as high as the 12 V/m rheobase proposed by Reilly for the population average (Reilly, 1991, 1992b). The average simulated (exponential) time constant of 1.1 ± 0.2 ms falls within the relatively large experimental range (0.2 ms to 7.7 ms (Reilly, 1992b)), but is smaller than the average time constant of 3 ms used in the IEC standard (IEC, 2010). The simulated strength-duration parameters thus broadly agree with previously published values, even though the agreement is not perfect. It should again be stressed that the literature values show a wide variability, and that it is not straightforward to compare E-field magnitudes between different experiments due to simplifications in the E-field estimations. The hyperbolic Lapicque expression of the strength-duration curve fitted the simulated data better than the exponential Blair expression. This finding is in accordance with previous work that fitted experimental electrostimulation thresholds of the canine heart (Mouchawar et al., 1989) and is in contrast to the safety limit in the IEC standard, which is based on the exponential strength-duration curve.

Different excitability of Purkinje and ventricular muscle fibers

In all simulations, the human Purkinje fiber model (Stewart et al., 2009) was more sensitive to stimulation than the ventricular muscle fiber model (O'Hara et al., 2011). Previous experiments in cardiac tissue of canines demonstrated that high-voltage shocks with a 5-ms pulse duration had fundamentally different effects on isolated Purkinje and ventricular muscle fibers (Li et al., 1993). The authors recorded TMV in both tissue types and found that the same shock intensity evoked a stronger depolarization in the Purkinje fibers. Moreover, they found that the Purkinje fibers fired APs at a rapid rate in response to the stimulus, while the ventricular muscle tissue exhibited a transient refractory state (Li et al., 1993).

The different excitability may be caused by the larger diameter of Purkinje fibers (80 µm (Legato, 1973)) compared to ventricular muscle fibers (16 µm (Legato, 1973)). For peripheral nerve fibers, larger fiber diameters correlate with lower stimulation thresholds (Davids et al., 2017; Enoka, 2002), which likely applies to cardiac fibers as well. Aside from their different diameters, Purkinje cells and ventricular myocytes have distinct electrophysiological properties (Han et al., 2002a, 2000, 2002b; Li et al., 1993). The different ionic currents of both cell types result in distinct AP shapes. Moreover, Purkinje fibers exhibit an automatic pacemaking activity that is not present in ventricular muscle.

Previous modeling studies investigating the effect of Purkinje fibers on the cardiac response to defibrillation shocks found that the one-dimensional cable structure of Purkinje fibers makes them more excitable than the bulk of myocardial tissue (Boyle et al., 2010; Vigmond and Clements, 2007). The geometry of Purkinje fibers thus appears to contribute to their higher sensitivity to stimulation compared to ventricular muscle. The subendocardial network of Purkinje fibers exhibits sharp bends in some locations, while the ventricular fiber paths are comparatively smooth. Bends or kinks in an excitable fiber subjected to an extracellular E-field can cause large changes in the tangential E-field along the fiber, and thus high values of the activation function (Davids et al., 2019b; Rattay, 1986). The simulations conducted in this work demonstrated that the activation function is an indicator for the excitability of a cardiac fiber (Figure 4.7), which is in agreement with previous experiments and simulations in cardiac tissue (Knisley et al., 1999). This finding stresses the importance of modeling both the E-field and the embedded excitable fiber paths to make reliable predictions of CS thresholds rather than only investigating the E-field magnitude in the heart, as done by previous work on cardiac safety (Pastore et al., 2011; Wang et al., 1995).

Limitations of the modeling framework and future work

The simulations performed in this work only included fibers in the ventricles (Purkinje and ventricular muscle). Electrostimulation studies in humans using pacemaker leads showed that the ventricles have a similar or lower stimulation threshold than the atria (Brandt et al., 1990; Kleinert et al., 1983), and the same has been found for canines and pigs (Bowman and Hughes, 1984). Assuming that excitable fibers in the ventricles are more sensitive to magnetostimulation as well, it might thus be suffi-

cient to model only these fibers to accurately predict cardiac magnetostimulation thresholds. Nonetheless, this hypothesis should be tested in future work. Similarly as for the ventricular fibers, atrial fibers could be added to the body models using specific rule-based algorithms developed for modeling atrial fiber paths (Dössel et al., 2012; Piersanti et al., 2021). These fiber paths could be combined with published electrophysiological models of human atrial muscle cells (Grandi et al., 2011) to verify that their thresholds are higher than those for the excitable fibers in the ventricles. Other types of cardiac tissue that are not yet included in the model are the SA and AV nodal cells. Less data is available for the stimulation sensitivity of nodal cells, but experiments indicate that they also have greater thresholds than those of ventricular tissue (Merideth et al., 1968). This finding could be verified in the simulations by adding ion-dynamic models of nodal cells (Fabbri et al., 2017; Inada et al., 2009) at their respective locations in the heart.

The current modeling pipeline does not include the natural cardiac pacemaking activity, i. e., the model does not capture propagation of electrical depolarization waves initiated by the SA and AV nodes through the Purkinje and ventricular muscle fibers. Instead, all CS thresholds were simulated with the Purkinje and ventricular fibers at rest, i. e., during diastole. One of the previous canine magnetostimulation studies found no difference in CS thresholds of the beating and arrested heart (Nyenhuis et al., 1992). From a safety perspective, it is likely sufficient to perform simulations for diastole, since this is the most sensitive heart phase for excitation (Reilly, 1992b), as was also observed in the porcine experiments performed in the second part of this thesis. However, it might be informative to compare systolic and diastolic thresholds in the simulations to verify this point. To this end, the pacemaking activity of the SA and AV nodes could be included in the threshold simulations. Analogously to the Purkinje cell model (Stewart et al., 2009), the nodal cell models initiate spontaneous pacemaking APs (Fabbri et al., 2017; Inada et al., 2009), which could be propagated into the Purkinje fiber model.

Future simulations should include a larger variety of body models including obese adults, pregnant women, and children of various ages to better reflect a diverse population. Similarly to a sensitivity analysis conducted previously for PNS simulations (Klein et al., 2019), the impact of physiological parameters such as body size, weight, shape, and electrical tissue conductivity values on the predicted CS thresholds should be assessed. This seems important, as the simulations performed in this work showed that even mild changes of the Purkinje fiber paths can have an impact on the CS threshold, depending on the duration of the applied stimulus (Figure 4.8). A comparison of 13 in vitro and in vivo electrostimulation studies conducted in humans and different animal species found that if differences in the experimental setup are carefully accounted for, the CS threshold varied by $<25\%$ across the reviewed studies for a 2-ms undamped capacitor discharge waveform (Lepeschkin et al., 1978). A systematic sensitivity analysis of the CS modeling framework could help studying the sources of variability of CS thresholds across the population for a larger variety of stimulus durations and waveforms.

This analysis should also study effects of cardiac pathologies on the CS threshold, such as ischemia and infarction, as well as the effect of drugs, changes in electrolyte concentration or body temperature, which are all known to affect cardiac excitabil-

ity (Antoni, 1998; Liu et al., 2003). Previous work suggested that a safety factor of three should be used to account for thus arising uncertainties in the CS threshold (Irnich and Schmitt, 1995; Reilly, 1992a), which has been adopted by the IEC regulatory standard (IEC, 2010). Cardiac activity can also be affected by sympathetic and parasympathetic nerves of the autonomous nervous system. Deliberate electrical stimulation of the vagus nerve can, e. g., lead to cardiac arrest (Antoni, 1998; Matheny and Shaar, 1997). Future simulations should thus also investigate stimulation thresholds of autonomous nerve fibers located close to the heart.

5.2 MEASUREMENT OF MAGNETOSTIMULATION IN THE PORCINE HEART

In the second part of this thesis, cardiac magnetostimulation thresholds were measured in ten healthy, anesthetized pigs. A thorough search of the relevant literature yielded no experimental studies of cardiac magnetostimulation in vivo since the canine studies performed in the early 1990s (Bourland et al., 1991; Mouchawar et al., 1992; Nyenhuis et al., 1992; Yamaguchi et al., 1991, 1992), and no study to do so in the pig, which has become an important large animal model for the human cardiovascular system. The porcine and human heart have a similar size and AP duration (Gaur et al., 2021), which is why the pig is commonly used in experimental studies of cardiac diseases or mechanisms for arrhythmias (Azarov et al., 2018; Valdeomillos et al., 2019) as well as to investigate potential therapies thereof (Dixon and Spinale, 2009).

In this thesis, a magnetic stimulator was constructed consisting of a 220-µF capacitor discharged into a flat spiral coil ($L = 235$ µH, $R = 95$ mΩ) placed close to the porcine chest, creating damped sinusoidal magnetic field pulses with an effective stimulus duration of $t_{s,eff} = 0.45$ ms. The average CS threshold measured with this setup was $dB/dt = 1.66 \pm 0.23$ kT/s (average±SD, $E_{95} = 92.9 \pm 13.5$ V/m) in the porcine heart for stimulation during early ventricular diastole, and $dB/dt = 1.69 \pm 0.32$ kT/s ($E_{95} = 95.1 \pm 8.3$ V/m) during late diastole. The threshold difference for measurements during early and late diastole was not statistically significant at $p < 0.05$. The inter-individual variability of the measured CS thresholds was on the order of 15% (SD relative to mean threshold). This variability is comparable to previous canine studies that used a solenoid coil for cardiac excitation (Bourland et al., 1991). There was a weak positive correlation between the measured CS threshold and the porcine weight, with Pearson correlation coefficients of $\rho = 0.54$ for stimulation during early diastole and $\rho = 0.43$ during late diastole. A correlation between the measured thresholds and the animal's sex could not be established because only three female pigs were measured. Future experiments should include animals with a wider weight range (animal weights in the current study ranged from 20 kg to 35 kg) and an equal number of male and female animals to reliably test weight- and sex-dependent CS threshold variations.

The CS thresholds in this work were obtained by fitting the binary cardiac response, i. e., no stimulation or cardiac capture indicating stimulation, at different capacitor charging voltages with sigmoid functions (Figure 4.19). In some cases, the cardiac response was inconsistent around the stimulation threshold, i. e., sometimes a sub-threshold voltage led to cardiac capture, or a supra-threshold voltage failed

to stimulate the heart. Similar intra-individual inconsistencies have been observed in previous PNS experiments on human volunteers (Saritas et al., 2013). There are a number of reasons why the CS threshold might vary slightly during measurements in one pig. First, the EMPs were not synchronized with the breathing phase. Both the impedance of the lungs and the torso shape change during the breathing cycle, which may affect the induced E-field strength and distribution, and thus the CS threshold. Second, the charging of the capacitors took up to two minutes. Over the course of several charging periods, the animal's heart rate may have decreased (longer RR interval) under the influence of anesthesia. This may have led to slight variations in the timing of the pulse relative to the cardiac cycle as the EMPs were applied at fixed delays after the R-wave.

Comparison of porcine and canine cardiac magnetostimulation thresholds

One of the previous experimental studies used a solenoid coil for excitation of the canine heart (Nyenhuis et al., 1992). The authors reported an average threshold of ~4.5 kT/s at the coil center (Nyenhuis et al., 1992), which roughly coincided with the location of the canine heart. This threshold value is substantially higher than the average dB/dt threshold measured at the center of the porcine heart (1.66 kT/s). Another canine study used a coplanar pair of spiral coils for excitation (Mouchawar et al., 1992), and found an average experimental threshold of ~17.0 kT/s at the center of each coil. This value is almost twice as high as the dB/dt threshold of ~9.3 kT/s computed at the center of the spiral coil for the porcine study.

Previous simulations of the canine experimental setups (Klein et al., 2021; Ragan et al., 1995) found E-field amplitudes between 90 and 110 V/m in the heart of canine body models at the experimental threshold. These value are very similar to the average E-field threshold determined in the porcine heart ($E_{95} \approx 93$ V/m), which may suggest that canines and pigs do have a similar CS threshold in terms of E-field magnitude. Furthermore, this finding hints to the point that the E-field is likely a better surrogate for stimulation than dB/dt. However, comparing these thresholds is difficult, because they are associated with slightly different EM field waveforms and stimulus durations. In the canine studies, the EMP had a lower frequency (ca. 450 Hz) than in the porcine study (715 Hz), and a higher damping factor ($D = 0.11$ (Mouchawar et al., 1992) compared to $D = 0.04$ in the porcine study).

Comparison with MRI gradient-induced dB/dt and E-field values

For comparison, EM fields were simulated in the heart of a human male body model for the three axes of the Siemens Sonata, Quantum, and Connectome whole-body MRI gradient systems. All gradient-induced dB/dt and E-field values simulated in the human heart were substantially lower than the measured threshold values in the porcine heart. Even the highest dB/dt value simulated in the human heart ($dB/dt_{max} = 53.8$ T/s for the Connectome Z-axis coil) was 14 times lower than the smallest dB/dt value in the porcine heart at the experimental threshold ($dB/dt_{min} = 780$ T/s for pig #7, measured during late diastole). The Connectome Z-axis also induced the highest E-field in the human heart ($E_{95} = 2.5$ V/m). This value was 29

times lower than the lowest threshold E-field simulated in the heart of the porcine models ($E_{95} = 72.4$ V/m for pig #1, early diastole).

The IEC 60601-2-33 regulatory standard defines whole-body gradient safety limits as the maximum dB/dt value in a cylindrical volume with 0.2-m radius oriented along the z-axis of the scanner (IEC, 2010). For all gradient coils investigated in this work, the dB/dt value evaluated in such a cylinder was between 12% and 140% greater than the dB/dt in the heart when the body model was placed with its head at the isocenter. The evaluation of maximum dB/dt in a 0.2-m cylinder thus likely adds an additional safety factor to the regulatory dB/dt limit. At an effective stimulus duration of $t_{s,eff} = 0.45$ ms, the IEC limit is $dB/dt_{IEC} = 144$ T/s. This value is 11-fold lower than the average experimental porcine threshold evaluated as dB/dt at the center of the porcine heart (1.66 kT/s), and 40-fold lower than the maximum dB/dt in the whole porcine body at the average experimental threshold (5.76 kT/s). The IEC limit in terms of induced E-field is $E_{IEC} = 14.4$ V/m at $t_{s,eff} = 0.45$ ms. This value is 6-fold lower than the average E-field evaluated in the porcine heart at threshold ($E_{95} = 92.9$ V/m). A more detailed comparison of measured cardiac magnetostimulation thresholds with the IEC limit, which could potentially inform a correction thereof, requires threshold measurements at multiple stimulus durations. The CS measurements in the porcine experiments were limited to a single stimulus duration ($t_{s,eff} = 0.45$ ms) that was dictated by the capacitance and inductance of the magnetic stimulator and spiral coil.

Types of observed cardiac magnetostimulation effects

Four types of physiological outcomes were observed in the measurements for which an ECG trace was recorded in the pigs: lack of stimulation (i), cardiac capture followed by a compensatory pause (ii), capture without a compensatory pause (iii), and capture followed by a premature ventricular contraction (PVC) (iv). In all cases with successful capture, i. e., effects (ii)-(iv), stimulation occurred in the ventricles, as indicated by changes in R-wave morphology and premature T-waves with altered morphology on the ECG trace (the T-wave is caused by repolarization of the ventricles). Premature T-waves have also previously been observed in another magnetostimulation experiment on an open-chest canine (Andoh et al., 1994). Unfortunately, the single-lead ECG traces acquired in the porcine experiments do not allow a more detailed analysis of the stimulation site, e. g., whether the Purkinje fibers or the ventricular myocardium was stimulated first. It would be advantageous to have a more sophisticated electrode configuration in future experiments, such as a 12-lead ECG, which measures the heart's electrical potential on the body surface from twelve different angles. Such a measurement could help determine the origin and propagation direction of the depolarization wave following stimulation.

In stimulation mechanism (ii), the captured heartbeat often caused no or only small peaks in the blood pressure and oximetry signals (Figure 4.15). The lack of peaks in the hemodynamic signals was likely caused by the fact that the ventricles were captured, i. e., stimulated and contracted, before they were completely filled with blood. The next anterograde atrial conduction wave then reached the ventricles when they were still refractory from the stimulated beat, and was thus blocked,

which caused the absence of a heartbeat at the native RR interval, i. e., a compensatory pause. This pause extends the diastolic filling time of the ventricles and, consequently, when anterograde conduction of the next atrial conduction wave causes the ventricles to contract, it typically produces a large stroke volume and an increase in blood pressure.

Stimulation mechanism (iii) is similar to mechanism (ii), except that in these measurements, the EMP was applied later in the diastolic phase. The captured heartbeat was thus virtually superimposed to the next normal QRS complex. In this case, the stimulated capture was followed by no, or a very short, compensatory pause (Figure 4.16). It is also possible that in these cases, retrograde conduction occurred across the AV node, which could have reset the intrinsic pacemaker of the heart in the SA node. The stimulated pulses most likely did not result in isolated atrial capture since the abnormal morphology of the QRS complexes is not typical for atrial capture followed by aberrant AV-nodal conduction.

Finally, mechanism (iv) was only observed in pig #4 for EMPs applied on the T-wave with voltages >7.75 kV. In this case, cardiac capture was followed by a single intrinsic PVC on the ECG trace (Figure 4.17). This was the only case in which the EMP affected the heart for an additional heartbeat, causing a minor and temporary arrhythmia.

Magnetostimulation did not induce lasting cardiac arrhythmias

Beyond single PVCs, no cardiac arrhythmias were detected in any of the pigs with measured ECG traces. For the measurements that had no clean ECG traces, either due to EM interference with the measuring equipment or due to motion caused by skeletal muscle contractions, it was not possible to conclusively exclude the presence of arrhythmias. However, all animals remained hemodynamically stable after the pulse, i. e., the recorded blood pressure and oximetry traces showed no altered morphology or sustained altered rhythm. Importantly, no evidence of non-sustained ventricular tachycardia, ventricular couplets, or ventricular fibrillation was seen in any of the pigs. All of these conditions would likely have been visible on the hemodynamic traces alone. Aside from the visual inspection of cardiac activity on the ECG or hemodynamic traces, another method to detect lasting magnetostimulation-induced effects on the heart would be to measure troponin levels in the blood. Cardiac-specific troponin is a biomarker for myocardial damage such as infarction (Antman et al., 1996). Its measurement should thus be included in future experimental protocols.

Ventricular fibrillation (VF) is a particularly dangerous and life-threatening arrhythmia that can lead to cardiac arrest and sudden cardiac death (Baldzizhar et al., 2016). The ventricle is most sensitive to VF during repolarization (Reilly, 1992b), corresponding to the T-wave of the ECG signal. In the experiments, EMPs produced by charging voltages of up to 14.0 kV applied on the T-waves of pig #4 and #5 did not induce VF. Previous experiments determined the VF threshold of single electrode stimulation pulses to be approximately 50 times greater than for cardiac excitation (Antoni, 1998; Reilly, 2002). However, the margin between cardiac excitation and VF thresholds has not yet been investigated for magnetostimulation. The heart can get

more susceptible to VF when it is excited repeatedly during the vulnerable period of the cardiac cycle (Liu et al., 2003; Reilly, 1992b, 2002; Sugimoto et al., 1967). This is of particular concern for MRI gradient readout waveforms, which typically consist of trapezoidal pulse trains, i. e., repeated dB/dt pulses. The effect of repeated stimulations could not be investigated in the porcine experiments performed in this thesis due to the capacitors' long charging time compared to the cardiac cycle, and should be addressed in future work.

Dependence of the stimulation threshold on the cardiac cycle

In one of the pigs (#5), CS thresholds were measured at five different time points during the cardiac cycle (Figure 4.20). Stimulation in the form of cardiac capture could only be achieved during ventricular diastole. During systole, no stimulation could be achieved with capacitor charging voltages up to 13.0 kV, which corresponds to twice the diastolic stimulation threshold of pig #5. The finding that the CS threshold was higher during systole than during diastole is in alignment with a previous study that could only achieve magnetostimulation of the canine heart during diastole within the hardware limits of their experimental stimulation device (Yamaguchi et al., 1994). This phenomenon can be explained by the fact that the ventricular myocardium is refractory during ventricular systole. During this phase, it is either impossible (absolute refractory period) or at least more difficult (relative refractory period) to excite the myocardium (Antoni, 1998; Reilly, 1992b). For all other stimulation measurements performed in this work, the EMP was applied during the more vulnerable diastolic phase to obtain a conservative estimate of the CS threshold.

Stimulation of skeletal muscle by electromagnetic field pulses

Muscle contractions were observed in every measurement, even at the lowest charging voltage of $U_{min} = 2.0$ kV, which was substantially lower than the average porcine CS threshold of 6.3 kV. Previous canine experiments found that the threshold for the induction of skeletal muscle contractions by time-varying magnetic fields was ca. 9 times lower than the stimulation threshold of the heart (Bourland et al., 1991, 1999; Nyenhuis et al., 1991). Skeletal muscle contractions are most likely caused by stimulation of large peripheral motor nerves (Bourland et al., 1999), and can thus be seen as an indicator for PNS. This large margin between PNS and CS thresholds is in alignment with the simulations of MRI gradient-induced PNS and CS conducted in this thesis, and with previous theoretical work (Irnich, 1994). These findings support the conjecture that PNS thresholds are well below the CS thresholds, and preventing PNS is likely sufficient to prevent CS. This hypothesis will need to be verified for more stimulus waveforms and durations than the ones used in this work ($t_{s,eff} = 0.45$ ms) and in the previous canine experiments (Mouchawar et al., 1992; Nyenhuis et al., 1992). Most importantly, the hypothesis should be tested for long pulse durations of up to several milliseconds. The margin between CS and PNS thresholds has been suggested to decrease for such long pulse durations (IEC, 2010; Reilly, 1992b), an assumption that was confirmed by the CS model developed in this thesis.

Determination of the relationship between PNS and CS thresholds would thus be of great interest in future experiments. At the same time, it would be desirable to further reduce motion-induced artifacts on the physiological traces during measurements of the CS threshold. In the porcine experiments, vecuronium bromide, a potent muscle relaxant, was administered to the pigs to induce skeletal muscle paralysis. The agent was injected as a bolus in regular intervals of 20 min, and it thus had a limited half-life. In future experiments, vecuronium should be administered continuously as an infusion to increase its effectiveness. Another possibility to reduce muscle contractions would be to use a coil geometry that creates a more focused E-field in the heart region. The spiral coil used in the porcine experiments induced high E-field amplitudes in a large area of the torso, thus facilitating stimulation of adjacent muscle or nerve tissues.

Limitations of the experiments and future work

One of the primary goals of this work was to investigate the cardiac safety of MRI gradient systems. To this end, the dB/dt and E-field CS thresholds measured in pigs were compared to the peak values induced by MRI gradient systems in the human body. However, a significant limitation of this comparison is the assumption that porcine and human hearts have the same dB/dt or E-field thresholds. It has been established experimentally that pigs have a lower threshold for VF than humans or other mammals with comparable weights (Panescu et al., 2014). In particular, the porcine VF threshold was measured to be only 30% of the human VF threshold (Walcott et al., 2015). Pigs are, therefore, a conservative animal model for VF. Pacemaker, i. e., electrostimulation, thresholds measured in pigs were found to be on the lower end of pacemaker thresholds measured in human patients (Bowman and Hughes, 1984). As explained above, cardiac electrostimulation thresholds are influenced by many experimental parameters related to the electrodes (e. g., size, shape, and material), stimulus waveform (shape and pulse duration), and physiology (Bowman and Hughes, 1984). This variability makes it difficult to compare CS thresholds measured in different electrostimulation studies and thus to make definitive statements about the cardiac excitability of pigs compared to humans. Moreover, such a direct comparison is even more challenging for magnetostimulation experiments, which are difficult to perform in humans. A different, non-experimental, avenue to shed light on the relative cardiac magnetostimulation thresholds of pigs and humans would be to simulate the induced E-fields in models of the porcine and human anatomy coupled with models of the respective cardiac electrophysiology. A first step towards such a modeling-based extrapolation of the measured porcine thresholds to humans was done in the third part of this thesis.

Another difficulty in extrapolating the experiments to MRI gradient safety is that instead of a gradient coil, a flat spiral coil was used to excite the porcine heart. Whole-body gradient coils have a relatively large inductance (on the order of several hundred μH (Davids et al., 2020)), making it difficult to reach sufficiently high dB/dt values to induce CS within the current limits of state-of-the-art GPAs. This implicitly suggests that MRI gradient coils may be safe in terms of CS, but unfortunately also prohibits their use for cardiac magnetostimulation experiments. The flat spiral coil

used in the porcine experiments created a very different B-field, and thus induced E-field, pattern compared to a typical gradient coil.

A further difference between MRI experiments and the porcine study is the temporal waveform of the EMP used for stimulation, i. e., a damped sinusoid, which resulted from the capacitor discharges. The frequency of the damped sinusoid is in the range of typical MR gradient waveforms used in, e. g., EPI. However, the pulse shape is very different, which can affect the CS threshold. The stimulus frequency in the experiments was fixed by the capacitance and coil inductance. Future work could remedy this limitation by using several capacitance values to allow measurements over a wider range of frequencies, as has previously been done for CS measurements in canines (Yamaguchi et al., 1992). The shape of the capacitor-discharge pulse, on the other hand, is not easy to change. It would thus be advantageous to use a device capable of creating more general B-field waveforms, such as a GPA. However, simulations of several coil-amplifier combinations performed in this work showed that a standard GPA in combination with the spiral coil would likely not reach the cardiac dB/dt threshold.

This work investigated the B-field amplitude and dB/dt in the porcine heart at threshold as well as the expected (simulated) E-field. The former are useful threshold quantities because they can be easily estimated from the coil geometry and current waveform alone using Biot-Savart's law. The E-field, on the other hand, is more closely linked to the physical cause of tissue stimulation than dB/dt, but must be simulated in porcine and human models to allow a cross-species comparison. However, CS is not driven by the magnitude of the E-field alone, but rather by the tangential E-field component along the excitable tissue fibers, and in particular by the spatial derivative of this component (Knisley et al., 1999).

5.3 PREDICTING PORCINE CARDIAC MAGNETOSTIMULATION THRESHOLDS

In the third part of this thesis, cardiac magnetostimulation thresholds were simulated in individualized porcine body models corresponding to the animals used in the experimental study (Section 5.2). The main experimental parameters, such as anatomy and posture of the pig, the magnetic field waveform, and the relative position of the coil, were recorded in the experiments, allowing for an accurate replication of the experimental setup in the simulations.

Comparison of modeled and measured porcine CS thresholds

The eight MRI-based porcine models were equipped with geometrical descriptions of cardiac Purkinje and ventricular muscle fibers, both of which were coupled to the corresponding electrophysiological models. The modeling workflow described in the first part of this thesis was then used to predict CS thresholds in the porcine models for the E-fields matching the experimental setup, i. e., as induced by the damped sinusoidal magnetic field waveform created by the capacitor discharges into the spiral coil. The predicted thresholds show an overall very good agreement with the measured thresholds: The absolute prediction error averaged over all porcine

models is 18% when compared to measurements during early diastole, and 10% compared to measurements during late diastole.

The largest deviation between prediction and experiments was found for the first two pigs. In these cases, the predicted thresholds were around 50% higher than the measured thresholds, i. e., a substantially greater deviation compared to the maximum error in the other six porcine models (18%). This discrepancy is also apparent in the lower threshold E-fields found in the heart of these two pigs ($\approx$ 75 V/m compared to an average 98.9 ± 8.9 V/m in the remaining pigs). The comparatively low threshold E-field may be caused by corruptions in the porcine models of pigs #1 and #2. For pig #1, the heating blanket covering the animal during the stimulation experiment was not removed before the MRI scan. The water volume in this blanket generates a high signal intensity in the water-weighted Dixon images. Consequently, the segmentation process interpreted these regions as muscle tissue, which may have affected the overall predicted E-fields. For pig #2, the head was not completely captured in the MRI scan, thus reducing the body model's cross-sectional area and the overall induced E-field amplitude. Excluding pigs #1 and #2 from the analysis, the average absolute prediction error reduces to 7% when compared to measurements during early diastole, which is similar to the prediction error for late diastole.

The remaining mismatches between CS predictions and measurements may partly stem from an intra-individual variability of CS thresholds measured over the course of the experiments. Even though the average thresholds measured during early and late diastole are not significantly different, some intra-individual measurements showed a substantial variability in thresholds measured during both cardiac phases. Most notably, in pig #6 the threshold difference between early and late diastole was 2.37 kV, corresponding to a threshold variability of ca. 38%. This intra-individual variability may, e. g., have been caused by variations in the breathing cycle, as changing torso shape may affect the induced E-field. In the experiments, the capacitor discharge was not synchronized with the breathing cycle, and it is thus not known in which breathing phase the EMP was applied.

Sensitivity analysis of the cardiac threshold simulations

Some physiological details underlying the simulations may not perfectly match the individual pigs under study. For example, electrical tissue conductivity values or the ionic concentrations of, e. g., sodium or potassium in the porcine myocardium were not measured in the experiments. These parameters are known to fluctuate across individuals, and can affect CS threshold (Antoni, 1998; Liu et al., 2003). A preliminary sensitivity analysis was therefore conducted to assess the impact of variations in electrical tissue conductivity and the major electrophysiological parameters of the Purkinje fiber model on the predicted CS thresholds.

The sensitivity analysis also showed a strong impact of the myocardial tissue conductivity: A 50% reduction in myocardial conductivity led to a 41% increase in E-field and a 22% reduction in the CS threshold. Previous measurements of the electrical conductivity of the porcine heart found a minimum value of 0.31 S/m and a maximum of 0.44 S/m (Tsai et al., 2002). Varying the myocardial conductivity (based on the default value of 0.38 S/m (Hasgall et al., 2018)) by $\pm$50% is therefore likely

extreme and may provide a worst-case estimate of the CS threshold variability. The E-field in the heart also depended on the general muscle conductivity in the body (−16%/+11% variations for −50%/+50% changes of muscle conductivity). This is likely because the muscle compartment constitutes the largest tissue group in the porcine model by volume, therefore heavily influencing the overall induced E-field amplitude in the whole body. Surprisingly, the E-field in the heart and the predicted CS thresholds did not change significantly with variations of the lung conductivity, even though the lungs enclose a large portion of the heart. The sensitivity analysis also showed that the peak E-field in the heart does not necessarily correlate with the predicted CS threshold. For example, a 50% reduction in blood conductivity did not affect the 95th percentile E-field in the heart, but led to a decrease in predicted CS thresholds of 8%. This result again demonstrates that while the E-field is the driver behind activation of excitable tissue, the E-field magnitude itself is a poor surrogate for the quantitative CS threshold. Additionally, not every portion of the myocardium is populated with sensitive excitable tissue, meaning that an E-field hotspot in a region without excitable fibers may not lead to CS. For example, the subendocardial Purkinje fiber network is confined to a single layer beneath the endocardium, which makes the fibers insensitive to E-field changes in other areas of the heart.

For variations of the electrophysiological model parameters, the cell diameter had the largest impact on the CS thresholds: A 50% decrease in cell diameter caused a 35% increase in predicted threshold. Such an inverse correlation between the stimulation threshold and fiber diameter has also been found in previous PNS simulations (Davids et al., 2017) and experiments (Enoka, 2002). The largest threshold decrease (20%) was caused by a 50% increase in specific membrane capacitance. This dependence is also apparent in the basic Hodgkin-Huxley cable equation (Equation 2.111), where a change in membrane capacitance inversely correlates with the temporal rate of change of the TMV. Larger temporal changes of the TMV in turn result in a lower stimulation threshold for the same extracellular voltage applied along the fiber.

Future work should expand this analysis to investigate the effect of other biophysical and electrophysiological parameters, such as body temperature, electrolyte and ionic concentrations, as well as pathological fluctuations of these parameters. Such an in-depth analysis could help shed light on the inter- and intra-individual variability of CS thresholds.

Improvements of the porcine CS predictions and future work

While the good agreement between the measured and predicted porcine CS thresholds is encouraging, the work carried out in this thesis identified various aspects by which the CS modeling can be improved or extended.

One such example is the Purkinje fiber topology in the porcine heart models. Pigs have intramural Purkinje fibers that connect the endo- and epicardium (Lelovas et al., 2014). The algorithm employed in this thesis to add Purkinje fibers to body models only describes the subendocardial Purkinje fiber network (Ijiri et al., 2008). While this representation is accurate for humans and canines (Ono et al., 2009), intramural Purkinje fibers should be added to the porcine models in future work to assess their influence on the predicted CS threshold. Previous work demonstrated the subject-

specific generation of Purkinje fiber networks based on electro-anatomical maps (Barber et al., 2021). Although the fiber networks created with this method may be too sparse to accurately predict CS thresholds, they may be used to complement the network generation algorithm to obtain a more accurate depiction of the individual animals' Purkinje fiber anatomy.

In addition to the geometric differences in the Purkinje fiber networks, human and porcine hearts exhibit electrophysiological differences on a cellular level, e. g., in their potassium and calcium dynamics (Gaur et al., 2021). All simulations in this work utilized membrane models of human Purkinje cells (Stewart et al., 2009) and ventricular myocytes (O'Hara et al., 2011) to predict the cardiac response to induced E-fields. Recently, a dedicated model of the porcine ventricular cardiomyocyte was developed (Gaur et al., 2021), which could be included in the CS modeling framework for the porcine threshold predictions. Although a similar model for the porcine Purkinje cell membrane has not yet been developed (Gaur et al., 2021), the field of electrophysiological models is quickly evolving, and the CS modeling framework will be updated continuously as new models become available.

The modeling framework developed and validated in this thesis will play a central role in translating the CS thresholds measured in pigs to humans. This could be achieved by modeling CS in the human body for a similar experimental setup, i. e., the same magnetic field pattern and temporal waveform, as used in the porcine measurements. Such simulations would help shed light on differences in induced E-field distributions caused by differences in anatomy as well as electrophysiological responses to the induced E-fields. Furthermore, the induced E-fields and CS thresholds of the spiral coil should be compared to a variety of MRI gradient coils, including whole-body, head-only, and special purpose coils, as well as different gradient waveforms, using the electromagnetic-electrophysiological modeling tool developed and validated in this work.

6

CONCLUSION AND OUTLOOK

State-of-the-art MRI gradient hardware is increasingly constrained by safety hazards arising from potential cardiac stimulation (CS) by induced E-fields (magnetostimulation). Cardiac magnetostimulation thresholds cannot be safely measured in humans, making their quantitative and qualitative assessment extremely difficult. The IEC 60601-2-33 safety regulations to prevent CS in MRI were instead based on simple E-field calculations and electrode-based stimulation experiments in animals. These experiments showed a large variability in CS thresholds due to the inclusion of different species and multiple electrode positions and geometries. The lack of human cardiac magnetostimulation data and the difficulty of translating knowledge from other species to humans have required a conservative approach in defining safety limits by regulatory bodies. These limits can restrict gradient performance and therefore imaging speed and resolution, a situation that is expected to be more and more common as the performance of gradient systems continues to improve. Given the increasing relevance of cardiac safety in MRI, this thesis investigates the thresholds and mechanisms underlying CS by time-varying magnetic fields. This aim is approached in two ways: First, a coupled electromagnetic-electrophysiological model of cardiac magnetostimulation was used to investigate safe operational limits for MRI gradients, and second, the magnetostimulation threshold of the porcine heart was measured – for the first time – in an experimental in vivo study.

In the first part of this thesis, a modeling framework was developed to predict cardiac magnetostimulation thresholds using computational body models assigned with EM tissue properties in combination with models of electrically excitable fibers in the heart. Specifically, the body models were equipped with realistic depictions of the cardiac Purkinje and ventricular muscle fiber paths. The electrophysiological ion channel properties of individual cardiac cells and gap junction connections that make up the fibers were represented using equivalent electrical-circuit models. A preliminary model validation was performed by comparison with previously published measurements in canines. Despite unavoidable mismatches between the simulations and experiments, CS thresholds predicted in a generic canine body model matched the experimental thresholds with a maximum error of 28%. Building on these promising first results, CS thresholds were then simulated in male and female adult human body models placed in two commercial MRI gradient systems. The CS thresholds predicted for these systems were at least one order of magnitude higher than the IEC cardiac safety limit, indicating that this limit may be overly conservative. Furthermore, the predicted thresholds were >26 times higher than the hardware limits of the gradient systems. The simulations confirmed the expectation that the heart is much more difficult to stimulate by gradient-induced E-fields than peripheral nerves. The ratio between CS and peripheral nerve stimulation (PNS) thresholds ranged from 6 for gradient waveforms with long rise times (>2.5 ms) to 25 for short rise times (<0.5 ms). PNS may be uncomfortable but is harmless for the patient. The

large predicted margin between CS and PNS thus suggests that PNS may be used as a safe indicator of gradient-induced stimulation effects.

The modeling framework developed in this thesis can predict the thresholds as well as the sites of stimulation in the heart. For example, the Purkinje fibers in the model were always stimulated before the ventricular muscle fibers. Furthermore, it was shown that the stimulation of cardiac fibers depends on the relative orientation between the induced E-field and the fiber path. In particular, the excitability of the fibers correlated inversely with the spatial derivative of the E-field projection onto the fibers. The results presented in this thesis thus provide knowledge about both the threshold magnitude and the mechanisms of action of cardiac magnetostimulation, which may help inform appropriate safe operational limits for MRI gradients while fully exploiting the imaging system's performance. Moreover, the modeling tool could be used to understand the impact of different design parameters of novel gradient coils, such as non-cylindrical coil formers or asymmetrical wire geometries, on the CS threshold. Ultimately, the model could help design gradient coils with an inherently low CS propensity, e. g., by optimizing the magnitude and orientation of the E-field induced in the heart. Finally, the CS modeling framework could become valuable for studying the MRI compatibility of cardiac pacemakers and other implants such as stents, which are known to increase the amplitude of gradient-induced E-fields in the heart region, thus increasing the risk for CS.

The second part of this thesis measured CS thresholds in ten healthy, anesthetized pigs using EMPs created by capacitor discharges into an inductive coil. Despite pigs having become the primary animal model of the human cardiovascular system, this study is the first to measure cardiac magnetostimulation thresholds in the porcine heart. In the experiments, a capacitor bank was discharged into a flat spiral coil placed close to the porcine chest, resulting in a damped sinusoidal magnetic field pulse. The amplitude of the magnetic field pulse, and correspondingly the peak E-field magnitude induced in the porcine heart, was proportional to the capacitor charging voltage. The voltage was varied to determine the threshold at which the heart showed an abnormal response to the EM pulse (such as an ectopic heartbeat). Successful CS was identified on ECG, blood pressure, and blood oximetry signals measured before, during, and after application of the EMP. The stimulation experiments were followed by whole-body MR Dixon and CINE image acquisitions for eight of the pigs to create computational body models of each animal's anatomy and posture. These body models were used to simulate the dB/dt and E-field induced in the heart for the capacitor discharge waveform that caused CS in the experiments. The average dB/dt threshold in the porcine heart resulting in CS was 1.66 ± 0.23 kT/s. The average E-field threshold in the porcine heart was 92.9 ± 13.5 V/m, a value that is similar to the E-field threshold determined previously in canines. This E-field is ~15-fold higher than the established stimulation threshold for peripheral nerves (6 V/m).

The average dB/dt threshold of the porcine heart was 11-fold higher than the IEC cardiac safety limit. Assuming similar CS thresholds for humans and pigs, this result again indicates that the IEC limit may be overly conservative for the EM field waveform and duration used in the experiments. Moreover, the average porcine dB/dt threshold was 31-fold higher, and the average E-field threshold was 37-fold higher

than the peak dB/dt and E-field values induced in the heart of a human body model by three commercial MRI gradient systems. These results suggest that these gradient systems operate well below the CS threshold for the investigated EMP waveform.

The measurements performed in this thesis add critical new data to the otherwise sparse body of data for cardiac magnetostimulation. Future experimental work should investigate the CS threshold dependence on the duration of the EMP, which could, e. g., be achieved by using coils with different inductance in combination with varying capacitances. Knowledge of the stimulus-duration dependence of CS thresholds would be valuable for the definition of safety limit for MRI gradient waveforms with different rise times.

The third part of this thesis combined the cardiac magnetostimulation thresholds measured in pigs in the second part with the modeling framework developed in the first part. To this end, the porcine body models derived from the acquired MR images were augmented with geometrical and electrophysiological descriptions of cardiac Purkinje and ventricular muscle fibers. The predicted CS thresholds showed a good agreement with the experimental thresholds. Specifically, the absolute simulation error averaged across all porcine models was 18% for threshold measurements during early diastole and 10% for measurements during late diastole. These results constitute the first in-depth comparison of numerically predicted and measured CS thresholds for individual animals. Their overall good agreement demonstrates the validity of the CS prediction model developed in this work for the experimental EMP waveform and duration. A well-validated CS modeling tool will allow translation of measurements obtained in an animal model like the pig to humans exposed to MRI gradient fields. Such a translation requires a careful comparison of the porcine and human anatomy and electrophysiology, which will be the subject of future work.

A preliminary sensitivity analysis showed that $\pm 50\%$ changes of the most important model parameters such as cardiac fiber diameter and electrical tissue conductivity caused a predicted threshold variation of less than 35%. This moderate threshold variability indicates some level of robustness of the CS predictions. The sensitivity analysis will be expanded in future work to include more EM and electrophysiological parameters to shed light on the physiological inter- and intra-individual variability of CS thresholds.

In summary, the numerical and experimental results presented in this thesis indicate that current MRI gradient systems are extremely unlikely to induce CS and that PNS may be an adequately conservative and safe indicator of gradient-induced stimulation effects. The experimental data in combination with the modeling framework developed and validated in this thesis lay the basis for a re-evaluation of regulatory safety limits to enable safe state-of-the-art MRI in humans.

A

APPENDIX

A.1 PUBLICATIONS

Parts of this thesis have been published in (Klein et al., 2021) and submitted to a peer-reviewed journal (Klein et al., 2022).

Peer-reviewed journal articles

[1] **V Klein,** M Davids, L R Schad, L L Wald, B Guérin. "Investigating cardiac stimulation limits of MRI gradient coils using electromagnetic and electrophysiological simulations in human and canine body models". In: *Magn. Reson. Med.* 85.2 (2021), pp. 1047-1061. (https://doi.org/10.1002/mrm.28472)

[2] **V Klein,** M Davids, L L Wald, L R Schad, B Guérin. "Sensitivity analysis of neurodynamic and electromagnetic simulation parameters for robust prediction of peripheral nerve stimulation". In: *Phys. Med. Biol.* 64 (2019), p. 015005. (https://doi.org/10.1088/1361-6560/aaf308)

[3] M Davids, B Guérin, **V Klein,** L L Wald. "Optimization of MRI gradient coils with explicit peripheral nerve stimulation constraints". In: *IEEE Trans. Med. Imag.* 40.1 (2021), pp. 129-142. (https://doi.org/10.1109/TMI.2020.3023329)

[4] M Davids, B Guérin, **V Klein,** M Schmelz, L R Schad, L L Wald. "Optimizing selective stimulation of peripheral nerves with arrays of coils or surface electrodes using a linear peripheral nerve stimulation metric". In: *J. Neural Eng.* 17 (2020), p. 016029. (https://doi.org/10.1088/1741-2552/ab52bd)

Journal article under review

[1] **V Klein,** J Coll-Font, L Vendramini, D Straney, M Davids, N G Ferris, L R Schad, D Sosnovik, C Nguyen, L L Wald, B Guérin. "Measurement of magnetostimulation thresholds in the porcine heart". Submitted to *Magn. Reson. Med.* in February 2022.

Conference contributions

[1] **V Klein,** M Davids, D Straney, L Vendramini, L R Schad, M van den Boomen, C Nguyen, L L Wald, B Guérin. "Device and simulation workflow for validating cardiac magneto-stimulation thresholds in porcine models". In: *Proceedings of the 29th Annual Meeting of the International Society for Magnetic Resonance in Medicine (ISMRM).* 2021, p. 2477.

[2] **V Klein,** M Davids, L R Schad, L L Wald, B Guérin. "Modeling of cardiac stimulation by externally applied electromagnetic fields". In: *Proceedings of the 22nd International Conference on Electromagnetics in Advanced Applications (ICEAA).* 2021, p. 215. (https://doi.org/10.1109/ICEAA52647.2021.9539844)

[3] **V Klein,** M Davids, C Nguyen, L R Schad, L L Wald, B Guérin. "Feasibility of using transcranial magnetic stimulation devices to study magnetically induced cardiac stimulation in pigs". In: *Proceedings of the 28th Annual Meeting of the ISMRM.* 2020, p. 111.

[4] **V Klein,** M Davids, L R Schad, L L Wald, B Guérin. "Simulation of electromagnetic cardiac stimulation: Valdiation in dogs and application to human threshold limits for MRI gradient coils". In: *Proceedings of the 28th Annual Meeting of the ISMRM.* 2020, p. 1125.

[5] **V Klein,** M Davids, L R Schad, L L Wald, B Guérin. "Simulation of MRI gradient-induced cardiac stimulation: Are the current safety regulations too conservative?". In: *Proceedings of the 27th Annual Meeting of the ISMRM.* 2019, p. 729.

[6] **V Klein,** M Davids, L R Schad, L L Wald, B Guérin. "Informing MRI safety using coupled electromagnetic and electrophysiological modeling of cardiac stimulation". In: *Proceedings of the ISMRM workshop on MR safety.* 2019, p. 18.

[7] **V Klein,** M Davids, L R Schad, L L Wald, B Guérin. "Coupled electromagnetic and electrophysiological modeling of cardiac stimulation in MRI: Preliminary comparison with dog studies". In: *Proceedings of the 36th Annual Meeting of the European Society for Magnetic Resonance in Medicine and Biology (ESMRMB).* 2019, p. 1799.

[8] **V Klein,** M Davids, B Guérin, L R Schad, L L Wald. "Sensitivity analysis of peripheral nerve stimulation modeling: Which model parameters actually matter?". In: *Proceedings of the 26th Annual Meeting of the ISMRM.* 2018, p. 641.

[9] M Davids, P Dietz, G Ruyters, M Roesler, **V Klein,** B Guérin, D A Feinberg, L L Wald. "PNS optimization of a high-performance asymmetric gradient coil for head imaging". In: *Proceedings of the 29th Annual Meeting of the ISMRM.* 2021, p. 565.

[10] N G Ferris, M Davids, **V Klein,** B Guérin, L L Wald. "Exploiting nerve membrane dynamics to reduce peripheral nerve stimulation using asymmetric readout gradient waveforms". In: *Proceedings of the 29th Annual Meeting of the ISMRM.* 2021, p. 410.

[11] S Littin, T Kuder, F Jia, A Magill, P Amrein, F Laun, S Bicklehaupt, M Davids, **V Klein,** M Ladd, M Zaitsev. "Approaching order of magnitude increase of gradient strength: Non-linear breast gradient coil for diffusion encoding". In: *Proceedings of the 29th Annual Meeting of the ISMRM.* 2021, p. 3096.

[12] M Davids, B Guérin, **V Klein,** L R Schad, L L Wald. "The PNS oracle: A modified neural activation function metric for rapid assessment of peripheral nerve stimulation (PNS)". In: *Proceedings of the 27th Annual Meeting of the ISMRM.* 2019, p. 726.

[13] M Davids, B Guérin, **V Klein,** L R Schad, L L Wald. "Simulation of peripheral nerve stimulation thresholds of MRI gradient coils". In: *Proceedings of the 26th Annual Meeting of the ISMRM.* 2018, p. 4175.

A.2 TABLES

The following Table A.1 reports dB/dt and E-field values simulated in the porcine heart and scaled to match the stimulation threshold measured during late ventricular diastole. Table A.2 lists the maximum dB/dt and E-field values induced in the heart of a human body model by three gradient systems (heart at isocenter).

Table A.1: Magnetic field amplitude and rate (B-field and dB/dt) and 95th percentile electric field values (E_{95}) simulated in the heart of the porcine body models. All values were scaled to match the experimental threshold for stimulation during late diastole. For pigs #1 and #2, the traces measured during late diastole were inconclusive, and were thus excluded from the threshold analysis. For pigs #5 and #6, no MR images were acquired and thus no body models could be created. For these animals, the magnetic field was instead evaluated at a single point 11 cm above the coil center, which was the average coil-heart distance in the other pigs.

Pig	|B|-field [T] *at heart center*	dB/dt [T/s] *at heart center*	dB/dt [T/s] *mean in the heart*	dB/dt [T/s] *min. in the heart*	dB/dt [T/s] *max. in the heart*	dB/dt [T/s] *max. in the body*	E_{95} [V/m] *in the heart*
1	–	–	–	–	–	–	–
2	–	–	–	–	–	–	–
3	0.47	2240	2240	1380	3530	7260	106.7
4	0.37	1770	1840	1040	3220	6330	102.5
5	0.27	1290	No MRI	No MRI	No MRI	No MRI	No MRI
6	0.40	1880	No MRI	No MRI	No MRI	No MRI	No MRI
7	0.27	1310	1350	780	2450	4360	87.5
8	0.34	1620	1620	920	3040	5320	96.3
9	0.33	1590	1600	930	2930	4870	91.8
10	0.30	1460	1460	850	2680	4880	86.0
Mean $\pm$ SD	0.34 ± 0.07	1650 ± 320	1690 ± 320	980 ± 210	2980 ± 380	5500 ± 1090	95.1 ± 8.3

Table A.2: Maximum dB/dt and E-field values generated by three commercial gradient systems within the respective gradient hardware limits corresponding to an effective stimulus duration $t_{s,eff} = 0.45$ ms. The dB/dt values were evaluated within a cylinder with 0.2-m radius along the z-direction (IEC definition IEC, 2010), and in the heart of a male body model placed with its heart at isocenter.

Gradient system	Coil axis	Max. dB/dt [T/s] *on 0.2-m radius cylinder*	dB/dt [T/s] *at heart center*	dB/dt [T/s] *mean in the heart*	dB/dt [T/s] *min. in the heart*	dB/dt [T/s] *max. in the heart*	E_{95} [V/m] *in the heart*
Sonata	X-axis	55.7	3.0	6.1	0.1	13.9	0.32
	Y-axis	54.5	3.6	8.2	0.1	16.5	0.80
	Z-axis	51.7	2.6	5.7	0.1	11.4	0.24
Quantum	X-axis	57.6	3.0	5.2	0.1	11.1	0.31
	Y-axis	57.3	3.4	6.6	0.1	13.6	0.66
	Z-axis	50.6	2.8	5.0	0.3	10.5	0.20
Connectome	X-axis	53.8	5.3	8.5	0.1	18.2	0.50
	Y-axis	53.5	5.7	9.7	0.2	20.6	0.82
	Z-axis	58.2	5.7	8.8	0.9	19.2	0.39

BIBLIOGRAPHY

Abart, J, K Eberhardt, H Fischer, W Huk, E Richter, F Schmitt, T Storch, and E Zeitler (1997). "Peripheral nerve stimulation by time-varying magnetic fields." In: *J. Comput. Assist. Tomogr.* 21.4, pp. 532–538.

Amuzescu, B, R Airini, F B Epureanu, S A Mann, T Knott, and B M Radu (2021). "Evolution of mathematical models of cardiomyocyte electrophysiology." In: *Math. Biosci.* 334, p. 108567.

Andoh, T, A Hosono, M Yamaguchi, T Kawakami, and F Okumura (1994). "Arrhythmias induced by pulsed magnetic fields." In: *Med. Biol. Eng. Comput.* 32, pp. 16–18.

Antman, E M et al. (1996). "Cardiac-specific troponin I levels to predict the risk of mortality in patients with acute coronary syndromes." In: *N. Engl. J. Med.* 335, pp. 1342–1349.

Antoni, H (1998). "Electrical properties of the heart." In: *Applied bioelectricity*. Ed. by J P Reilly. New York: Springer, pp. 148–193.

Argentieri, T M, L H Frame, and T J Colatsky (1990). "Electrical properties of canine subendocardial Purkinje fibers surviving in 1-day-old experimental myocardial infarction." In: *Circ. Res.* 66.1, pp. 123–134.

Azarov, J E, M M Demidova, S Koul, J van der Pals, D Erlinge, and P G Platonov (2018). "Progressive increase of the T peak-T end interval is associated with ischaemia-induced ventricular fibrillation in a porcine myocardial infarction model." In: *Europace* 20, pp. 880–886.

Baldzizhar, A, E Manuylova, R Marchenko, Y Kryvalap, and M G Carey (2016). "Ventricular tachycardias: Characteristics and management." In: *Crit. Care Nurs. Clin. North Am.* 28.3, pp. 317–329.

Barber, F, P Langfield, M Lozano, I Garcia-Fernandez, J Duchateau, M Hocini, M Haissaguerre, E Vigmond, and R Sebastian (2021). "Estimation of personalized minimal Purkinje systems from human electro-anatomical maps." In: *IEEE Trans. Med. Imaging* 40.8, pp. 2182–2194.

Baumann, G, M Puderbach, M Deimling, V Jellus, C Chefd'hotel, J Dinkel, C Hintze, H U Kauczor, and L R Schad (2009). "Non-contrast-enhanced perfusion and ventilation assessment of the human lung by means of Fourier decomposition in proton MRI." In: *Magn. Reson. Med.* 62, pp. 656–664.

Bayer, J D, R C Blake, G Plank, and N A Trayanova (2012). "A novel rule-based algorithm for assigning myocardial fiber orientation to computational heart models." In: *Ann. Biomed. Eng.* 40.10, pp. 2243–2254.

Bieri, O and K Scheffler (2013). "Fundamentals of balanced steady state free precession MRI." In: *J. Magn. Reson. Imaging* 38, pp. 2–11.

Blair, H A (1932). "On the intensity-time relations for stimulation by electric currents I." In: *J. Gen. Physiol.* 15.6, pp. 709–729.

Bloch, F (1946). "Nuclear induction." In: *Phys. Rev.* 70.7-8, pp. 460–474.

Bourland, J D, J A Nyenhuis, G A Mouchawar, L A Geddes, D J Schaefer, and M E Riehl (1991). "Z-gradient coil eddy-current stimulation of skeletal and cardiac muscle in the dog." In: *Proceedings of the 10th Annual Meeting of the SMRM*. San Francisco, USA, p. 969.

Bourland, J D, J A Nyenhuis, and D J Schaefer (1999). "Physiologic effects of intense MR imaging gradient fields." In: *Neuroimaging Clin. N. Am.* 9.2, pp. 363–377.

Bowman, T A and H C Hughes (1984). "Swine as an in vivo model for electrophysiologic evaluation of cardiac pacing parameters." In: *PACE* 7, pp. 187–194.

Bowtell, R and R M Bowley (2000). "Analytic calculations of the E-fields induced by time-varying magnetic fields generated by cylindrical gradient coils." In: *Magn. Reson. Med.* 44, pp. 782–790.

Boyden, P A, M Hirose, and W Dun (2010). "Cardiac Purkinje cells." In: *Heart Rhythm* 7.1, pp. 127–135.

Boyle, P M, M Deo, G Plank, and E Vigmond (2010). "Purkinje-mediated effects in the response of quiescent ventricles to defibrillation shocks." In: *Ann. Biomed. Eng.* 38.2, pp. 456–468.

Brandt, J, R Attewell, T Fahraeus, and H Schüller (1990). "Atrial and ventricular stimulation threshold development: A comparative study in patients with a DDD pacemaker and two identical carbon-tip leads." In: *Pacing Clin. Electrophysiol.* 13.7, pp. 859–866.

Budinger, T F, H Fischer, D Hentschel, H-E Reinfelder, and F Schmitt (1991). "Physiological effects of fast oscillating magnetic field gradients." In: *J. Comput. Assist. Tomogr.* 16.6, pp. 909–914.

Carew, T E and J W Covell (1979). "Fiber orientation in hypertrophied canine left ventricle." In: *Am. J. Physiol. Heart Circ. Physiol.* 236.3, H487–H493.

Chronik, B A and B K Rutt (2001). "A comparison between human magnetostimulation thresholds in whole-body and head/neck gradient coils." In: *Magn. Reson. Med.* 46, pp. 386–394.

Clauss, S, C Bleyer, D Schüttler, P Tomsits, S Renner, N Klymiuk, R Wakili, S Massberg, E Wolf, and S Kääb (2019). "Animal models of arrhythmia: Classic electrophysiology to genetically modified large animals." In: *Nat. Rev. Cardiol.* 16, pp. 457–475.

Coates, S and B Thwaites (2000). "The strength-duration curve and its importance in pacing efficiency: A study of 325 pacing leads in 229 patients." In: *PACE* 23, pp. 1273–1277.

Cohen, M S, R M Weisskoff, R R Rzedzian, and H L Kantor (1990). "Sensory stimulation by time-varying magnetic fields." In: *Magn. Reson. Med.* 14, pp. 409–414.

Crick, S J, M N Sheppard, S Y Ho, L Gebstein, and R H Anderson (1998). "Anatomy of the pig heart: Comparisons with normal human cardiac structure." In: *J. Anat.* 193, pp. 105–119.

Damadian, R (1971). "Tumor detection by nuclear magnetic resonance." In: *Science* 171, pp. 1151–1153.

Damadian, R, M Goldsmith, and L Minkoff (1977). "NMR in cancer: XVI. Fonar image of the live human body." In: *Physiol. Chem. & Phys.* 9.1, pp. 97–100.

Daube, J R (2012). "Nerve conduction studies." In: *Electrodiagnosis in Clinical Neurology*. Ed. by Aminoff M J. 6th edition. Churchill Livingstone: Elsevier Inc., pp. 229–264.

Davids, M, B Guérin, A vom Endt, L R Schad, and L L Wald (2019a). "Prediction of peripheral nerve stimulation thresholds of MRI gradient coils using coupled electromagnetic and neurodynamic simulations." In: *Magn. Reson. Med.* 81, pp. 686–701.

Davids, M, B Guérin, V Klein, and L L Wald (2020). "Optimization of MRI gradient coils with explicit peripheral nerve stimulation constraints." In: *IEEE Trans. Med. Imaging* 40.1, pp. 129–142.

Davids, M, B Guérin, M Malzacher, L R Schad, and L L Wald (2017). "Predicting magnetostimulation thresholds in the peripheral nervous system using realistic body models." In: *Sci. Rep.* 7.

Davids, M, B Guérin, L R Schad, and L L Wald (2019b). "Peripheral nerve stimulation modeling for MRI." In: *eMagRes* 8, pp. 87–102.

Davids, M, B Guérin, L L Wald, and L R Schad (2018). "Automatic generation of topologically correct, high quality, finite-element tetrahedral body models from voxel and surface data." In: *Proceedings of the Joint Annual Meeting ISMRM-ESMRMB*. Paris, France, p. 4176.

De Almeida, M C, F Lopes, P Fontes, F Barra, R Guimaraes, and V Vilhena (2015). "Ungulates heart model: A study of the Purkinje network using India ink injection, transparent specimens and computer tomography." In: *Anat. Sci. Int.* 90, pp. 240–250.

Dhar, S K, K J Heston, L J Madrak, B K Shah, F T Deger, and R M Greenberg (2009). "Strength duration curve for left ventricular epicardial stimulation in patients undergoing cardiac resynchronization therapy." In: *PACE* 32, pp. 1146–1151.

Dixon, J A and F G Spinale (2009). "Large animal models of heart failure." In: *Circ.* 2.3, pp. 262–271.

Dixon, W T (1984). "Simple proton spectroscopic imaging." In: *Radiology* 153, pp. 189–194.

Dössel, O, M W Krueger, F M Weber, M Wilhelms, and G Seemann (2012). "Computational modeling of the human atrial anatomy and electrophysiology." In: *Med. Biol. Eng. Comput.* 50, pp. 773–799.

Elahi, B, B Elahi, and R Chen (2009). "Effect of Transcranial Magnetic Stimulation on Parkinson motor function - Systematic review of controlled clinical trials." In: *Mov. Disord.* 24.3, pp. 357–363.

Enoka, R M (2002). "Activation order of motor axons in electrically evoked contractions." In: *Muscle Nerve* 25, pp. 763–764.

Fabbri, A, M Fantini, R Wilders, and S Severi (2017). "Computational analysis of the human sinus node action potential: Model development and effects of mutations." In: *J. Physiol.* 595.7, 2365–2396.

Feldman, R E, C J Hardy, B Aksel, J Schenck, and Chronik B A (2009). "Experimental determination of human peripheral nerve stimulation thresholds in a 3-axis planar gradient system." In: *Magn. Reson. Med.* 62, pp. 763–770.

Ferris, N G, V Klein, B Gu'erin, L L Wald, and M Davids (2022). "Influence of electric field and axon geometry on peripheral nerve stimulation chronaxie." In: *submitted to Proceedings of the Joint Annual Meeting ISMRM-ESMRMB*. London, UK.

Fitzsimmons, S, Y D van der Werf, A D van Campen, M Arns, A T Sack, A W Hoogendoorn, Tetro consortium, and O A van den Heuvel (2022). "Repetitive transcranial magnetic stimulation for obsessive-compulsive disorder: A systematic review and pairwise/network meta-analysis." In: *J. Affect. Disord.*

Freitas, C, H Mondragón-Llorca, and A Pascual-Leone (2011). "Noninvasive brain stimulation in Alzheimer's disease: Systematic review and perspectives for the future." In: *Exp. Gerontol.* 46, pp. 611–627.

Gabriel, S, R W Lau, and C Gabriel (1996a). "The dielectric properties of biological tissues: II. Measurements in the frequency range 10 Hz to 20 GHz." In: *Phys. Med. Biol.* 41, pp. 2251–2269.

— (1996b). "The dielectric properties of biological tissues: III. Parametric models for the dielectric spectrum of tissues." In: *Phys. Med. Biol.* 41, pp. 2271–2293.

Garcia-Bustos, V, R Sebastian, M Izquierdo, P Molina, F J Chorro, and A Ruiz-Sauri (2017). "A quantitative structural and morphometric analysis of the Purkinje network and the Purkinje-myocardial junctions in pig hearts." In: *J Anat* 230, pp. 664–678.

Gaur, N, X Y Qi, D Benoist, O Bernus, R Coronel, S Nattel, and E J Vigmond (2021). "A computational model of pig ventricular cariomyocyte electrophysiology and calcium handling: Translation from pig to human electrophysiology." In: *PLoS Comput. Biol.* 17.6, e1009137.

Geddes, L A and J D Bourland (1985a). "The strength-duration curve." In: *IEEE Trans. Biomed. Eng.* 32.6, pp. 458–459.

— (1985b). "Tissue stimulation: Theoretical considerations and practical applications." In: *Med. Biol. Eng. Comput.* 23, pp. 131–137.

Gerlach, W and O Stern (1922). "Der experimentelle Nachweis der Richtungsquantelung im Magnetfeld." In: *Z. Physik* 9, pp. 349–352.

Grandi, E, S V Pandit, N Voigt, A J Workman, D Dobrev, J Jalife, and D M Bers (2011). "Human atrial action potential and Ca2+ model: Sinus rhythm and chronic atrial fibrillation." In: *Circ. Res.* 109, pp. 1055–1066.

Haacke, E M, R W Brown, M R Thompson, and R Venkatesan (1999). *Magnetic Resonance Imaging: Physical principles and sequence design*. Hoboken, NJ, USA: John Wiley & Sons, Inc.

Hahn, E L (1950). "Spin echoes." In: *Phys. Rev.* 80.4, pp. 580–594.

Hallett, M (2000). "Transcranial Magnetic Stimulation and the human brain." In: *Nature* 406, pp. 147–150.

Han, W, W Bao, Z Wang, and S Nattel (2002a). "Comparison of ion-channel subunit expression in canine cardiac Purkinje fibers and ventricular muscle." In: *Circ. Res.* 91, pp. 790–797.

Han, W, Z Wang, and S Nattel (2000). "A comparison of transient outward currents in canine cardiac Purkinje cells and ventricular myocytes." In: *Am. J. Physiol. Heart Circ. Physiol.* 279, H466–H474.

Han, W, L Zhang, G Schram, and S Nattel (2002b). "Properties of potassium currents in Purkinje cells of failing human hearts." In: *Am. J. Physiol. Heart Circ. Physiol.* 283, H2495–H2503.

Harvey, R D and A O Grant (2018). "Agents used in cardiac arrhythmias." In: *Basic and clinical pharmacology*. Ed. by B G Katzung. 14th ed. New York, USA: McGraw-Hill Education, p. 229.

Hasgall, P A, F Di Gennaro, C Baumgartner, M C Gosselin, D Payne, A Klingenböck, and N Kuster (2018). *IT'IS Database for thermal and electromagnetic parameters of biological tissues Version 4.0*.

Hodgkin, A L and A F Huxley (1952). "A quantitative description of membrane current and its application to conduction and excitation in nerve." In: *J. Physiol.* 117, pp. 500–544.

Huang, S Y et al. (2021). "Connectome 2.0: Developing the next-generation ultra-high gradient strength human MRI scanner for bridging studies of the micro-, meso- and macro-connectome." In: *NeuroImage* 243, p. 118530.

Hund, T J and Y Rudy (2004). "Rate dependence and regulation of action potential and calcium transient in a canine cardiac ventricular cell model." In: *Circ.* 110, pp. 3168–3174.

IEC (2010). *International standard IEC 60601 medical electrical equipment. Part 2-33: Particular requirements for the basic safety and essential performance of magnetic resonance equipment for medical diagnosis*. Tech. rep. International Electrotechnical Commission (IEC).

Ijiri, T, T Ashihara, T Yamaguchi, K Takayama, T Igarashi, T Shimada, T Namba, R Haraguchi, and K Nakazawa (2008). "A procedural method for modeling the Purkinje fibers of the heart." In: *J Physiol. Sci.* 58.7, pp. 481–486.

Inada, S, J C Hancox, H Zhang, and M R Boyett (2009). "One-dimensional mathematical model of the atrioventricular node including atrio-nodal, nodal, and nodal-His cells." In: *Biophys. J.* 97, pp. 2117–2127.

Irnich, W (1994). "Electrostimulation by time-varying magnetic fields." In: *MAGMA* 2, pp. 43–49.

— (2008). "The hyperbolic strength-duration relationship of defibrillation threshold." In: *IEEE Trans. Biomed. Eng.* 55.8, pp. 2057–2063.

Irnich, W and F Schmitt (1995). "Magnetostimulation in MRI." In: *Magn. Reson. Med.* 33, pp. 619–623.

Izhikevich, E M (2007). *Dynamical systems in neuroscience: The geometry of excitability and bursting*. Cambridge, Massachusetts: The MIT press.

Jaeger, K H, A G Edwards, W R Giles, and A Tveito (2021). "From millimeters to micrometers; Re-introducing myocytes in models of cardiac electrophysiology." In: *Front. Physiol.* 12, p. 763584.

Jia, F, S Littin, P Amrein, H Yu, A W Magill, T A Kuder, S Bickelhaupt, F Laun, M E Ladd, and M Zaitsev (2021). "Design of a high-performance non-linear gradient coil for diffusion weighted MRI of the breast." In: *JMRI.*

Keener, J and J Sneyd (2009). *Mathematical physiology - I: Cellular physiology*. 2nd ed. Vol. 8/1. Interdisciplinary applied mathematics. New York: Springer-Verlag New York.

Klein, V, M Davids, L R Schad, L L Wald, and B Guérin (2021). "Investigating cardiac stimulation limits of MRI gradient coils using electromagnetic and electrophysiological simulations in human and canine body models." In: *Magn. Reson. Med.* 85, 1047–1061.

Klein, V, M Davids, L L Wald, L R Schad, and B Guérin (2019). "Sensitivity analysis of neurodynamic and electromagnetic simulation parameters for robust prediction of peripheral nerve stimulation." In: *Phys. Med. Biol.* 64, p. 015005.

Klein, V et al. (2022). "Measurement of magnetostimulation thresholds in the porcine heart." In: *Magn. Reson. Med.* submitted in February 2022.

Kleinert, M P, H R Bartsch, and K G Mühlenpfordt (1983). "Comparative studies of ventricular and atrial stimulation thresholds of carbon-tip electrodes." In: *Cardiac Pacing*. Ed. by K Steinbach. Heidelberg: Steinkopff, pp. 353–359.

Knisley, S B, N A Trayanova, and F Aguel (1999). "Roles of electric field and fiber structure in cardiac electric stimulation." In: *Biophys. J.* 77, pp. 1404–1417.

Kramer, G H, K Capello, S Strocchi, B Bearrs, K Leung, and N Martinez (2012). "The HML's new voxel phantoms: Two human males, one human female, and two male canines." In: *Health Phys. Soc.* 103.6, pp. 802–807.

Lapicque, L (1909). "Definition expérimentale de l'excitabilité." In: *Comptes Rendus Acad. Sci.* 67.2, pp. 208–283.

Lauterbur, P C (1973). "Image formation by induced local interactions: Examples employing NMR." In: *Nature* 242, pp. 190–191.

Le Bihan, D and E Breton (1985). "Imagerie de diffusion in vivo par résonance magnétique nucléaire." In: *C. R. Acad. Sci.* 301.15, pp. 1109–1112.

Lee, S K et al. (2016). "Peripheral nerve stimulation characteristics of an asymmetric head-only gradient coil compatible with a high-channel-count receiver array." In: *Magn. Reson. Med.* 76, 1939–1950.

Legato, M J (1973). "Ultrastructure of the atrial, ventricular, and Purkinje cell, with special reference to the genesis of arrhythmias." In: *Circ.* 47, pp. 178–189.

Lelovas, P P, N G Kostomitsopoulos, and T T Xanthos (2014). "A comparative anatomic and physiologic overview of the porcine heart." In: *J. Am. Assoc. Lab. Anim. Sci.* 53.5, pp. 432–438.

Lepeschkin, E, J L Jones, S Rush, and R E Jones (1978). "Local potential gradient as a unifying measure for thresholds of stimulation standstill, tachyarrhythmia and fibrillation appearing after strong capacitor dischargees." In: *Adv. Cardiol.* 21, pp. 268–278.

Li, H G, D L Jones, R Yee, and G J Klein (1993). "Defibrillation shocks produce different effects on Purkinje fibers and ventricular muscle: Implications for successful defibrillation, refibrillation and postshock arrhythmia." In: *J. Am. Coll. Cardiol.* 22, pp. 607–614.

Lin, J and J P Keener (2010). "Modeling electrical activity of myocardial cells incorporating the effects of ephaptic coupling." In: *PNAS* 107.49, 20935–20940.

Listerud, J, S Einstein, E Outwater, and H Y Kressel (1992). "First principles of fast spin echo." In: *Magn. Reson. Q.* 8.4, pp. 199–244.

Littin, S et al. (2021). "Approaching order of magnitude increase of gradient strength: Non-linear breast gradient coil for diffusion encoding." In: *Proceedings of the 29th Annual Meeting of the ISMRM*, p. 3096.

Liu, F, L Xia, and S Crozier (2003). "Influence of magnetically-induced E-fields on cardiac electric activity during MRI: A modeling study." In: *Magn. Reson. Med.* 50, pp. 1180–1188.

Lloyd, C M, J L Lawson, P J Hunter, and P F Nielsen (2008). "The CellML Model Repository." In: *Bioinformatics* 24.18, pp. 2122–2123.

Logothetis, N K (2008). "What we can and what we cannot do with fMRI." In: *Nature* 453, 869–878.

Lohr, F, M Essig, M Bock, H Oster, F Wenz, and M V Knopp (1999). "Ventricular arrhythmia during MR angiography with fast ramping gradients in a patient with multiple coronary artery bypass grafts (CABG)." In: *Magn. Reson. Med.* 9, pp. 624–626.

Lu, W and L Xia (1996). "Computer simulation of epicardial potentials using a heart-torso model with realistic geometry." In: *IEEE Trans. Biomed. Eng.* 43.2, pp. 211–217.

Lövsund, P, P A Öberg, S E G Nilsson, and T Reuter (1980). "Magnetophosphenes: A quantitative analysis of thresholds." In: *Med. Biol. Eng. Comput.* 18, pp. 326–334.

Magnusson, C E and H C Stevens (1911). "Visual sensations caused by changes in the strength of a magnetic field." In: *Am. J. Physiol.* 29, pp. 124–136.

Mansfield, P and P K Grannell (1973). "NMR 'diffraction' in solids?" In: *J. Phys. C: Solid State Phys.* 6, p. L422.

Mansfield, P and P R Harvey (1993). "Limits to neural stimulation in echo-planar imaging." In: *Magn. Reson. Med.* 29, pp. 746–758.

Mansfield, P and A A Maudsley (1977). "Planar spin imaging by NMR." In: *J. Magn. Reson.* 27, pp. 101–119.

Matheny, R G and C J Shaar (1997). "Vagus nerve stimulation as a method to temporarily slow or arrest the heart." In: *Ann. Thorac. Surg.* 63.6, pp. 28–29.

McIntyre, C C, A G Richardson, and W M Grill (2002). "Modeling the excitability of mammalian nerve fibers: Influence of afterpotentials on the recovery cycle." In: *J. Neurophysiol.* 87, pp. 995–1006.

McNab, J A et al. (2013). "The Human Connectome Project and beyond: Initial application of 300 mT/m gradients." In: *NeuroImage* 80, pp. 234–245.

McNeal, D R (1976). "Analysis of a model for excitation of myelinated nerve." In: *IEEE Trans. Biomed. Eng.* 23.4, pp. 329–337.

Merideth, J, C Mendez, W J Mueller, and G K Moe (1968). "Electrical excitability of atrioventricular nodal cells." In: *Circ. Res.* 23, pp. 69–85.

Mogyoros, I, M C Kiernan, and D Burke (1996). "Strength-duration properties of human peripheral nerve." In: *Brain* 119, pp. 439–447.

Molendowska, M, F Fasano, U Rudrapatna, R Kimmlingen, D K Jones, S Kusmia, C M W Tax, and C J Evans (2021). "Physiological effects of human body imaging with 300 mT/m gradients." In: *Magn. Reson. Med.* 00, pp. 1–9.

Mouchawar, G A, J D Bourland, J A Nyenhuis, L A Geddes, K S Foster, J T Jones, and G P Graber (1992). "Closed-chest cardiac stimulation with a pulsed magnetic field." In: *Med. Biol. Eng. Comput.* 30, pp. 162–168.

Mouchawar, G A, L A Geddes, J D Bourland, and J A Pearce (1989). "Ability of the Lapicque and Blair strength-duration curves to fit experimentally obtained data from the dog heart." In: *IEEE Trans. Biomed. Eng.* 36.9, pp. 971–974.

Mouchawar, G A, J A Nyenhuis, J D Bourland, L A Geddes, D J Schaefer, and M E Riehl (1993). "Magnetic stimulation of excitable tissue: Calculation of induced eddy-currents with a three-dimensional finite-element model." In: *IEEE Trans. Magn.* 29.6, pp. 3355–3357.

Nguyen, C, Z Fan, B Sharif, Y He, R Dharmakumar, D S Berman, and D Li (2014). "In vivo three-dimensional high resolution cardiac diffusion-weighted MRI: A motion compensated diffusion-prepared balanced steady-state free precession approach." In: *Magn. Reson. Med.* 72, pp. 1257–1267.

Niederer, S A, J Lumens, and N A Trayanova (2018). "Computational models in cardiology." In: *Nat. Rev. Cardiol.* 16, pp. 100–111.

Nyenhuis, J A, J D Bourland, G A Mouchawar, T Z Elabbady, L A Geddes, D J Schaefer, and M E Riehl (1991). "Comparison of stimulation effects of longitudinal and transverse MRI gradient coils." In: *Proceedings of the 10th Annual Meeting of the SMRM*. San Francisco, CA, USA, p. 1275.

Nyenhuis, J A, J D Bourland, D J Schaefer, K S Foster, W E Schoelein, G A Mouchawar, T Z Elabbady, L A Geddes, and M E Riehl (1992). "Measurement of cardiac stimulation thresholds for pulsed z-gradient fields in a 1.5-T magnet." In: *Proceedings of the 11th Annual Meeting of the SMRM*. Berlin, Germany, p. 586.

Nyenhuis, J A and D Gross (2019). "Effect of strong time-varying magnetic field gradients on humans." In: *eMagRes* 8, pp. 29–40.

Nyenhuis, J A et al. (1994). "Magnetic stimulation of the heart and safety issues in magnetic resonance imaging." In: *Biomagnetic stimulation*. Ed. by S Ueno. Boston, MA: Springer, pp. 75–89.

O'Hara, T, L Virág, A Varró, and Y Rudy (2011). "Simulation of the undiseased human cardiac ventricular action potential: Model formulation and experimental validation." In: *PLoS Comput. Biol.* 7.5, e1002061.

Ono, N, T Yamaguchi, H Ishikawa, M Arakawa, N Takahashi, T Saikawa, and T Shimada (2009). "Morphological varieties of the Purkinje fiber network in mammalian hearts, as revealed by light and electron microscopy." In: *Arch. Histol. Cytol.* 72.3, pp. 139–149.

Panescu, D, M Kroll, and M Brave (2014). "Limitations of animal electrical cardiac safety models." In: *36th Annual International Conference of the IEEE Engineering in Medicine and Biology Society*. Chicago, IL, USA: IEEE, pp. 6483–6486.

Parker, J L, N H Shariati, and D M Karantonis (2018). "Electrically evoked compound action potential recording in peripheral nerves." In: *Bioelectron. Med.* 1.1, pp. 71–83.

Pastore, A P, A De Leo, R De Leo, G Della Chiara, V M Primiani, F Moglie, and G Cerri (2011). "A realistic model for the analysis of heart magnetic stimulation." In: *IEEE Trans. Biomed. Eng.* 58.2, pp. 291–300.

Pearce, J A, J D Bourland, W Neilsen, L A Geddes, and M Voelz (1982). "Myocardial stimulation with ultrashort duration current pulses." In: *PACE* 5, pp. 52–58.

Pelot, N A, D C Catherall, B J Thio, N D Titus, E D Liang, C S Henriquez, and W M Grill (2021). "Excitation properties of computational models of unmyelinated peripheral axons." In: *J. Neurophysiol.* 125.1, pp. 86–104.

Piersanti, R, P C Africa, M Fedele, C Vergara, L Dede, A F Corno, and A Quarteroni (2021). "Modeling cardiac muscle fibers in ventricular and atrial electrophysiology simulations." In: *Comput. Methods Appl. Mech. Engrg.* 373, p. 113468.

Plank, G et al. (2021). "The openCARP simulation environment for cardiac electrophysiology." In: *Comput. Methods Programs Biomed.* 208, p. 106223.

Purcell, E M, H C Torrey, and R V Pound (1946). "Resonance absorption by nuclear magnetic moments in a solid." In: *Phys. Rev.* 69.37, pp. 37–38.

Rabi, I I, J R Zacharias, S Millman, and P Kusch (1938). "A new method of measuring nuclear magnetic moments." In: *Phys. Rev.* 53.4, p. 318.

Ragan, P M, W Wang, and S R Eisenberg (1995). "Magnetically induced currents in the canine heart: A finite element study." In: *IEEE Trans. Biomed. Eng.* 42.11, pp. 1110–1116.

Rattay, F (1986). "Analysis of models for external stimulation of axons." In: *IEEE Trans. Biomed. Eng.* 33.10, pp. 974–977.

Reilly, J P (1985). "Sensory effects of transient electrical stimulation - Evaluation with a neuroelectric model." In: *IEEE Trans. Biomed. Eng.* 32.12, pp. 1001–1011.

— (1991). "Magnetic field excitation of peripheral nerves and the heart: A comparison of thresholds." In: *Med. Biol. Eng. Comput.* 29, pp. 571–579.

— (1992a). *Electrical stimulation and electropathology*. Cambridge: Cambridge University Press.

— (1992b). "Principles of nerve and heart excitation by time-varying magnetic fields." In: *Ann. N. Y. Acad. Sci.* 649, pp. 96–117.

— (1998). *Applied bioelectricity: From electrical stimulation to electropathology*. New York: Springer-Verlag New York, Inc.

— (2002). "Neuroelectric mechanisms applied to low frequency electric and magnetic field exposure guidelines - Part 1: Sinusoidal waveforms." In: *Health Phys.* 83.3, pp. 341–355.

Rodríguez, A A and A Valli (2010). *Eddy current approximation of Maxwell equations: Theory, algorithms and applications*. 1st ed. Vol. 4. Milano, Italy: Springer-Verlag Milan.

Rodríguez, R (2015). "Numerical approximation of Maxwell equations in low-frequency regime." In: *Computational electromagnetism*. Ed. by A Bermúdez de Castro and A Valli. Switzerland: Springer International Publishing.

Rosen, M R, M J Legato, and R M Weiss (1981). "Developmental changes in impulse conduction in the canine heart." In: *Am. J. Physiol. Heart Circ. Physiol.* 240.4, H546–H554.

Roy, O Z (1980). "Summary of cardiac fibrillation thresholds for 60 Hz currents and voltages applied directly to the heart." In: *Med. Biol. Eng. Comput.* 18, pp. 657–659.

Roy, O Z, G C Park, and J R Scott (1977). "Intracardiac catheter fibrillation thresholds as a function of the duration of 60 Hz current and electrode area." In: *IEEE Trans. Biomed. Eng.* 24.5, pp. 430–435.

Rudy, Y and W Quan (1987). "A model study of the effects of the discrete cellular structure on electrical propagation in cardiac tissue." In: *Circ. Res.* 61, pp. 815–823.

— (1991). "Propagation delays across cardiac gap junctions and their reflection in extracellular potentials: A simulation study." In: *J. Cardiovasc. Electrophysiol.* 2.4, pp. 299–315.

Rush, S and H Larsen (1978). "A practical algorithm for solving dynamic membrane equations." In: *IEEE Trans. Biomed. Eng.* 25.4, pp. 389–392.

Saritas, E U, P W Goodwill, G Z Zhang, and S M Conolly (2013). "Magnetostimulation limits in magnetic particle imaging." In: *IEEE Trans. Med. Imaging* 32.9, pp. 1600–1610.

Scally, M, K J Heston, A G Rudnick, F T Deger, and R M Greenberg (2007). "Strength duration curve for epicardial left ventricular stimulation." In: *PACE* 30, pp. 612–615.

Schaefer, D J, J D Bourland, and J A Nyenhuis (2000). "Review of patient safety in time-varying gradient fields." In: *J. Magn. Reson. Imaging* 12, pp. 20–29.

Schenck, J F (2013). "Safety and sensory aspects of main and gradient fields in MRI." In: *eMagRes* 2, pp. 55–66.

Sedmera, D and R G Gourdie (2014). "Why do we have Purkinje fibers deep in our heart?" In: *Physiol. Res.* 63, pp. 9–18.

Setsompop, K et al. (2013). "Pushing the limits of in vivo diffusion MRI for the Human Connectome Project." In: *NeuroImage* 80, pp. 220–233.

Sharp, G H and R W Joyner (1980). "Simulated propagation of cardiac action potentials." In: *Biophys. J.* 31, pp. 403–424.

Stankovicova, T, V Bito, F Heinzel, K Mubagwa, and K R Sipido (2003). "Isolation and morphology of single Purkinje cells from the porcine heart." In: *Gen. Physiol. Biophys.* 22, pp. 329–340.

Stewart, P, O V Aslanidi, D Noble, P J Noble, M R Boyett, and H Zhang (2009). "Mathematical models of the electrical action potential of Purkinje fibre cells." In: *Phil. Trans. R. Soc. A* 367, pp. 2225–2255.

Sugimoto, T, S F Schaal, and A G Wallace (1967). "Factors determining vulnerability to ventricular fibrillation induced by 60-cps alternating current." In: *Circ. Res.* 21, pp. 601–608.

Tacker, W A and L A Geddes (1996). "The laws of electrical stimulation of cardiac tissue." In: *Proc. of the IEEE* 84.3, pp. 355–365.

Tan, E T, Y Hua, E W Fiveland, M E Vermilyea, J E Piel, K J Park, V B Ho, and T K Foo (2020). "Peripheral nerve stimulation limits of a high amplitude and slew rate magnetic field gradient coil for neuroimaging." In: *Magn. Reson. Med.* 83, 352–366.

Tian, Q et al. (2022). "Comprehensive diffusion MRI dataset for in vivo human brain microstructure mapping using 300 mT/m gradients." In: *Sci. Dat.* 9.7, pp. 1–11.

Tsai, J-Z, J A Will, S Hubbard-Van Stelle, H Cao, S Tungjitkusolmun, Y B Choy, D Haemmerich, V R Vorperian, and J G Webster (2002). "In-vivo measurement of swine myocardial resistivity." In: *IEEE Trans. Biomed. Eng.* 49.5, pp. 472–483.

Tusscher, K H W J ten, D Noble, P J Noble, and A V Panfilov (2004). "A model for human ventricular tissue." In: *Am. J. Physiol. Heart. Circ. Physiol.* 286, pp. 1573–1589.

Valdeomillos, E, Z Jalal, A Metras, F Roubertie, D Benoist, O Bernus, M Haissaguerre, P Bordachar, X Iriart, and J B Thambo (2019). "Animal models of repaired Tetralogy of Fallot: Current applications and future perspectives." In: *Can. J. Cardiol.* 35, pp. 1762–1771.

Vigmond, E J and C Clements (2007). "Construction of a computer model to investigate sawtooth effects in the Purkinje system." In: *IEEE Trans. Biomed. Eng.* 54.3, pp. 389–399.

Walcott, G P, M W Kroll, and R E Ideker (2015). "Ventricular fibrillation: Are swine a sensitive species?" In: *J Interv Card Electrophysiol* 42, pp. 83–89.

Wang, F et al. (2021). "In vivo human whole-brain Connectom diffusion MRI dataset at 760 μm isotropic resolution." In: *Sci. Dat.* 8.122, pp. 1–12.

Wang, W, V Hong, M Rohan, and S R Eisenberg (1995). "Electric fields induced in a human heart by MRI gradient coils: A finite element study." In: *Conf. Proc. IEEE Eng. Med. Biol. Soc.* Pp. 475–476.

Weiss, G (1901). "Sur la possibilité de rendre comparables entre eux les appareil servant a l'éxitation électrique." In: *Arch. Ital. de Biol.* 35, pp. 413–446.

Xia, L, F Liu, and H Zhao (2002). "Simulation study of the potential hazards of cardiac stimulation by induced eddy-currents in modern MRI." In: *Comput. Cardiol.* 29, pp. 725–728.

Xia, L, W Lu, and Y Duan (1996). "Microcomputer-based cardiac arrhythmia simulation model." In: *Med. Biol. Eng. Comput.* 34.Suppl I, pp. 42–43.

Yamaguchi, M, T Andoh, T Goto, A Hosono, T Kawakami, F Okumura, H Syugyo, T Takenaka, and I Yamamoto (1991). "Stimulation of dog heart by pulsed magnetic fields." In: *Jpn. J. Appl. Phys.* 30.11A, pp. 1905–1906.

Yamaguchi, M, T Andoh, T Goto, A Hosono, T Kawakami, F Okumura, T Takenaka, and I Yamamoto (1992). "Heart stimulation by time-varying magnetic fields." In: *Jpn. J. Appl. Phys.* 31, pp. 2310–2316.

— (1994). "Effects of strong pulsed magnetic fields on the cardiac activity of an open chest dog." In: *IEEE Trans. Biomed. Eng.* 41.12, pp. 1188–1191.

DECLARATION

I hereby declare that this dissertation is solely my original work. I have only used the sources indicated and have not made unauthorized use of services of a third party. Where the work of others has been quoted or reproduced, the source is always given.

I have not yet presented this thesis or parts thereof to a university as part of an examination or degree.

I hereby confirm that the declarations made above are correct. I am aware of the importance of a sworn affidavit and the criminal prosecution in case of a false or incomplete affidavit.

I affirm that the above is the absolute truth to the best of my knowledge and that I have not concealed anything.

Heidelberg, February 21st 2022

Valerie Susanne Klein